MEASUREMENT OF THE STANDARD MODEL PROCESSES FOR SUPERSYMMETRY SEARCH IN LOW MOMENTUM SINGLE-ELECTRON EVENTS IN THE VECTOR BOSON FUSION TOPOLOGY AT THE LHC

A Dissertation

by

ALI CELIK

Submitted to the Office of Graduate and Professional Studies of
Texas A&M University
in partial fulfillment of the requirements for the degree of

DOCTOR OF PHILOSOPHY

Chair of Committee,	Teruki Kamon
Co-Chair of Committee,	Othmane Bouhali
Committee Members,	Bhaskar Dutta
	Robert Webb
	Stephen A. Fulling
Head of Department,	Grigory Rogachev

May 2018

Major Subject: Physics

ABSTRACT

The yield of events with two jets, a single low-momentum electron, and large missing transverse momentum in the vector boson fusion (VBF) topology is measured in proton-proton collisions at center-of-mass energy of 13 TeV. The data corresponds to a total integrated luminosity of 35.86 fb^{-1} collected in 2016 by the CMS detector at CERN's Large Hadron Collider. The event selection requirements with electron's transverse momentum of 10 GeV to 40 GeV are optimized for the production of charginos ($\tilde{\chi}_1^{\pm}$) and next-to-lightest neutralinos ($\tilde{\chi}_2^0$) in supersymmetry (SUSY) compressed mass-spectra scenarios where the mass difference (ΔM) between $\tilde{\chi}_1^{\pm}$ and lightest neutralino ($\tilde{\chi}_1^0$) is small. The masses of sleptons ($\tilde{l}$) are assumed to be between $\tilde{\chi}_1^{\pm}$ and $\tilde{\chi}_1^0$. The measurements in the VBF topology in various control regions are performed for the first time at hadron collider experiments, and the observed events are consistent with expectations by the Standard Model (SM) processes. The results are used to predict the SM event yields in the signal region in a blind analysis, and to set limits on the SUSY production in the VBF topology. Expected lower limits at 95% CL on the $\tilde{\chi}_1^{\pm}/\tilde{\chi}_2^0$ mass are reported for various ΔM values in a scenario, where the branching fraction of $\tilde{l} \rightarrow l + \tilde{\chi}_1^0$ is 1/3 for each lepton flavour. The expected limits will be compared with observed limits in the next phase of the blind analysis.

DEDICATION

This dissertation is dedicated to my beloved family.

ACKNOWLEDGMENTS

First of all, I would like to thank my family who have always supported me and all others who have helped me to get to this point today.

Prof. Teruki Kamon is not only a perfect advisor and mentor, but he is a great friend too. Whenever I had any issues, including personal ones, he always helped me to overcome them. I want to thank Prof. Kamon for all his help, guidance, and advice, which has made me a better person and physicist. I am really grateful for his support.

I would also like to thank Prof. Bhaskar Dutta for raising the level of out physics discussions during the pheno meetings and his truly enlightening explanations. There is also no doubt that his jokes are as great as him, which made the meetings more enjoyable.

I did not have a chance to work with Prof. Alfredo Gurrola when he was a graduate student at TAMU, however I had the opportunity to work with him later on. He is the best colleague that one could ask to work with. I would like to thank Prof. Gurrola for leading our analysis group and helping me whenever I had questions.

Prof. Andres Florez, thank you very much for all your guidance. Your comments always challenged me to think differently and ultimately led to a better result.

I had an extraordinary opportunity to work at the Fermi National Accelerator Laboratory for more than two years. I met so many great people who are a source of wisdom. Prof. Stephan Lammel was my on site advisor during my stay at Fermilab. I would like to thank him for his support. My stay at Fermilab

was definitely enriched because of his guidance. I must also thank him for the discussions both during and after our group meetings.

Prof. Carlos Avila, Minsuk Kim, Andres Leonardo Cabrera Mora, Priyanka Kumari, Prof. Will H. Flanagan, Andres Delannoy, Jose David Ruiz Alvarez, Roy Montalvo, Amandeep Kalsi, Sho Maruyama, Andrew Melo, Denis Rathjens, Yu Gao, Tathagata Gosh, Sean Wu and anyone I rudely left out, it was a real pleasure for me to know and work with all of them. I want to thank all of them for their help and support.

I would like to thank my office mates at Fermilab; Alexx Perloff, Daniel Edison Marley, Ryan Mueller, and Scarlet Norberg; for helping me with checking the grammar in my dissertation. I again want to thank Alexx for his help with coding, ROOT, and his extraordinary effort on reviewing this dissertation.

I would like to thank Prof. Othmane Bouhali, Prof. Robert Webb, and Prof. Stephen A. Fulling for being on my committee.

I also want to thank the Burucu family who helped me a lot during my stay in Texas and my visits to TAMU.

I met three great people during my stay in Naperville. Elena Hsu, Mike Hsu, and Sherry Lin, all treated me as if I was a part of their family. I am truly grateful for all the things they have done for me and I will always remember those enjoyable moments I had with them.

Lastly, I would like to thank the Turkish Ministry of National Education and the Fermi National Accelerator Laboratory, both of which have financially supported me during my PhD studies.

CONTRIBUTORS AND FUNDING SOURCES

Contributors

This work was supported by a dissertation committee consisting of Professor Teruki Kamon [advisor], Professor Othmane Bouhali [co-advisor] and Professor Bhaskar Dutta, Robert Webb of the Department of Physics and Professor Stephen A. Fulling of the Department of Mathematics.

The analyses depicted in Section 2 were conducted by compact muon solenoid (CMS) collaboration and was published in 2015.

All other work conducted for the dissertation was completed by the student independently.

Funding Sources

The graduate student was supported by Republic of Turkey Ministry of National Education, Fermi National Laboratory (Fermilab) LPC and Department of Energy (DOE) grant DE-SC0010813.

NOMENCLATURE

ATLAS	A Toroidal LHC Apparatus.
ALICE	A Large Ion Collider Experiment.
BF	Branching Fraction.
BSM	Beyond Standard Model.
CDM	Cold Dark Matter.
CDF	Collider Detector at Fermilab.
CERN	The European Organization for Nuclear Research.
CL	Confidence Level.
CMS	Compact Muon Solenoid.
CR	Control region.
CSC	Cathode Strip Chambers.
CSV	Combined Secondary Vertex.
DAQ	Data Acquisition.
DM	Dark Matter.
DT	Drift Tube.
DUNE	Deep Underground Neutrino Experiment.
EB	Electromagnetic Barrel Calorimeter.
ECAL	Electromagnetic Calorimeter.
EE	Electromagnetic Endcap Calorimeter.
EFT	Effective Fields Theory.

EM	Electromagnetic.
FPGA	Field Programmable Gate Array.
FSR	Final state radiation.
GEM	Gas Electron Multiplier.
GSF	Gaussian Sum Filter.
GUT	Grand Unified Theory.
HB	Hadronic Barrel Calorimeter.
HCAL	Hadronic Calorimeter.
HE	Hadronic End-cap Calorimeters.
HF	Hadronic Forward Calorimeter.
HEP	High Energy Physics.
HL-LHC	High-Luminosity Large Hadron Collider.
HLT	High level trigger.
HO	Hadronic Outer Barrel Calorimeter.
HV	High Voltage.
ISR	Initial state radiation.
JER	Jet Energy Resolution.
JES	Jet Energy Scale.
L1	Level-1.
LEP	Large Electron-Positron.
LHC	Large Hadron Collider.
LHCb	Large Hadron Collider beauty.
LO	Leading order.
LS	Like Sign.

LS2	Second Long Shut-Down.
LSP	Lightest Supersymmetric Particle.
MC	Monte Carlo.
ME	Muon Endcap.
MINOS	Main Injector Neutrino Oscillation Search.
MIP	Minimum Ionizing Particles.
MSSM	Minimal Supersymmetric Extension of the Standard Model.
NLO	Next-to-leading order.
NNLO	Next-to-next-to-leading order.
OS	Opposite Sign.
PD	Primary Dataset.
PDF	Parton Distribution Function.
PF	Particle Flow.
POG	Physics Object Group.
PS	Proton Synchrotron.
PU	Pile-Up.
QCD	Quantum Chromodynamics.
RMS	Root mean square.
ROC	Readout Chip.
RPC	Resistive Plate Chambers.
RPV	R-parity Violating.
SEU	Single Event Upset.
SM	Standard Model.

SPS	Super Proton Synchrotron.
SR	Signal region.
SUSY	Supersymmetry.
TEC	Tracker End Cap.
TIB	Tracker Inner Barrel.
TID	Tracker Outer Barrel.
UE	Underlying Event.
VEV	Vacuum Expectation Value.
VBF	Vector Boson Fusion.
VR	Validation region.

TABLE OF CONTENTS

Page

ABSTRACT ii

DEDICATION iii

ACKNOWLEDGMENTS iv

CONTRIBUTORS AND FUNDING SOURCES vi

NOMENCLATURE vii

TABLE OF CONTENTS xi

LIST OF FIGURES xiv

LIST OF TABLES xviii

1. INTRODUCTION 1

2. STANDARD MODEL AND SUPERSYMMETRY 3

    2.1 Standard Model 3
        2.1.1 Higgs Mechanism 7
    2.2 Supersymmetry 9
        2.2.1 Search Strategy in VBF 14
        2.2.2 Review of Run-I Analysis 16
            2.2.2.1 Search for Charginos/Neutralinos Using the VBF Processes 16

3. THE LARGE HADRON COLLIDER & COMPACT MUON SOLENOID DETECTOR 19

    3.1 The Large Hadron Collider 19
    3.2 Compact Muon Solenoid Detector 20
        3.2.1 The CMS Coordinate System 22
        3.2.2 Superconducting Magnet 23
        3.2.3 The Tracker 24
            3.2.3.1 Pixel Tracker 26

3.2.3.2 Strip Tracker 27
3.2.4 The Electromagnetic Calorimeter 28
3.2.5 The Hadron Calorimeter 29
3.2.6 The Muon System 31
3.2.6.1 Drift Tube Chambers 32
3.2.6.2 Cathode Strip Chambers 33
3.2.6.3 Resistive Plate Chambers 34
3.2.6.4 Gas Electron Multipliers 35
3.2.6.5 ME0 37

4. TRIGGER SYSTEM AT CMS 39

4.1 Level-1 Trigger 39
4.2 High-Level Triggers 40
4.2.1 Mu+VBF High Level Trigger 41

5. PHYSICS OBJECTS 45

5.1 The Particle Flow Algorithm 46
5.2 Jets 46
5.3 Missing Transverse Energy 47
5.4 Electron 48
5.5 Muons 50
5.6 Hadronically Decaying Tau Lepton 51
5.7 B-Tagged Jets 51
5.8 Event Generation and Simulation 53
5.8.1 MadGraph 5 53
5.8.2 Pythia 53
5.8.3 POWHEG 54
5.8.4 Geant4 54

6. DATA AND MONTE CARLO SAMPLES 55

6.1 Data Samples 55
6.2 MC Samples 57

7. ANALYSIS 59

7.1 Signal Region and Control Regions 59
7.2 Optimization 60
7.3 Background Estimation Using ABCD Method 63
7.3.1 ABCD Method 63
7.3.2 $t\bar{t}$ Estimation 63
7.3.3 $W(\rightarrow e\nu)+$ jets Estimation 69

7.3.4 Other Backgrounds 76
7.4 $t\bar{t}$ Closure Test 76
7.5 Validation of the $t\bar{t}$ Scale Factors and VBF Shapes with Low-m_T Region 79
7.6 Validation of the $t\bar{t}$ VBF Shapes with Dilepton Samples 81
7.7 Validation of the W + jets Scale Factors and VBF Shapes with Low-m_T Region 83
7.8 Expected Limits 84
7.9 Data in the Signal Region 86

8. CONCLUSIONS 89

REFERENCES 91

LIST OF FIGURES

FIGURE Page

2.1 Standard Model of elementary particles and gauge bosons. Reprinted from [1] 6

2.2 Summary of the cross section measurements of Standard Model processes. Reprinted from [2] 7

2.3 Higgs potential 8

2.4 Left: one loop quantum correction to the higgs squared mass parameter (m_H^2) from a particle f. Right: quantum correction to (m_H^2) from a scalar S. 11

2.5 Inverse of the three different force coupling represented by dot lines do not unify at GUT scale with SM whereas coupling represented by solid lines meet at the GUT (10^{16} GeV) with SUSY. Reprinted from [3] 14

2.6 Representative Feynman diagram for VBF production of chargino-chargino pair production in VBF process (left), and chargino-neutralino pair production (right). Reprinted from [4] 15

2.7 Observed limits for electroweakino searches with 8 TeV data. Reprinted from [5] 16

2.8 Left: dijet mass distribution after combining all 8 channels. There is a good agreement between data and MC. Right: observed and expected limits on mass of $\tilde{\chi}_1^{\pm}$ and $\tilde{\chi}_2^0$ for two different scenarios after combining all channels. Reprinted from [4] 18

3.1 Large hadron collider. Reprinted from [6] 20

3.2 Cross section of the CMS detector. Reprinted from [7] 22

3.3 CMS coordinate system 23

3.4 Tracking system at CMS detector. Reprinted from [8] 26

3.5 Pixel detector layers in the barrel and endcap section of CMS detector. Reprinted from [9] 27

3.6 Layout of the pixel detectors and read-out chips. Reprinted from [10] 28

3.7 Simulated electromagnetic shower in a lead tungstate crystal. Reprinted from [9] 29

3.8 Cross section of ECAL. Reprinted from [9] 30

3.9 A quadrant of the HCAL. Reprinted from [11] 31

3.10 Muon system in the CMS detector. 32

3.11 Illustration of drift tube chamber. 33

3.12 Illustration of cathode chamber. 34

3.13 Left: a GEM superchamber. Right: layout of long and short GEM superchambers. Long chamber is located at 12 o'clock position and both long and short chamber have 8 η partitions. Reprinted from [12] 36

3.14 Left: picture of GEM foils. Right: a schematic view of electron flow and electric field through the holes. Reprinted from [12] 37

3.15 Illustration of working principle of a three layer GEM chamber. Reprinted from [12] 38

4.1 CMS level 1 trigger system. After events pass each independent detector's trigger, then events are sent to global muon/calorimeter triggers which combine the information and send to global trigger for final decision. Reprinted from [13] 40

4.2 Left: trigger efficiency for monojet trigger as a function of E_T^{miss} in the case where both jets are central ($|\eta| < 3.0$). Right: shows trigger efficiency for monojet trigger as a function of E_T^{miss} in the case where one jet is central while the other one is forward ($3.0 < |\eta| < 5.0$) 42

4.3 Left: mu+VBF trigger efficiency as a function of m_{jj}. Right: mu+VBF trigger efficiency as a function of missing transverse energy. 44

5.1 Transverse slice of the CMS detector and paths for several species of particles traveling in the magnetic field. Reprinted from [9] 45

5.2 η distribution for jets in a $t\bar{t}$ control sample with one soft electron, 1 b-tagged jet, $E_T^{miss} > 250$ GeV, and $m_T(e, E_T^{miss}) < 110$ GeV..... 48

5.3 Illustration of a displaced secondary vertex with respect to a primary vertex in an event containing a bottom quark. Reprinted from [14]..... 52

6.1 Integrated luminosity delivered by LHC and recorded by CMS. Reprinted from [15]..... 56

7.1 (a) m_{jj}, and (b) η^{jets}..... 60

7.2 (a) leading jet p_{T}, and (b) E_T^{miss}..... 61

7.3 Transverse mass distribution..... 62

7.4 Signal significance S divided by the max significance S_{max}, as a function of E_T^{miss}. 62

7.5 $t\bar{t}$ background estimation and validation strategy. 64

7.6 (Top from left to right) electron η and p_{T} distributions. Electron m_T and MET distributions (bottom left and right respectively) in $t\bar{t}$ enriched control region (CR1) after applying SF. 67

7.7 (Top from left to right) electron η and p_{T} distributions. Electron m_T and MET distributions (bottom left and right respectively) in $t\bar{t}$ enriched control region (CR2) after applying SF. 68

7.8 W + jets estimation strategy. 70

7.9 (a) p_T^e and (b) η^e distributions for W + jets CR1. 70

7.10 (a) $m_T(e, E_T^{miss})$ and (b) $E_{\mathrm{T}}^{\mathrm{miss}}$ distributions for W + jets CR1..... 71

7.11 (Top from left to right) muon η and p_{T} distributions. Central jet η with di-muon invariant mass distributions (bottom left and right respectively) in DY+jets dominated CR (CR2) after applying SF. ... 74

7.12 (Top from left to right) muon η and p_{T} distributions. Central jet η with di-muon invariant mass distributions (bottom left and right respectively) in CR3 after applying SF. 75

7.13 Comparision of events with 1 b-jet and 0-b jet after lepton matching and normalized to unity. Top from left to right, electron η and p_{T} distributions. Bottom left to right, m_T and m_{jj} distributions..... 78

7.14 Comparision of events with 1 b-jet and 0-b jet after no lepton matching. Distributions are normalized to unity. Top from left to right, electron η and p_{T} distributions. Bottom left and right, m_T and $m_j j$ distributions respectively. 79

7.15 (a) $\eta(e)$ and (b) $p_{\mathrm{T}}(e)$ distributions in VR1..... 80

7.16 (a) $\eta(e)$, (b) $p_{\mathrm{T}}(e)$, (c) E_T^{miss}, and (d) m_{jj} distributions for the $t\bar{t}$ in VR2. 81

7.17 m_{jj} distributions for the $t\bar{t}$ $\mu\mu$ and $e\mu$ shape validation regions. 82

7.18 (a) η^e and (b) p_{T}^e distributions for the W + jets validation region VR1. 84

7.19 W + jets validation strategy..... 85

7.20 (a) η^{e}, (b) $p_{\mathrm{T}}^{\mathrm{e}}$, (c) E_{T}^{miss}, and (d) m_{jj} distributions for the W + jets validation region VR2. 86

7.21 Expected upper limit on chargino/neutralino after combining all channels in a democratic scenario for different ΔM benchmarks. 88

LIST OF TABLES

TABLE Page

2.1 Quantum numbers of first generation fermions. Reprinted from [16] 4

3.1 Some of the parameters of superconducting magnet of CMS detector. Reprinted from [17] 24

5.1 Loose Jet-ID selections. 47

5.2 Electron ID selections. 49

5.3 μ Identification 50

5.4 Reconstructed tau decay modes 52

6.1 Collision data samples correspond to an integrated luminosity of 35.86 fb^{-1} 55

6.2 MC samples 57

6.3 List of officially produced signal samples. Mass of chargino-neutralino is given in the sample name's description. The "leptonic" in the naming means branching ratio to selectron or smuon is 50 %. 58

7.1 Event selection cuts after optimization 63

7.2 Predicted and observed rates for the $t\bar{t}$ control regions with inverted VBF selections, CR1. 65

7.3 Predicted and observed rates in CR2 after requiring 1 b-jet in addition to central and VBF selections. 66

7.4 Predicted and observed rates along with data to MC scale factor for the W + jets control regions with inverted VBF selections. SF^{CR1} is calculated as $(N^{\mathrm{CR1}}(\mathrm{Data}) - N^{\mathrm{CR1}}(\mathrm{other\ BGs}))/N^{\mathrm{CR1}}(\mathrm{W + jets})$. ... 72

7.5 Event yields in $Z \to \mu\mu$ enriched region and VBF region called CR2 and CR3 respectively. 72

7.6 Event selections criteria for DY+jets CR2. On top of those following cuts, VBF cuts are also applied for another region called "CR3" in order to measure VBF efficiency as a ratio of two regions. 76

7.7 Composition of $t\bar{t}$ events in both signal and control regions. 77

7.8 Predicted and observed rates for validation region VR1, used to validate the scale factor measured from $t\bar{t}$ control sample CR1. 82

7.9 Predicted and observed rates for validation region VR2 which are used to validate the VBF efficiency scale factors measured from $t\bar{t}$ control sample CR2. 83

7.12 Expected event yield in the signal region after combining all leptonic channels. 86

7.10 Predicted and observed rates for the W + jets validation region VR1, which obtained with inverted m_T and VBF selections. 87

7.11 Predicted and observed rates for the W + jets validation region VR2, which is used to validate the VBF efficiency measured from $Z(\rightarrow \mu\mu)$ + jets control sample CR3. 88

1. INTRODUCTION

For centuries, human beings have always been curious about the surroundings. What are the fundamental constituents of matter? How do fundamental particles interact? These are some of the questions that have been asked and endlessly pursued. While asking those questions, they never gave up to find answer the those questions and come up with great models/theories.

Standard model (SM) of particle physics describe the fundamental components of the matter around us along with their interaction with each other. Many elementary particles predicted by the SM have been discovered in the past by different experiments and accomplished its success with discovery of 125 GeV Higgs boson in 2011 at Large Hadron Collider (LHC) at CERN which accommodate a gigantic, the most complicated particle detector ever built.

However, there are still many questions the SM cannot answer such as neutrino mass, existence of Dark matter or unification of three gauge interactions of the Standard Model into one which causes a belief that the SM is valid up to a certain energy scale. Theories beyond the SM (BSM) attempt to answer those phenomena that cannot be explained by the SM.

Supersymmetry, one of the extension to the SM, predicts a Dark matter candidate which provides a Dark Matter relic density [18] consistent with the astronomical observations on top of unification of three forces at GUT scale and solving hierarchy problem in the mass of Higgs boson.

This dissertation is organized as follows. An introduction in Section 1. Theoretical aspect of the SM and SUSY followed by SUSY searches with different scenarios and compressed mass-spectra in VBF in the second section. Section 3

provides information about LHC and CMS detector along with the sub-detectors while Section 4 and 5 give a general description of Trigger at CMS and particle reconstruction with the CMS detector respectively. Section 6 is about Data, MC and signal samples used in this analysis. Section 7 presents background estimation method and the search for chargino-chargino and chargino-neutralino production in single lepton channel through VBF at 13 TeV. The results/interpretation and limits are presented in Section 8.

2. STANDARD MODEL AND SUPERSYMMETRY

2.1 Standard Model

The Standard Model (SM) is the most successful theory of elementary particles and fundamental forces. This success has been proved by the ATLAS and CMS experiments with the observation of the Higgs boson at mass of the 125 GeV [19, 20] in 2012. The SM first conceived by Sheldon Lee Glashow [21], Abdus Salam [22] and Steven Weinberg [23] describes two fundamental forces (weak, electromagnetic) and constituents of matter which are made of elementary particles called quark and leptons. The SM is defined by $U(1)_Y \times SU(2)_L \times SU(3)_C$ gauge symmetry. The W and Z bosons are carriers for weak force governed by the $SU(2)$ gauge group, the photon is a force carrier for electromagnetic force and governed by $U(1)$, while the gluon is responsible for the strong force and governed by $SU(3)$. Subscripts C, Y correspond to conserved quantum number of each symmetry group "color" and "hypercharge and isospin". L denotes the symmetry as applied to left handed and anti-right handed fermions. Gravity, is not included in the SM since its effect is too small on this scale. Force carriers are gauge bosons. The SM contains 12 spin- $\frac{1}{2}$ fermions and four spin-1 bosons (Figure 2.1). Fermions obey Fermi-Dirac statistics which does not allow two fermions to occupy the same state at the same time while bosons, obey Bose-Einstein statistics, can occupy the same state at the same time.

There are three generation of quarks and leptons. The up and down quarks (u and d) are the first generation quarks, strange and charm quarks (s and c) are second generation while top and bottom quarks (t and b) are the third generation of quarks. Corresponding to 12 quarks, there are also 12 anti-quarks which have

the same mass and opposite charge. While quarks in first row in Figure 2.1 (u, c and t) have electric charge of "$\frac{2}{3}|e|$" quarks in second row (d, s and b) have electric charge of "$\frac{-1}{3}|e|$". Electric charges, $Q = T_L^3 + Y/2$ where T is weak isospin quantum numbers, are shown in Table 2.1 for leptons and quarks. Quarks also carry color charges: red, blue and green(Q_r, Q_b, Q_g) and they cannot be observed in a free state due to color confinement [24]. As quarks, there are also three generation of leptons total of 12 with their anti particles. First generation leptons are electron, electron neutrino (e and ν_e), second generation is muon, muon neutrino (μ and ν_μ), and third generation is tau, tau neutrino (τ and ν_τ) with charge -1 and 0 for e,μ,τ, and ν_e,ν_μ,ν_τ respectively. The most distinctive difference among the generation is the mass. While first generation particle; electron has mass of 0.511 MeV/c^2, third generation particle τ is about 3×10^3 times heavier.

Table 2.1: Quantum numbers of first generation fermions. Reprinted from [16]

Particle	Q	T_L^3	Y	C
ν_e	0	1/2	-1	0
e_L	-1	$-1/2$	-1	0
e_R	-1	0	-2	0
u_L	2/3	1/2	1/3	r,g,b
d_L	$-1/3$	$-1/2$	1/3	r,g,b
u_R	2/3	0	4/3	r,g,b
d_R	$-1/3$	0	$-2/3$	r,g,b

Fermions are expressed as a left-handed weak isospin doublet and a right-handed singlet as seen in Eq. 2.1-2.2 which correspond to leptons and quarks respectively. Subscripts $i = 1, 2, 3$ corresponds to the three generation of fermions.

$$l_{iL} = \begin{pmatrix} \nu_i \\ l_i \end{pmatrix} i.e. \begin{pmatrix} \nu_e \\ e \end{pmatrix}_L , \begin{pmatrix} \nu_\mu \\ \mu \end{pmatrix}_L , \begin{pmatrix} \nu_\tau \\ \tau \end{pmatrix}_L , e_R, \mu_R, \tau_R \tag{2.1}$$

$$q_{iL} = \begin{pmatrix} u_i \\ d_i \end{pmatrix} i.e \begin{pmatrix} u \\ d \end{pmatrix}_L \begin{pmatrix} c \\ s \end{pmatrix}_L \begin{pmatrix} t \\ b \end{pmatrix}_L , u_R, d_R, s_R, c_R, t_R, b_R \tag{2.2}$$

While electrons, muons and taus interact via the electromagnetic and weak forces, neutrinos interact via only the weak force. Quarks interact through the electromagnetic, weak and strong forces. The quarks are arranged in triplets under the $SU(3)_C$ transformation and denoted as seen in Equation 2.3 while leptons are singlet under the $SU(3)_C$ and thus cannot interact through the strong force.

$$q = \begin{pmatrix} q_r \\ q_g \\ q_b \end{pmatrix} \tag{2.3}$$

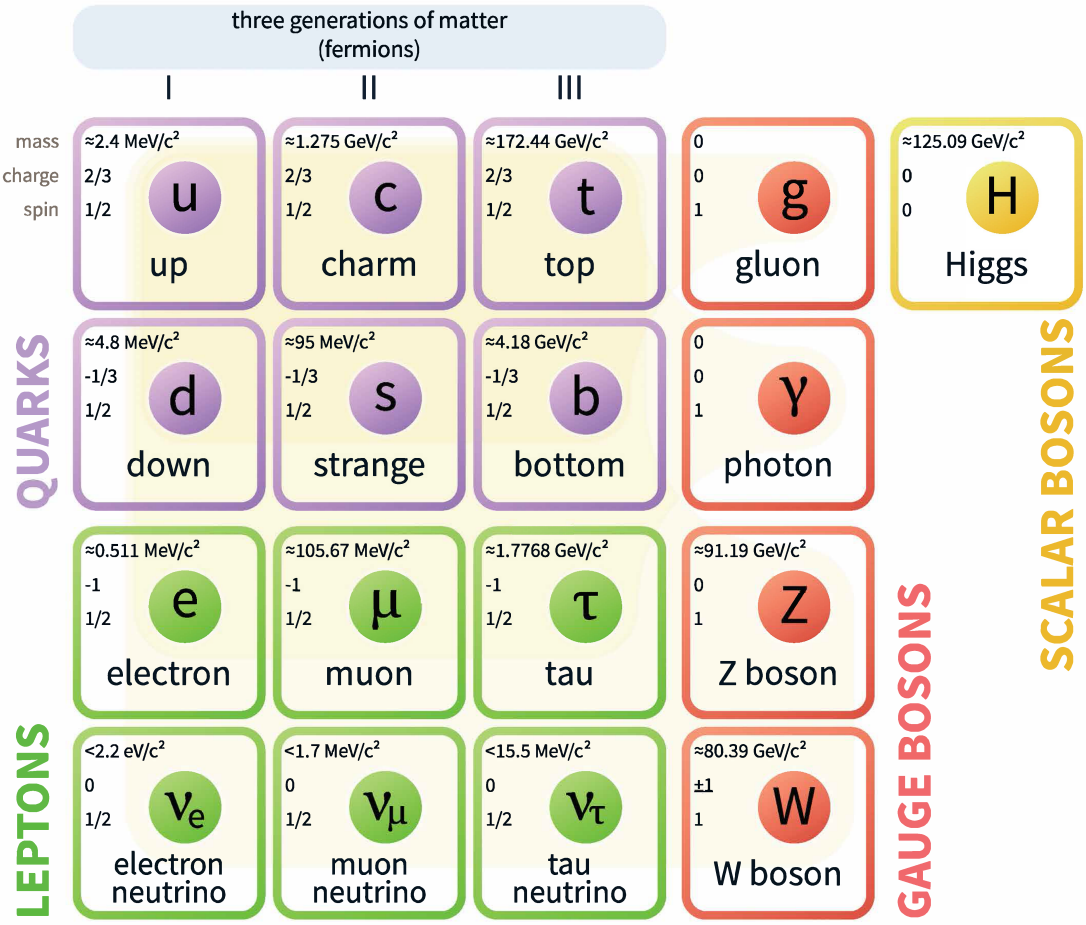

Figure 2.1: Standard Model of elementary particles and gauge bosons. Reprinted from [1]

Quarks create a colorless bound state called hadrons. Hadrons are divided into two: Mesons and baryons. Baryons are made up of three quarks e.g. protons and neutrons, mesons are made up of an anti-quark and a quark pair e.g. pions, kaons.

The CMS experiment provides the total production cross sections for the SM

processes. As seen in the Figure 2.2, theoretical cross sections of different SM processes at different collision energies (7,8 and 13 TeV) are in a good agreement with data within the uncertainty for all three center of mass energies.

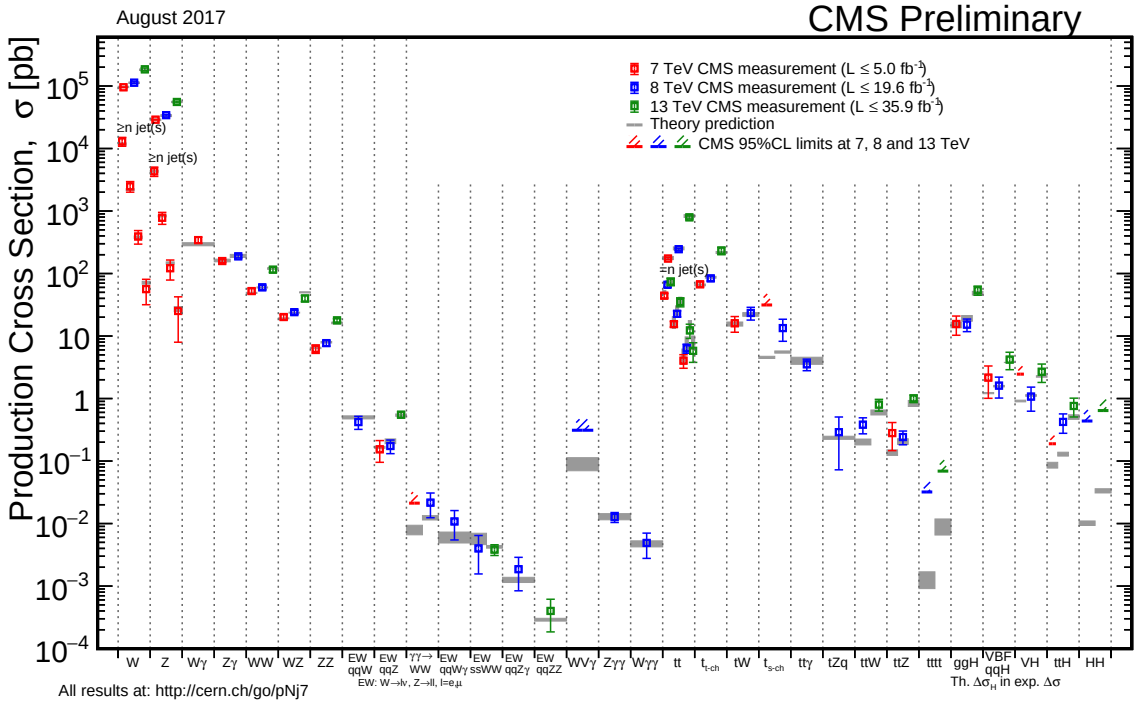

Figure 2.2: Summary of the cross section measurements of Standard Model processes. Reprinted from [2]

2.1.1 Higgs Mechanism

Experiments show that fermions and gauge bosons have mass. Higgs mechanism in the SM explains the generation of masses for fermions and weak gauge bosons (W^+, W^- and Z). After spontaneous symmetry breaking, Higgs field gives masses to the elementary particles which interact with it. The scalar Higgs part of the Lagrangian is given by:

$$\mathcal{L} = (D^{\mu}\phi)^{\dagger}(D_{\mu}\phi) - V(\phi) \tag{2.4}$$

where $V(\phi)$ is potential and expressed as:

$$V(\phi) = -\mu^2\phi^{+}\phi + \lambda(\phi^{+}\phi)^2 \tag{2.5}$$

and also SM Higgs field is given by:

$$\phi = \begin{pmatrix} \phi^{+} \\ \phi^{0} \end{pmatrix} \tag{2.6}$$

The case where $\mu^2 < 0$ and $\lambda > 0$ corresponds to vacuum expectation value $v = \sqrt{\mu^2/2\lambda}$. The Higgs potential in this case is depicted as in Figure 2.3 which is called the Mexican hat potential.

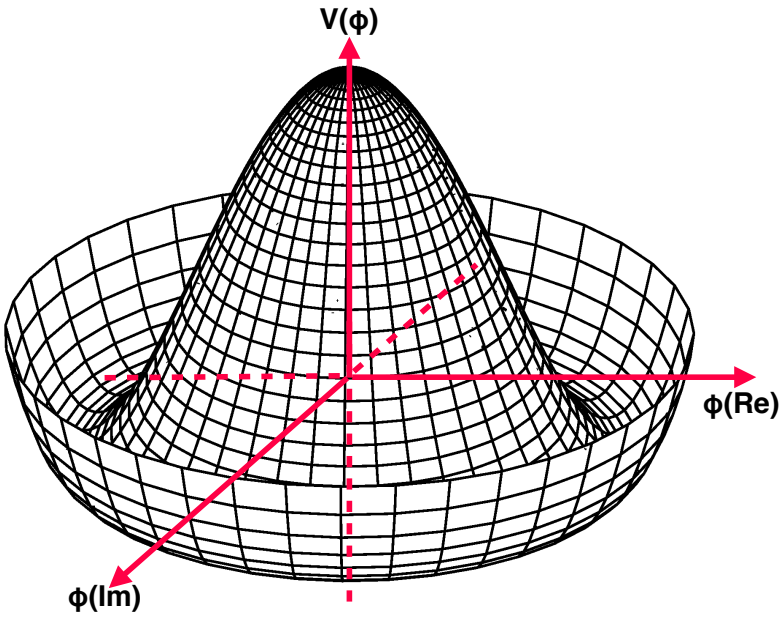

Figure 2.3: Higgs potential

By expanding Equation 2.6 around its vacuum expectation value v, it becomes 2.7:

$$\phi = \frac{1}{\sqrt{2}} \begin{pmatrix} 0 \\ v + h \end{pmatrix} \tag{2.7}$$

By choosing a direction, we have a broken symmetry. As a result of this broken symmetry, mass terms for gauge bosons and fermions as well as for scalar particle Higgs boson are obtained from Equation 2.4.

2.2 Supersymmetry

Although the SM achieved a great accomplishment so far, it has an inability to explain some of the phenomena such as neutrino masses [25], large differences on the masses of three generations of quarks, leptons and the existence of cold dark matter (CDM) observed by astronomers.

Understanding the nature of dark matter (DM) in the Universe would rank among the biggest leaps forward in the progress of fundamental physics. Supersymmetry (SUSY), one of the many extensions to the SM, proposes a super particle corresponding to every single particle in the SM with the same quantum numbers, except for spin, which differs by half spin. SUSY remains perhaps the best motivated of the possible theories to simultaneously describe the nature of DM and solve the gauge hierarchy problem in the SM.

Not only answering the question stated above that SM cannot explain, but SUSY also has the ability to unify the SM forces at GUT scale [26] (see Figure 2.5) on top of solving the quadratic divergence of the Higgs mass by canceling the contribution coming from particles and their superpartners.

Higgs boson masses get a huge quantum correction from the particle coupling

to the Higgs field. Contribution to the square of the Higgs mass from a loop containing a Dirac fermion f is seen in Figure 2.4 left. This correction from the particle can be seen in Eq. 2.8, when it couples to the Higgs field via a term $-\lambda_f \bar{\psi} H \psi$, where λ_f is Yukawa coupling, ψ is Dirac field and H is Higgs field. Since Yukawa coupling is proportional to the mass of the particle coupling to the Higgs field, the heavier coupling particle the more quantum correction to the Higgs boson mass. Thus, we can say most contribution to m_H^2 is coming from then top quark. However, if a scalar S that couples to the Higgs via an interaction term $-\lambda_S |H|^2 |\psi|^2$, then corrections to m_H^2 from Figure 2.4 will become Eq. 2.9

$$\Delta m_H^2 = -\frac{|\lambda_f|^2}{8\pi^2} \Lambda_{UV}^2 + \dots \tag{2.8}$$

$$\Delta m_H^2 = \frac{|\lambda_S|^2}{16\pi^2} \Lambda_{UV}^2 + \dots \tag{2.9}$$

By comparing the Eq. 2.9 and Eq. 2.8 it can be seen that this contribution to m_H^2 can be cancelled by a symmetry between fermions and bosons due to a minus sign between the two loops. If we assume two complex scalar fields existed with $\lambda_S = |\lambda_f|^2$ and accompany to each of the quarks and leptons of the Standard Model, then total contribution to the Higgs mass will be zero.

Minimal supersymmetric extension of the Standard Model (MSSM) is the most simple version of a SUSY theory. It contains a supersymmetric partner, which is classified in either by the chiral or gauge supermultiplet, to each particle in the SM with a spin by half. In addition to those mass eigenstates, there can even also be mixing between electroweak gauginos and the higgsinos due to electroweak symmetry breaking. An example of this is neutralinos that are

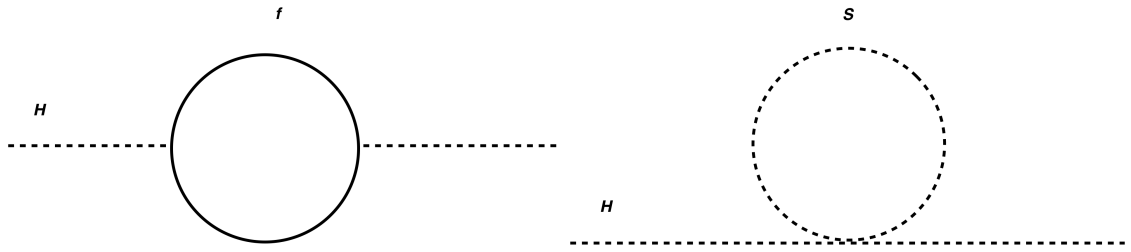

Figure 2.4: Left: one loop quantum correction to the higgs squared mass parameter (m_H^2) from a particle f. Right: quantum correction to (m_H^2) from a scalar S.

formed via the mixing between neutral Higgsinos ($\tilde{H}_d^0$, $\tilde{H}_u^0$) and neutral gauginos ($\tilde{B}$, $\tilde{W}^0$). Or charginos being a mixed form of the charged Winos ($\tilde{W}^+$, $\tilde{W}^-$) and Higgsinos ($\tilde{H}_d^+$, $\tilde{H}_u^+$). H_u and H_d which are denoted as (H_u^+, H_u^0) and (H_d^0, H_d^-) respectively are Higgs fields introduced by MSSM. Linear combination of H_u^0 and H_d^0 correspond to the SM Higgs boson. While neutral weak isospin components of H_u (H_u^0) are responsible for giving mass to up types of quarks, H_d^0 gives mass to down type quarks.

The chargino and neutralino mass eigenstates are denoted by $\tilde{\chi}_i^{\pm}$ and $\tilde{\chi}_i^0$ where index i runs over $1, 2$ and $1, 2, 3, 4$ respectively. The neutralino mass term in the Langrangian is given in Eq. 2.10, where $\mathrm{M}_{\tilde{\chi}^0}$ and ψ^0 are 4×4 mass matrix (given in Eq 2.12 where M_1, M_2, $-\mu$ are bino, wino and higgsino mass parameters and s_β, s_W, c_β, c_W are abbrevation for $\sin\beta$, $\sin\theta_W$, $\cos\beta$, $\cos\theta_W$ respectively.) and gauge-eigenstate basis ($\tilde{B}$, $\tilde{W}^0$, $\tilde{H}_d^0$, $\tilde{H}_u^0$) respectively.

$$\mathcal{L}_{m_{\tilde{\chi}^0}} = \frac{-1}{2}(\psi^0)^T M_{\tilde{\chi}^0} \psi^0 + h.c. \tag{2.10}$$

$$M_{\tilde{\chi}^0} = \begin{pmatrix} M_1 & 0 & -M_z c_\beta s_W & M_z c_\beta s_W \\ 0 & M_2 & M_z c_\beta s_W & M_z c_\beta s_W \\ -M_z c_\beta s_W & M_z c_\beta s_W & 0 & -\mu \\ -M_z c_\beta s_W & -M_z c_\beta s_W & -\mu & 0 \end{pmatrix} \tag{2.11}$$

Mass eigenstates of $\tilde{\chi}^0$ Eq 2.12 can be obtained by diagonalizing the mass matrix with a unitary matrix "U".

$$U^* M_{\tilde{\chi}^0} U^{-1} = \begin{pmatrix} \tilde{\chi}_1^0 & 0 & 0 & 0 \\ 0 & \tilde{\chi}_2^0 & 0 & 0 \\ 0 & 0 & \tilde{\chi}_3^0 & 0 \\ 0 & 0 & 0 & \tilde{\chi}_4^0 \end{pmatrix} \tag{2.12}$$

Mass comparision in ascending order is $m_{\tilde{\chi}_1^0} < m_{\tilde{\chi}_2^0} < m_{\tilde{\chi}_3^0} < m_{\tilde{\chi}_4^0}$ and $m_{\tilde{\chi}_1^\pm} < m_{\tilde{\chi}_2^\pm}$. The lightest neutralino ($\tilde{\chi}_1^0$) in R parity conserving MSSM could be the lightest supersymmetric particle (LSP) and stable. The definition of R parity is given in Eq. 2.13 where j is spin, B is baryon number and L is lepton number. As a consequence of R parity conservation, every interaction point has an even number of SUSY particles.

$$R = (-1)^{2j+3B+L} \tag{2.13}$$

$$\mathcal{L}_{m_{\tilde{\chi}^\pm}} = \frac{-1}{2} (\psi^\pm)^T M_{\tilde{\chi}^\pm} \psi^\pm + h.c. \tag{2.14}$$

In a similar manner, chargino mass eigenstates can be obtained too. The chargino mass term in the langrangian is given in Eq 2.14 where $M_{\tilde{\chi}^0}$ is 2×2 mass matrix (given in Eq 2.15) and $\psi^\pm$ = $\tilde{W}^+$, $\tilde{H}_u^+$ $\tilde{W}^-$, $\tilde{H}_d^-$. Mass eigenstates is

related to gauge eigenstate in such a way shown in Eq 2.16 where U^1 and U^2 are unitary matrices. Two unitary matrices are needed to diagonalize the mass matrix since $M_{\tilde{\chi}^{\pm}}$ is not symmetric. After diagonalizing the mass matrix with the unitary matrices, mass eigenstates of charginos are obtained.

$$M_{\tilde{\chi}^{\pm}} = \begin{pmatrix} M_2 & \sqrt{2}M_W s_\beta \\ \sqrt{2}M_W c_\beta & -\mu \end{pmatrix} \tag{2.15}$$

$$\begin{pmatrix} \tilde{\chi}_1^{\pm} \\ \tilde{\chi}_2^{\pm} \end{pmatrix} = U^{1,2} \begin{pmatrix} \tilde{W}^{\pm} \\ \tilde{H}_{u,d}^{\pm} \end{pmatrix} \tag{2.16}$$

Composition of $\tilde{\chi}_1^0$ plays a very important role in order to get correct Dark matter relic density observed by astronomers [18]. If the LSP is mostly Bino then the annihilation cross section is too small to fit the observed relic density, however, if it is mostly Higgsino with a mass around 1 TeV [27] or wino with a mass of 2.5 TeV then the annihilation cross section is too large.

The LSP is a natural candidate for the dark matter [28, 29, 30]. However, for all of its attractive features, there are no experimental signs yet of its existence. Current SUSY mass limits now reach as high as ~2 TeV for gluinos in certain scenarios [31]. It could be because SUSY has a more challenging nature.

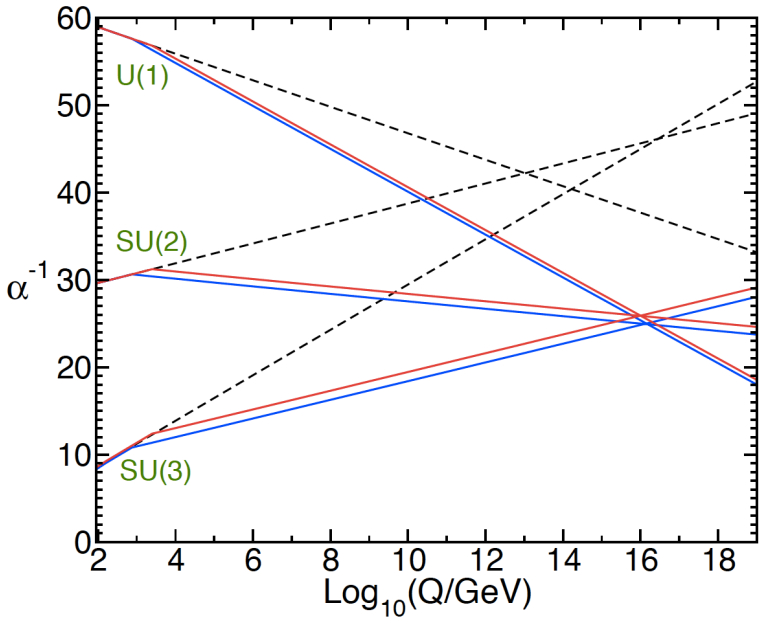

Figure 2.5: Inverse of the three different force coupling represented by dot lines do not unify at GUT scale with SM whereas coupling represented by solid lines meet at the GUT (10^{16} GeV) with SUSY. Reprinted from [3]

2.2.1 Search Strategy in VBF

Many SUSY searches have been carried out by ATLAS and CMS experiment and both put bounds on gluinos ($\tilde{g}$) and squarks ($\tilde{q}$) and their masses are ruled out up to ~2 TeV and ~1.5 TeV respectively at 95% CL [32]. One way to search for charginos/neutralinos (electroweakinos) is cascade decay of colored particles, however colored particles are heavy and the production cross section is limited thus searches should be devised to direct production of electroweakinos via vector boson fusion (VBF). The SUSY search strategy using events with dijet in the VBF topology at the LHC has been suggested in Refs [33, 34, 35].

VBF production is characterized by the presence of two highly energetic jets in the opposite hemispehere with large rapidity gap $\Delta\eta$ and large dijet invari-

ant mass. Figure 2.6 shows VBF production of chargino-chargino ($\tilde{\chi}_1^{\pm}$-$\tilde{\chi}_1^{\pm}$) and chargino-neutralino ($\tilde{\chi}_1^{\pm}$-$\tilde{\chi}_2^{0}$) with their decays to leptons and LSP in the final state. The large $\Delta\eta$ gap and $\eta_{j1} \times \eta_{j2} < 0$ requirement between jets make signal stand out while reducing the SM background significantly.

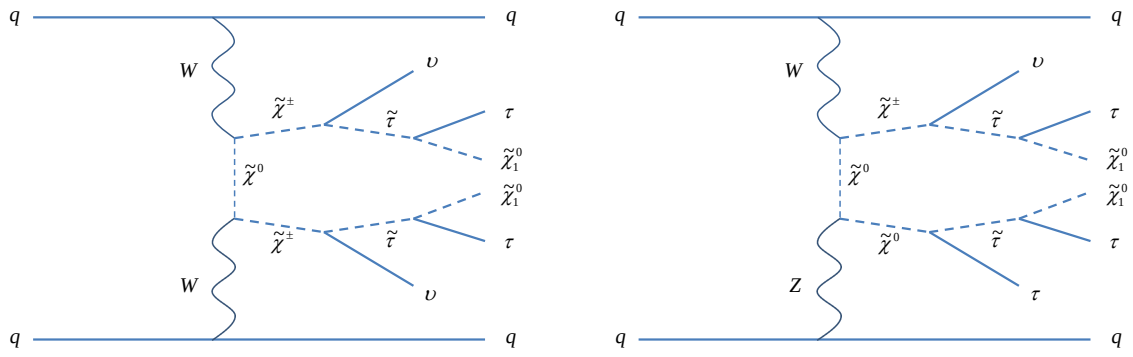

Figure 2.6: Representative Feynman diagram for VBF production of chargino-chargino pair production in VBF process (left), and chargino-neutralino pair production (right). Reprinted from [4]

I propose the search for charginos and neutralinos in the VBF topology in events with one soft lepton (electron) + Missing Energy + VBF Jets, where soft leptons are a key signature. The search in VBF topology offers a direct probe to the electroweakinos in the compressed mass spectra in which we target unexplored regions of SUSY parameter space, where other searches have limited sensitivity.

2.2.2 Review of Run-I Analysis

2.2.2.1 Search for Charginos/Neutralinos Using the VBF Processes

We searched for SUSY signatures with 8 TeV data in a final state with leptons, E_T^{miss} coming from the LSP and 2 VBF jets for two scenarios where $\tilde{\chi}_1^{\pm}$ and $\tilde{\chi}_2^0$ are mass degenerate with $\tilde{\chi}_1^0$ called "compressed-mass-spectrum" and large mass gap scenario in which we have $m_{\tilde{\chi}_1^0} = 0$ [4]. Compressed mass spectrum targets unexplored regions of SUSY parameter space, where other searches have limited sensitivity (see red region in Figure 2.7).

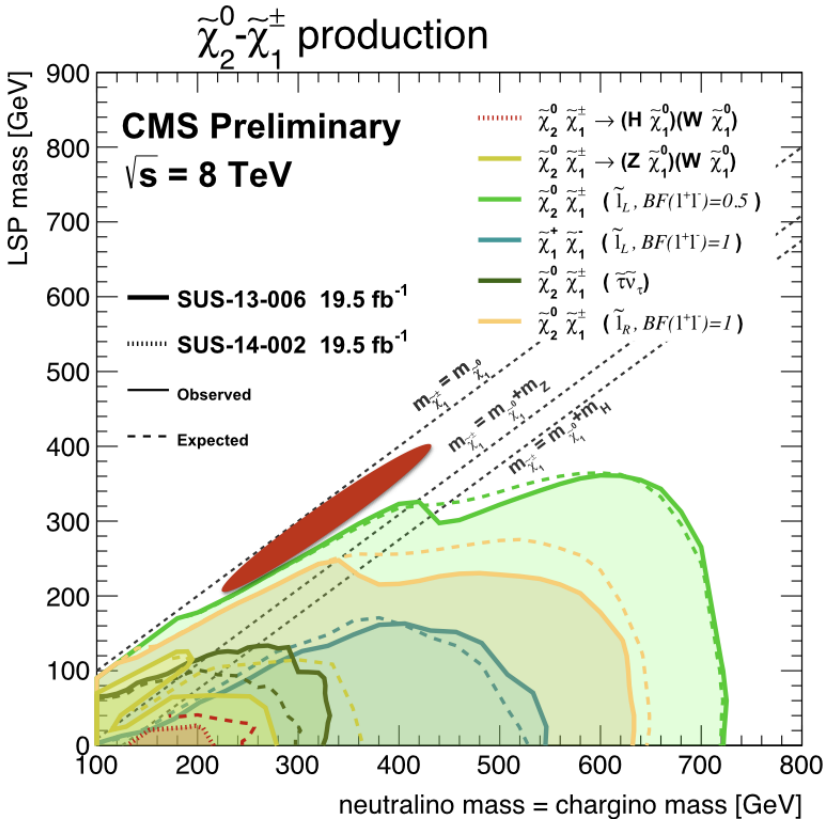

Figure 2.7: Observed limits for electroweakino searches with 8 TeV data. Reprinted from [5]

Figure 2.8 on the left shows the invariant mass distributions of two jets in VBF topology for events with two leptons, comparing between the data and the SM expectation [4]. Upper limits are set on the cross sections for pair production of charginos and neutralinos with two associated jets, assuming the supersymmetric partner of the lepton to be the lightest slepton and to be lighter than the lightest chargino. The data sample corresponds to an integrated luminosity of 19.7fb^{-1} at 8 TeV recorded by the CMS detector. Figure 2.8 on the right shows the observed limit on cross sections for two scenarios. For a compressed mass-spectrum scenario in which the mass difference between the $\tilde{\chi}_1^0$ and the next lightest, mass-degenerate, gaugino particles $\tilde{\chi}_1^{\pm}$ and $\tilde{\chi}_2^0$ is 50 GeV, the lower mass limit of 170 GeV is set for $\tilde{\chi}_1^{\pm}$ and $\tilde{\chi}_2^0$. This scenario was not excluded by the latest CMS analyses in the trilepton channel [36]. For the large mass gap scenario where $m_{\tilde{\chi}_1^0} = 0$ GeV, we excluded mass of $\tilde{\chi}_1^{\pm}$ and $\tilde{\chi}_2^0$ to below 270 GeV.

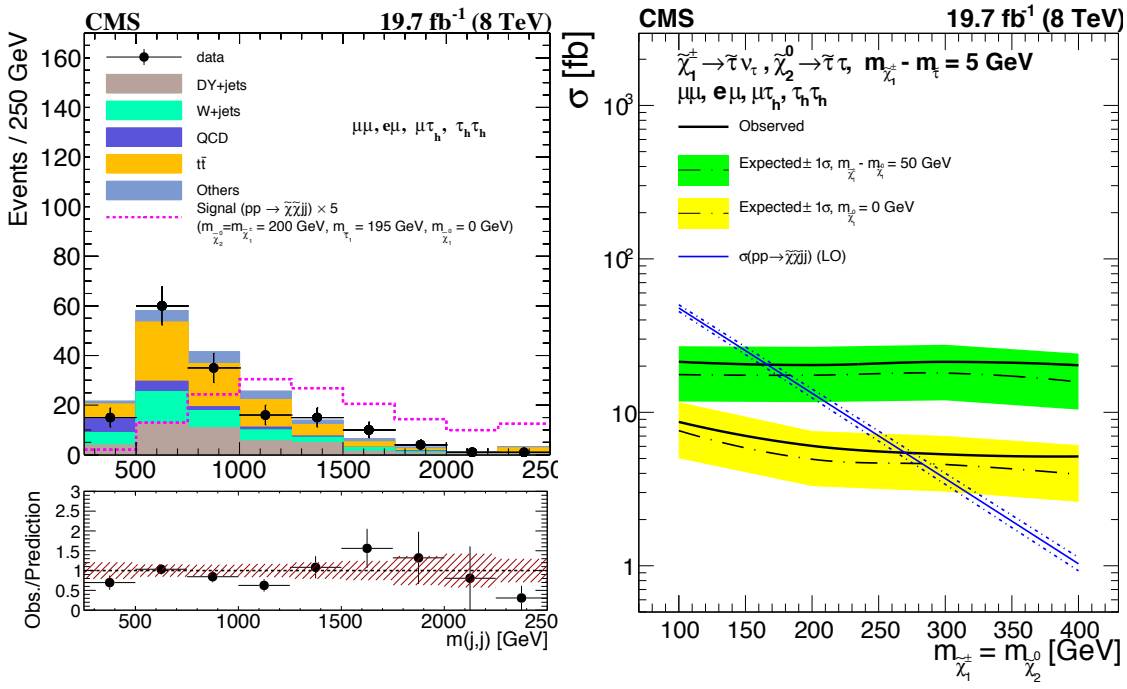

Figure 2.8: Left: dijet mass distribution after combining all 8 channels. There is a good agreement between data and MC. Right: observed and expected limits on mass of $\tilde{\chi}_1^{\pm}$ and $\tilde{\chi}_2^0$ for two different scenarios after combining all channels. Reprinted from [4]

3. THE LARGE HADRON COLLIDER & COMPACT MUON SOLENOID DETECTOR

This dissertation work is based on Compact Muon Solenoid (CMS) experiment which has been carried out at the Large Hadron Collier (LHC). Both the LHC and CMS detector will be detailed in the next sections.

3.1 The Large Hadron Collider

The Large Hadron Collider [37] located at European Organization for Nuclear Research (CERN) is the largest accelerator ever built in order to recreate the moment right after the big bang occured. It is located 100 metres underground near Geneva, Switzerland and has a circumference of 27 km. From 2010 until 2012, proton-proton collisions were taking place initialy at $\sqrt{s}$ = 7 TeV and then increased to 8 TeV before shutdown.

The accelerator is hosting four major experiments where beams collide, two of which are the general purpose experiments ATLAS (A Toroidal LHC ApparatuS) [38] and CMS, also B physics experiment LHCb (Large Hadron Collider beauty) [39] and heavy ion experiment ALICE (A Large Ion Collider Experiment),[40]. Before the protons collide, the LHC accelerates proton beams in opposite directions at speeds very near the speed of light.

As seen in Figure 3.1, protons obtained from Hydrogen atoms are sent to Proton Synchrotron (PS) for an initial acceleration. Then, accelerated beams are injected into Super Super Proton Synchrotron (SPS). After both beam energies have reached 450 GeV, they are transferred to the LHC in order to accelerate the protons to the center-of-mass energy of $\sqrt{s}$ = 13 TeV. During the acceleration, superconducting dipole magnets with a field strength of 3.8 Tesla are used to

keep the beams traveling along the beam pipe.

Although the initial rate of bunch crossings was 20 MHz at the beginning of Run II, We now have data from collisions happening every 25ns, corresponding to a bunch crossing frequency of 40 MHz.

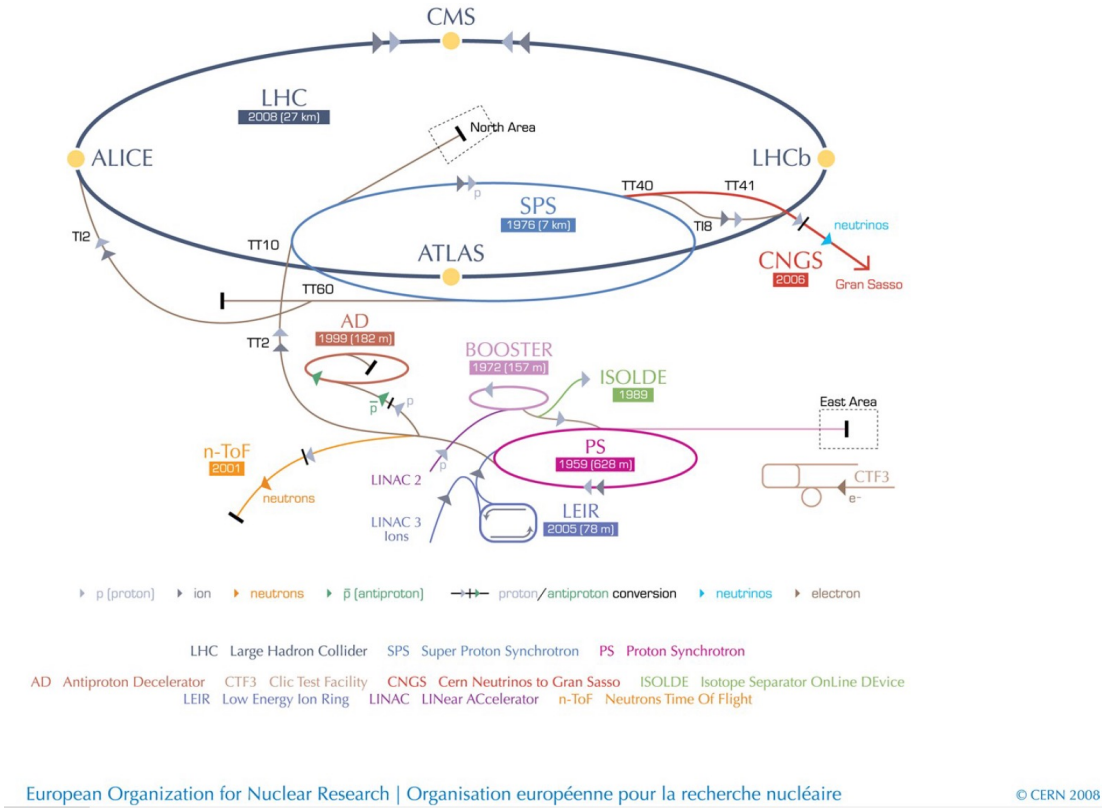

Figure 3.1: Large hadron collider. Reprinted from [6]

3.2 Compact Muon Solenoid Detector

The Compact Muon Solenoid (CMS) detector [7] is one of the four general-purpose particle physics detectors built on the Large Hadron Collider (LHC) beamline at CERN. It is also the second largest detector after ATLAS. Although there are differences between those two detectors in terms of magnet system

and tracking system, both aim to understand the properties of the Higgs boson, whose discovery was announced in 2012 by both the CMS and ATLAS collaborations, to search for the source of matter antimatter imbalance in the universe, and to look for new physics such as extra dimensions, dark matter, etc.

The CMS detector is 21.6 metres long, 15 meters in diameter, and weighs about 14 kilo-tonnes. Compared to the ATLAS detector CMS is smaller but twice as heavy as ATLAS. Although other detectors at the LHC have been built inside the LHC tunnel, CMS detector is assembled underground after its sections have been built outside. The most important characteristics of the CMS detector which make it different from other three detectors are that it has a great muon, electron, photon identification and resolution, along with great di-jet mass reconstruction, all of which are crucial for new physics discoveries beyond the Standard Model where identification of decay products and their momentum is vital.

The CMS experiment started in 2008 and completed the Run I in 2012. After upgrading the CMS detector, the experiment re-started in April 2015 with collisions happening every 50 ns at 13 TeV. In order to handle this big number of events, the CMS detector is making use of materials which have good time resolution in order to distinguish an interaction from the another interacton in the next bunch crossing. The CMS detector also has trigger system which decides quickly which events need to be kept which ones need to be thrown away in order to save disk space.

The CMS detector is comprised of sub-detectors, including a silicon tracker in the inner most part of the detector, an electromagnetic calorimeter (ECAL) surrounded by a hadronic calorimeter (HCAL), a magnet system generating magnetic field of 3.8 Tesla, and a muon system located at the most outer part of the CMS detector, as shown in Fig 3.2.

Besides the performance concerns, the sub-detectors must also have a high radiation tolerance. High levels of radiation can cause the sensitive electronics to break or have single event upsets (SEU), or fake signals. Because of this, the on-detector components are carefully chosen to minimize detector based errors.

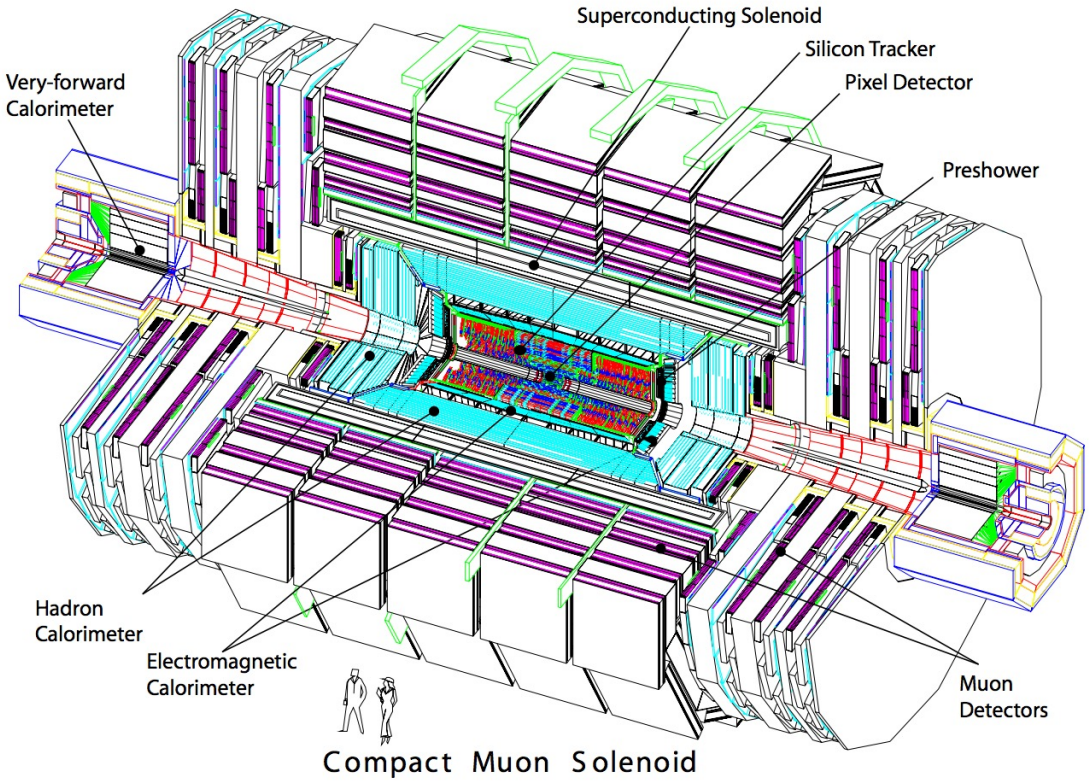

Figure 3.2: Cross section of the CMS detector. Reprinted from [7]

3.2.1 The CMS Coordinate System

The CMS experiment uses a right-handed coordinate system. The x axis points to the centre of LHC ring, the y axis points up to the surface, and the z axis points counterclockwise in the direction of the beamline. In addition to

the Euclidian coordinate system, CMS also makes use of a cylindrical coordinate system where the azimuthal angle ϕ is measured from the x-axis in the xy plane and the radial coordinate in this plane is denoted by r (see Figure 3.3). The polar angle θ is defined in the rz plane and the pseudorapidity is given by $\eta = \ln \tan \frac{\theta}{2}$.

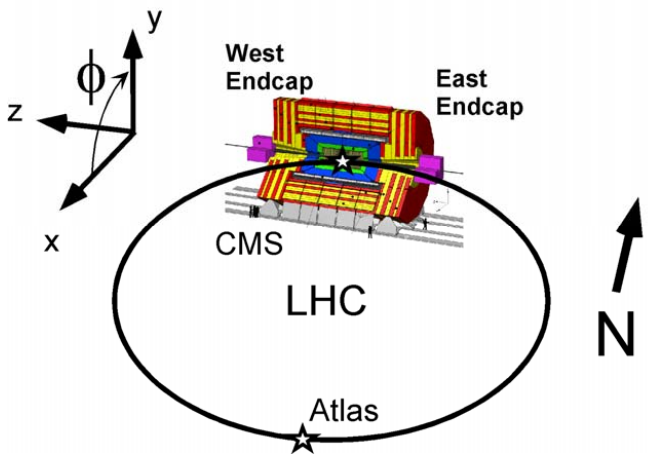

Figure 3.3: CMS coordinate system

3.2.2 Superconducting Magnet

One of the most important parts of the CMS detector is the solenoid magnet surrounding the tracker and the calorimeters. This powerful superconducting magnet, which produces a magnetic fields of 3.8 Tesla, about 100,000 times that of the earth's magnetic field, is 13 m long and 5.9 m in inner diameter. Having such a powerful magnet makes the CMS detector different from other detectors. A high magnetic field is very important in order to bend charged particle, espcially muons, so that the momentum of particle can be measured precisely.

In order to produce such a huge magnetic field, 2168 windings of Niobium-Titanium (NbTi) conductor are used. The number of turns N is proportional to

magnetic field as seen in the formula 3.1. Some of the important parameters for the solenoid magnet are shown in the table 3.1.

$$B \sim \mu \frac{N}{L} I \tag{3.1}$$

Table 3.1: Some of the parameters of superconducting magnet of CMS detector. Reprinted from [17]

Parameter	Description
Magnetic Field	3.8 T
Magnetic Length	12.5 m
Stored Energy	2.6 GJ
Nominal Current	19.14 kA
Inductance	14.2 H
Operating Temperature	1.8 K
Barrel Length	13 m
Inner Diameter	5.9 m
Weight	220 tons

3.2.3 The Tracker

The inner most part of the CMS detector is occupied by the tracking system, which helps us to reconstruct path of the charged particles such as muons, electrons and hadrons, as well as to measure their momentum. High momentum particles leave a more straight track in the tracker whereas low momentum particles have more curved path. In order to calculate the momentum, we can use equation 3.2. It is nothing but centripetal force and force on the charged particle moving in the magnatic field where P is momentum of the particle, R is radius

of the track in the tracker and q is the charge of the particle.

$$\mathbf{F} = \frac{mv^2}{R} = qvB \Rightarrow mv = \mathbf{P} = qBR \tag{3.2}$$

Since the tracker is located in the core of the detector, it is exposed to the most radiation. Thus it must be made of a radiation hard material which can also provide a resolution down to the 10 µm level. The CMS tracker is made completely out of silicon, which is the first time this has been attempted for a particle detector. Because this is a solid state tracker, special care was taken to reduce the amount of material so that the tracker itself would interact with the particles as little as possible. The tracker needs to record particle paths accurately yet be lightweight so as to not disturb the particle's trajectories as little as possible so that equation 3.2 can be used for an unaltared path. It does this by taking position measurements so accurate that tracks can be reliably reconstructed using just a few measurement points. Each measurement is accurate to 10 µm, a fraction of the width of a human hair. It is also the inner most layer of the detector and so receives the highest volume of particles: the construction materials were therefore carefully chosen to resist radiation.

The tracking system is made of two parts, the pixels and the silicon microstrip detectors which surround them. The tracking system in the barrel section and end cap region is seen in Figure 3.4. In the barrel section there are three layers of pixel detectors and ten layers of strip detectors, four of which are double-sided (blue-colored) and rest are single sided (red colored). The endcap section consists of two pixel layers and twelve strip layers.

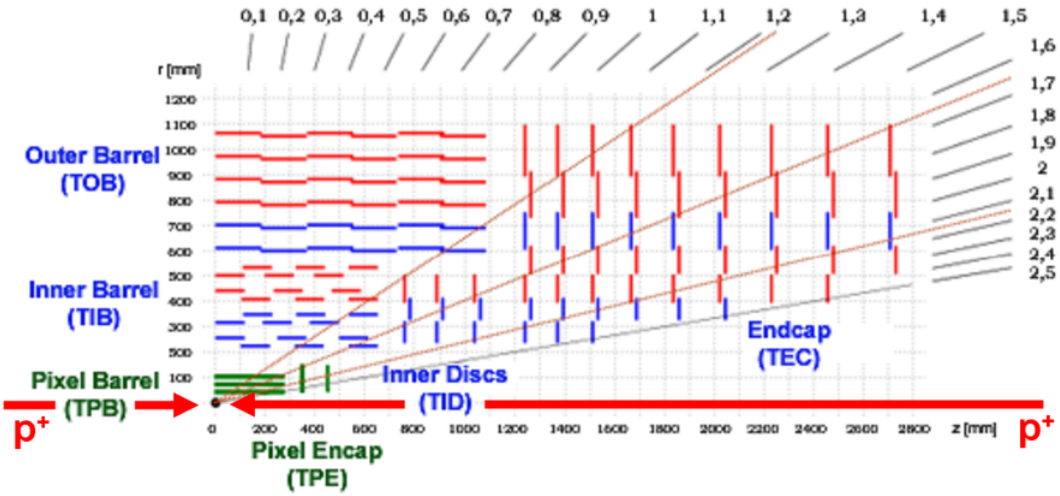

Figure 3.4: Tracking system at CMS detector. Reprinted from [8]

3.2.3.1 Pixel Tracker

As seen in the Figure 3.5, the inner tracking system consists of three layers in the barrel section and are located at radii of 4.4 cm, 7.3 cm and 10.2 cm. In the endcap sections there are two layers per side, which are located at $|z| = 34.5$ cm and 46.5 cm.

Being so close to the primary vertex, makes it vital for reconstruction of the track of short lived particles emerging from the collision. The pixel tracker is designed in a way to be able to withstand radiation for the duration of the experiment, about 10 years. It is made of completely from silicon and consist of 65 million pixels shape of $100 \times 150\ \mu m$.

After a charged particle hits the tracker, electron is kicked out of the silicon atom, which in turn creates electron-hole pairs or small electric signal. This signal is amplified by silicon readout chip (ROC) attached to the each single pixel (See Figure 3.6). Because the pixel tracker consists of multiple layers, we can construct

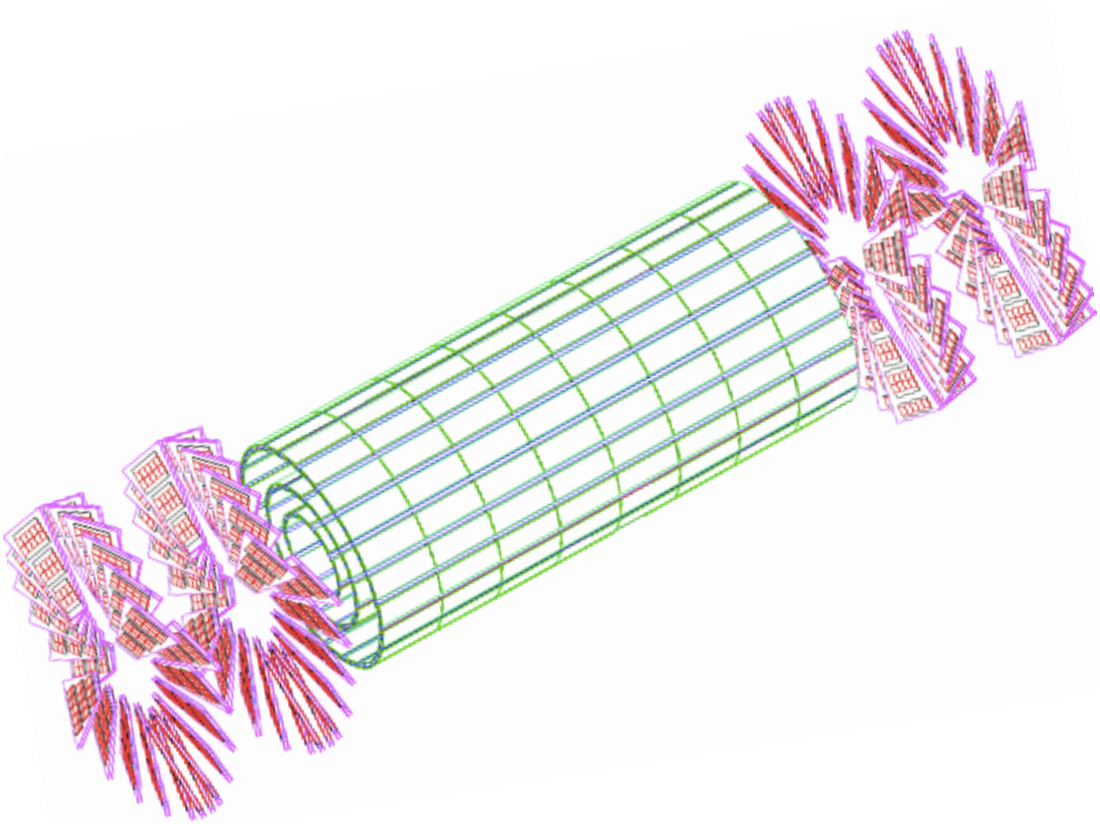

Figure 3.5: Pixel detector layers in the barrel and endcap section of CMS detector. Reprinted from [9]

a three dimensional picture of the particle trajectory with high precision.

3.2.3.2 Strip Tracker

The silicon strip tracker is located in both barrel and endcap region of the detector. In the barrel section it has ten layers, while in the endcap region it has 12 layers. As seen in Figure 3.4, the barrel region is comprised of two parts: The tracker inner barrel (TIB), made up of four layers having coverage up to $|z| < 65$ cm, and the tracker outer barrel (TOB), which contains 6 layers of detectors with coverage up to $|z| < 110$ cm.

The endcap region is divided into two parts, which are tracker end cap (TEC)

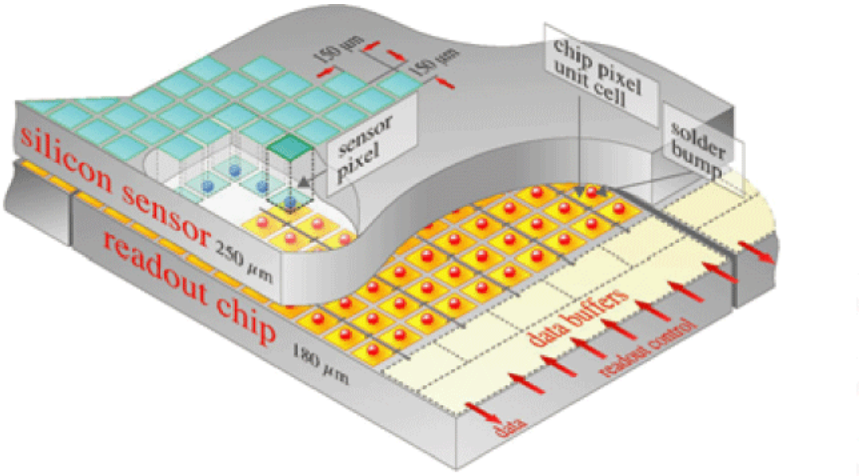

Figure 3.6: Layout of the pixel detectors and read-out chips. Reprinted from [10]

and tracker inner disks (TID). The TEC contains 9 disks in the region of 120 cm< |z| < 280, whereas the TID has 3 disks located in the gap between the TIB and the TEC. In total, the strip tracker is composed of 9.6 million strips.

3.2.4 The Electromagnetic Calorimeter

In order to measure energy of particles of interest (electron and photon) after collision, calorimeters are made use of at the CMS. Electromagnetic calorimeter (ECAL) is one two calorimeters. The CMS ECAL is comprised of lead tungstate crystals $PbWO_4$ (See Figure 3.7) due to its short radiation length and radiation hardness [9].

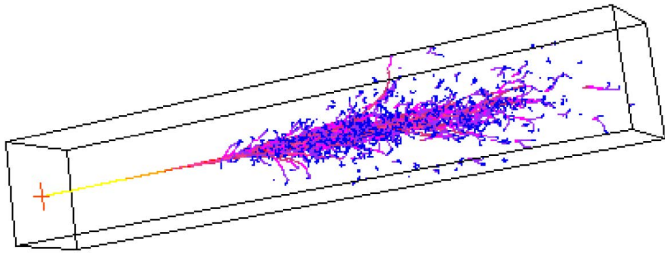

Figure 3.7: Simulated electromagnetic shower in a lead tungstate crystal. Reprinted from [9]

The ECAL is divided into two sections: barrel (EB) and endcap (EE) (see Figure 3.8). The EB section has 61200 crystals that form 36 supermodules and have a coverage of $|\eta| < 1.479$. The endcap region has 15000 crystals and extends $|\eta| < 3.0$. Pre-shower detectors are also located in the endcap region in order to distinguish single highly energetic photons from less energetic pairs of photons. Silicon photo-detectors on the backs side of the ECAL crystals are used in order to detect the scintillation light, electrical signal after electron or photon creates shower in crystals.

3.2.5 The Hadron Calorimeter

The second calorimeter inside the CMS detector is the hadron calorimeter (HCAL), which is made of brass absorber and plastic scintillator, both of which have good radiation hardness. The HCAL is a sampling calorimeter which means the materials used for showering and measuring the particles's energy is distinct from each other. It is used to measure the position and energy of hadrons, which are themselves made of quarks and gluons.

The HCAL is located outside of the ECAL and completely surrounds it. It is divided into four parts as shown in Figure 3.9: barrel (HB), outer (HO), endcap

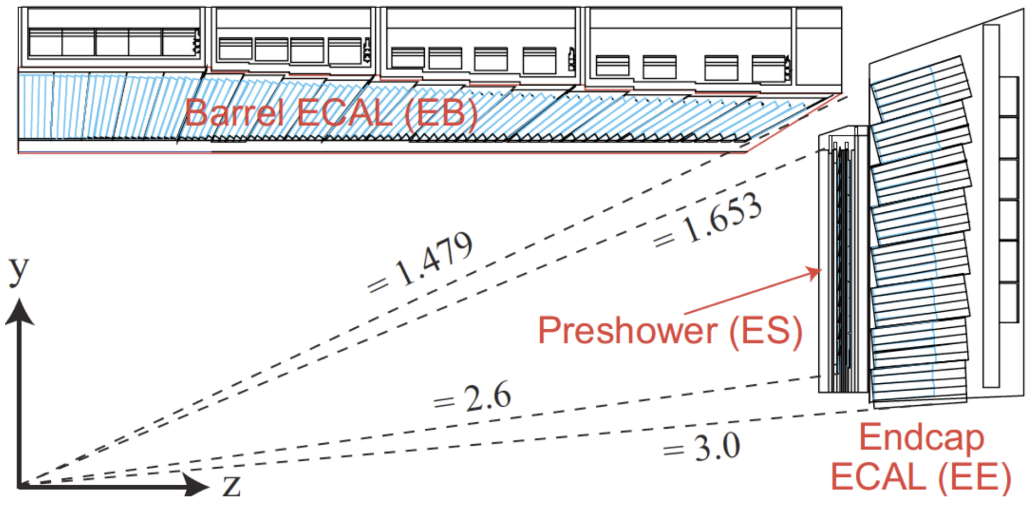

Figure 3.8: Cross section of ECAL. Reprinted from [9]

(HE) and forward (HF). The HB covers the range of $|\eta|$ <1.4 and is segmented into 2304, towers each of which covers an angle of $0.087^{\circ} \times 0.087$ in the $\phi - \eta$. The HE, on the other hand, covers the range of $1.3 < |\eta| < 3.0$. The HF is located 112 cm away from the collision point and covers the range of $3.0 < |\eta| < 5.0$ where mostly energetic jets, which are crucial for VBF processes, are present and consists of towers covering an angle of $0.175^{\circ} \times 0.175$ in the $\phi - \eta$. Lastly, the HO is located in the barrel section and outside of the magnet coil and is designed to catch any undetected particles, except for muons, which may penetrate through the HB and solenoid.

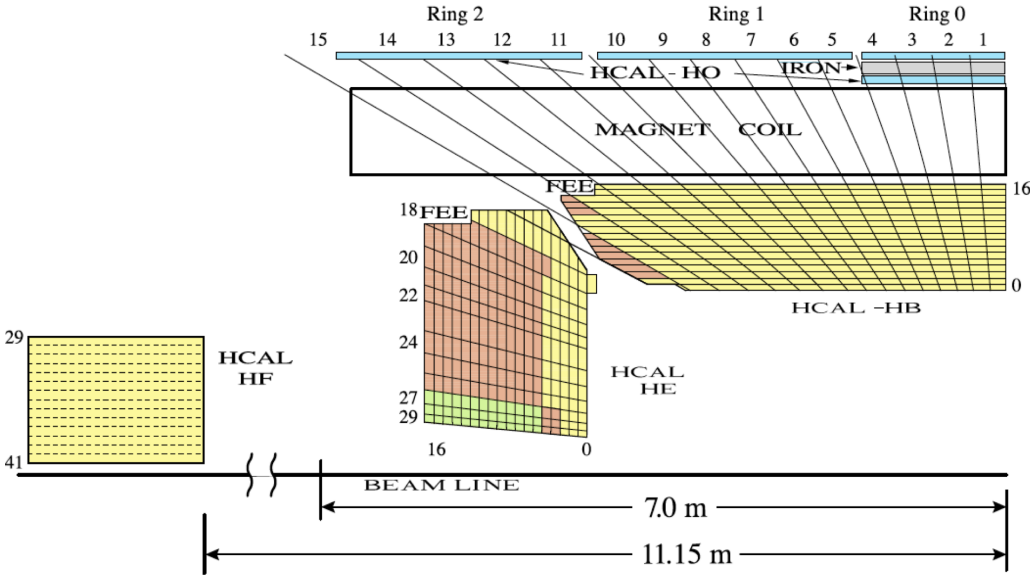

Figure 3.9: A quadrant of the HCAL. Reprinted from [11]

3.2.6 The Muon System

Muon reconstruction is a crucial task for investigating new physics, which is why it is one of the namesake components for the CMS detector. As such, the subsystem involved in measuring muons is one of the most advanced muon spectrometers ever constructed. It can provide very precise position and momentum measurements while still being fast enough to be involved in trigger decisions. It is located in the outer part of the CMS detector, interleaved with the iron return yoke. Muons a able to penetrate through a significant amount of material before interacting, which is why the muon chambers are located outside the solenoid magnet. The muon detectors are illustrated in Figure 3.10. The system consists of drift tubes (DT) in the barrel region, resistive plate chambers (RPC) in the barrel and endcap regions, and cathode strip chambers (CSC) in the endcap regions. In addition to the three current detector types in the muon subsystem, CMS has

approved the installation of GEM (gas electron multiplier) detectors at station 1 during second and third long shutdown. CMS also plans to install another muon detectors called ME0 (muon endcap station 0) in the very forward region of the CMS detector, however both GE2/1 and ME0 have yet to be fully approved.

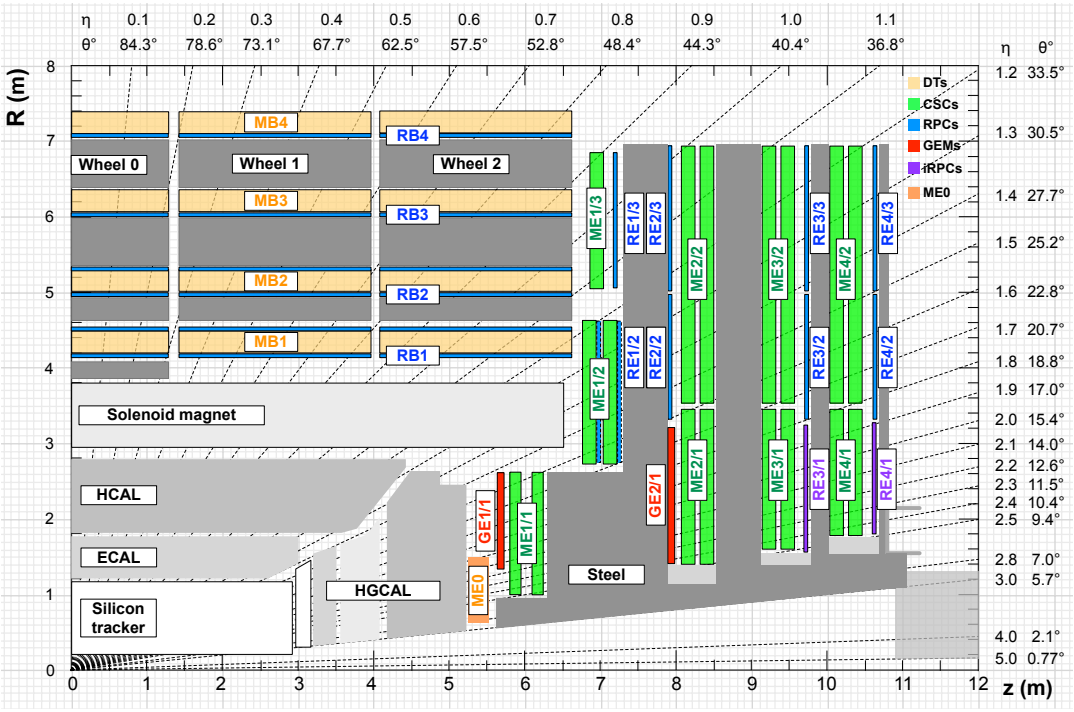

Figure 3.10: Muon system in the CMS detector.

3.2.6.1 Drift Tube Chambers

There are a total of 250 drift tubes located in the barrel section of the CMS detector with a coverage of $|\eta| < 1.2$. The DTs are ideally suited to this region because of the uniform magnetic field in the barrel section, low neutron flux, and the small muon rate.

The DT region is comprised of 4 stations which are located at 4.0, 4.9, 5.9 and

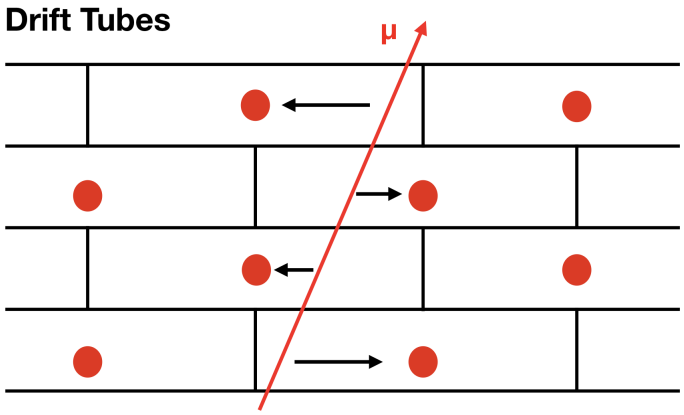

Figure 3.11: Illustration of drift tube chamber.

7.0 meters from the z-axis. The DT's are located in a such way that a muon will pass through at least three out of four stations. Each one is coupled to one or two RPCs in the barrel region for better resolution in muon reconstruction.

Figure 3.11 is an illustration of a drift tube. Each chamber is 2×2.5 meter in size and has 12 layers grouped every four into 1 and contains up to 60 tubes, each of which 4 cm wide. As seen in the Figure 3.11, When a muon passes through the chamber, it knocks out an electron from the gas molecules in the tube. Due to the electric field in the chamber, the electron moves towards the positively charged wire. An electron avalanche is created while the moving electron interacts with additional gas atoms, knocking out even more electrons. The trajectory of the muon is calculated using timing information from the pulses along the wires. The two most central tubes in Figure 3.11 measure the position of the muon parallel to beam line while the outer tubes measure the perpendicular coordinate.

3.2.6.2 Cathode Strip Chambers

Cathode strip chambers are located in the endcap region (having an eta coverage between 0.9 and 2.4 and perpendicular to the beam line.) where the magnetic

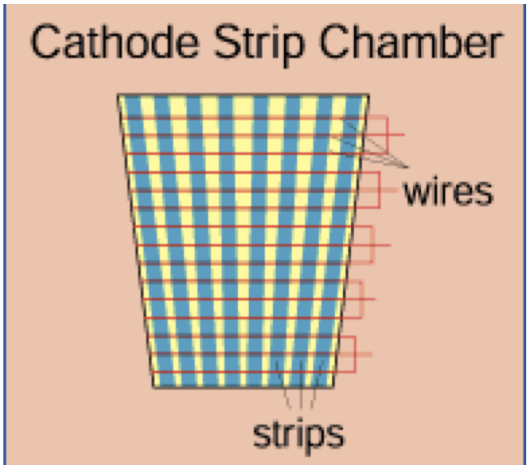

Figure 3.12: Illustration of cathode chamber.

field is not even and the muon rate is high. Radiation resistance and fast response time make CSCs preferable in the region. Each chamber is in trapezoidal shape and covers either 10° or 20° in ϕ. There are a total of 540 CSC's in four stations and each CSC contains six layers, which allows for a six coordinate measurement for every passing particle. Each CSC has a spacial resolution of 150 µm and a direction resolution of 10 mrad.

Figure 3.12 shows a depiction of a single CSC chamber. It is comprised of positively charged anode wires and negatively charged cathode strips, which are perpendicular to each other. This allows us to measure the position of the muon in two dimensions.

3.2.6.3 Resistive Plate Chambers

Resistive plate compliment the CSC and DT systems and are positioned in both the barrel and endcap regions with eta coverage $|\eta| < 1.6$. Each RPC is comprised of two parallel plates, separated with gas, which has highly electric resistant. There are a total of 480 RPCs. Compared to the CSCs and DTs, the

RPCs have a spacial resolution, but they provide a very good time resolution.

3.2.6.4 Gas Electron Multipliers

With upgrade plan of the LHC in 2018, integrated luminosity is estimated to reach around 300 fb^{-1} [12] and upgrade for muon system is going to be needed too in addition to the upgrades in other sub detectors so as to handle large amount of data. Gas electron multipliers (GEM) will be fourth kind of muon detectors, which is being planned to be installed during the second long shutdown. Although GEM detectors are not used of in this research, I took part in the simulation of the GEM detectors.

GEMs will be installed in a region in the HL−LHC where radiation rate is high since GEM has a good radiation robustness and expected to be in charge about 20 years under the high luminosity conditions. GEMs have a time resolution of 10 ns, angular resolution of 300 μrad, maximum geometric acceptance in a given CMS envelope and a maximum rate of 10 kHz/cm^2. These are all necessities for a muon system in the HL-LHC era [12].

Currently, there are two different GEM detectors called GE1/1 and GE2/1, which are located in the endcap region. "G" corresponds to GEM while "E" is corresponding to endcap. The first "1" in the name means station 1 whereas the second "1" indicates ring number. All of the simulation test are done for $GE1/1$ and the geometry is finalized. Two different GEM's in size, called long chamber and short chamber (see Figure 3.13), will be installed in the first station.

So far, several versions of the GE1/1 prototypes have been studied in detail at both CERN and Fermilab. The test GEMs were exposed to radiation tests and other beam tests over the last five years. $97-98\%$ detection efficiency is observed [12] with the current, final version (See Figure 3.13). GE2/1 is another type of

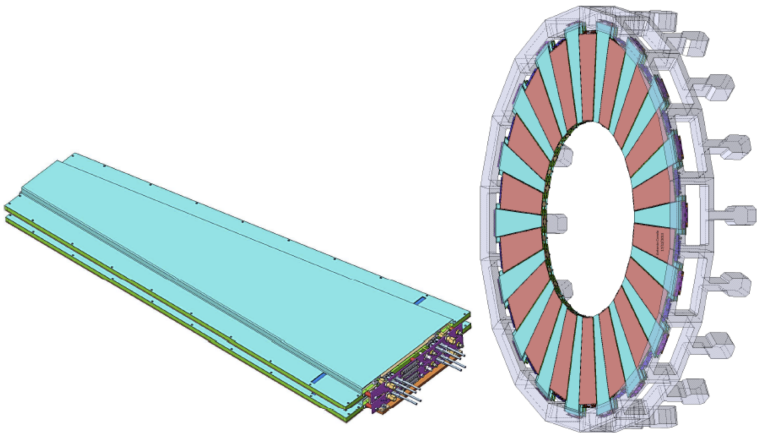

Figure 3.13: Left: a GEM superchamber. Right: layout of long and short GEM superchambers. Long chamber is located at 12 o'clock position and both long and short chamber have 8 η partitions. Reprinted from [12]

GEM chamber which will be installed in the first ring of station two after the third long shutdown. The geometry has yet to be finalized. The current geometry has a coverage of 20° in ϕ and eta coverage between 1.55 and 2.45.

As seen in Figure 3.15, each GEM chamber is comprised of three layers of GEM foils. Two of GEM chambers put together are called a GEM Superchamber. A total of 72 GEM (36 long chambers and 36 short chambers) will be installed in station 1 in each endcap. Each chamber will have 10.15° of coverage in ϕ as well as a coverage in eta between 1.55 and 2.2 (see Figure 3.10) approximately in 8 η partition. Each GEM chamber is comprised of three layers of GEM foils, which is a thin metal-clad polymer foil with both sides covered in 5 µm of copper. As shown in Figure 3.14 left, the surface of the clad has holes in a hexagonal pattern. Once a charged particle enters the detector, it begins to knock electrons out of the gas atoms between the GEM foils. The voltage applied between the copper layers creates an electric field in the holes, which accelerates electrons and continues to further ionize the gas atoms (see Figure 3.14). This processes generates an

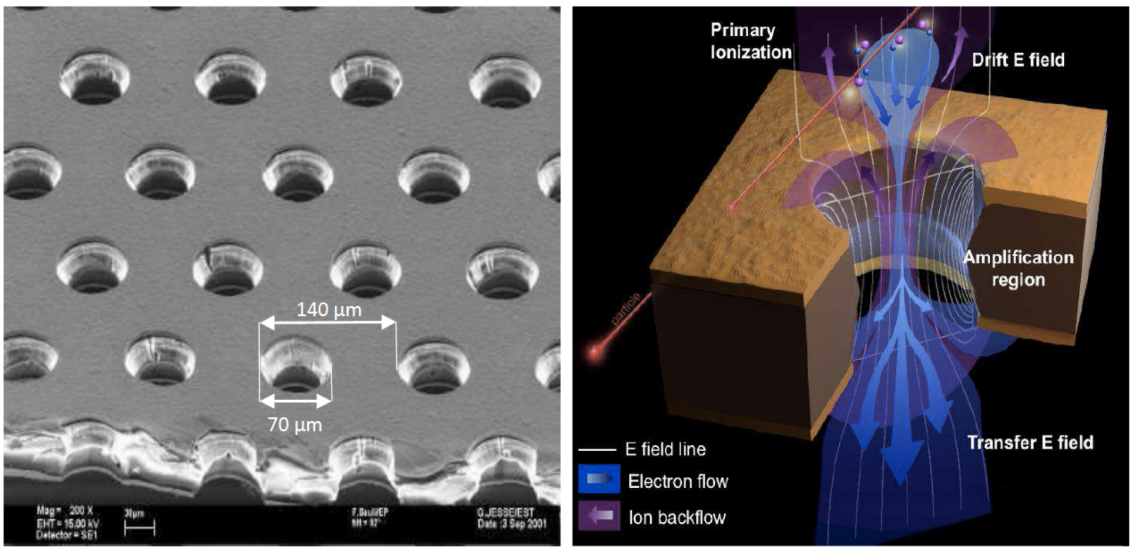

Figure 3.14: Left: picture of GEM foils. Right: a schematic view of electron flow and electric field through the holes. Reprinted from [12]

electron avalanche through the holes of three layer of GEM foils and induces an electric signal on the readout strips (see Figure 3.15).

3.2.6.5 ME0

Although the geometry has yet to be finalized, there is a plan to install another set of muon chambers, called, ME0, during the third long shutdown. These chambers will sit right behind the HE and will serve as near taggers for the muon system (see Figure 3.10). The current geometry contains six layers of triple GEM detectors and has a coverage of 20° in ϕ an eta coverage between 2.0 and 2.82. ME0 is located 527 cm away from the interaction point, has only one partition, and no strips.

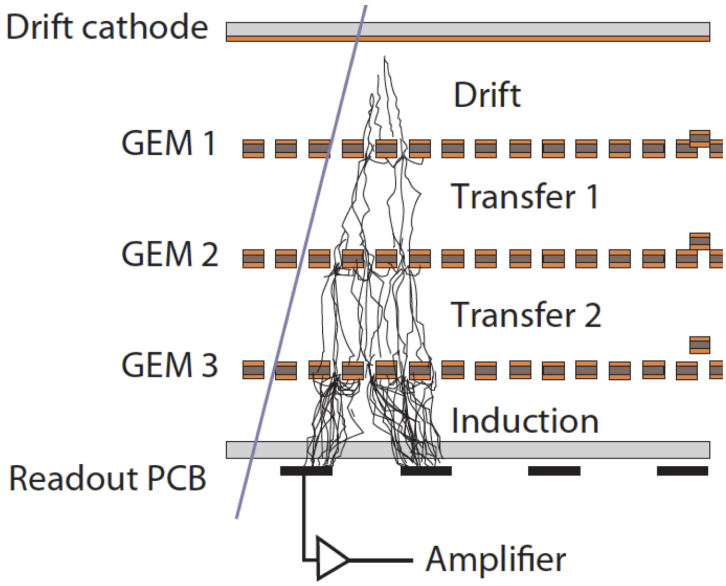

Figure 3.15: Illustration of working principle of a three layer GEM chamber. Reprinted from [12]

4. TRIGGER SYSTEM AT CMS

The Large Hadron Collider is designed to collide protons at a center of mass energy of 14 TeV and a luminosity of $10^{34}\text{cm}^{-2}\text{s}^{-1}$. Bunch spacing between beams is 25 ns corresponding to a bunch crossing rate of 40 MHz. In other words, approximately one billion of proton-proton collisions are produced every second. This billions of collisions might produce thousand of particles. In order to handle this huge data, trigger system is required for selecting only interesting events while rejecting the non-interesting events for offline analysis. Thus, CMS employs a two level of trigger system called Level-1 (L1) and High Level Trigger (HLT). First one is based on hardware, namely it consists of built of custom programmable electronics such as field-programmable gate arrays (FPGAs) and custom application-specific integrated circuits (ASICs) whereas the latter one is software based which uses more sophisticated algorithms.

4.1 Level-1 Trigger

Hardware based L1 trigger system is designed to reduce the rate from 10^9 Hz to 10^5 Hz. This L1 trigger system is a combination of independent tracker, calorimeters, and muon chambers' triggering systems and each independent trigger selects events whose detector signal is consistent with physics objects such as jet, missing energy etc. After an event passes one of those independent regional triggers, then the event is sent to the Global Trigger (see Figure 4.1) which decides to keep or reject the event for further processing.

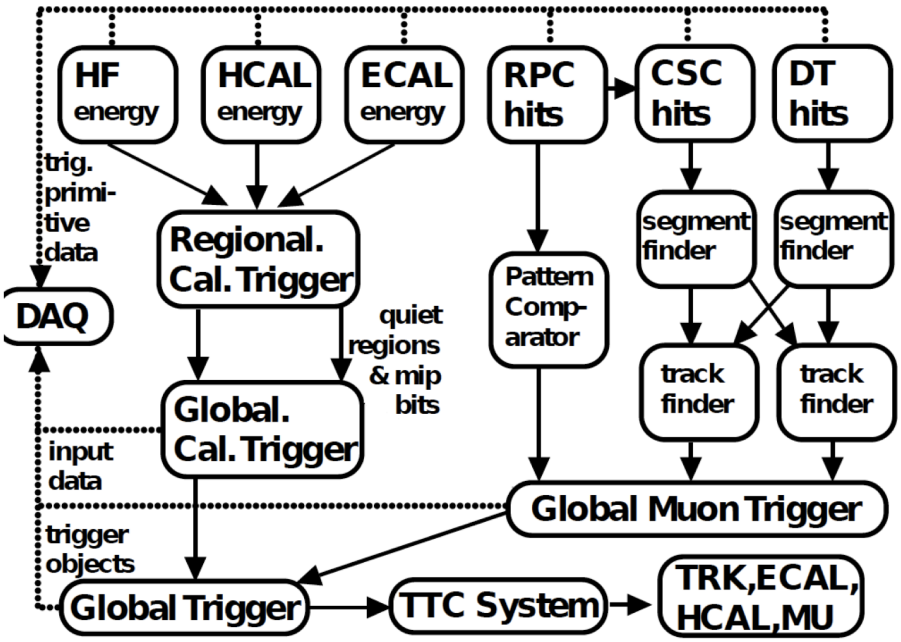

Figure 4.1: CMS level 1 trigger system. After events pass each independent detector's trigger, then events are sent to global muon/calorimeter triggers which combine the information and send to global trigger for final decision. Reprinted from [13]

4.2 High-Level Triggers

After passing the L1 trigger, final events for physics analysis are selected and stored on the grid after applying HLT. The event rate after applying HLT decreases approximately to $\mathcal{O}(10^2)$Hz. CMS deploys many HLT designed by various analysis groups for their needs. In this e+VBF analysis we use MET primary dataset (PD) since it is collected with MET trigger which is **HLT_PFMETNoMu120_PFMHTNoMu120_IDTight**.

The trigger efficiency is studied in a control region containing a high purity of $W(\rightarrow \mu\nu)$ + jets events. This is accomplished by using the single muon data sets, where events are selected with a single-muon trigger (**HLT_IsoMu24_eta2p1_v**) in order to define the denominator. In addition to the single muon trigger, we

applied $p_{\mathrm{T}} > 30$ GeV, $|\eta| < 2.1$, $E_T^{miss} > 50$ GeV and the VBF selections listed below.

1. at least two jets with $p_{\mathrm{T}} > 60$ GeV and $|\eta| > 5.0$
2. jets separated from the leptons by $\Delta R > 0.3$
3. All jets passing the above requirements and having:
   (a) $|\Delta\eta(j_1, j_2)| > 3.8$
   (b) $\eta_{j_1} \times \eta_{j_2} < 0$
   (c) $\mathrm{M}_{jj} > 1$ TeV

The numerator for the efficiency calculation is defined by additionally selecting the subset of those events that also fire the **HLT_PFMETNoMu120_PFMHTNoMu120_IDTight** trigger. Figure 4.2 shows the trigger efficiency as a function of E_T^{miss} for both data and MC backgrounds.

4.2.1 Mu+VBF High Level Trigger

As mentioned in the Section 2, we look for SUSY signatures with 8 TeV data in final states with dilepton + two VBF jets. Since low p_{T} leptons are crucial in SUSY searches in the case where mass difference between the lightest susy particle $\tilde{\chi}_1^0$ and gaugino particles $\tilde{\chi}_2^0$, $\tilde{\chi}_1^{\pm}$ is small (mass degenerate) we have developed a new dedicated mu+VBF trigger (HLT_Mu10_TrkIsoVVL_DiPFJet40_DEta3p5_MJJ750-_HTT350_PFMETNoMu60_v1) for LHC Run II, which allows us to reduce the p_{T}^{μ} threshold in the events in order to improve search sensitivity for SUSY compressed mass spectra regions. The mu+VBF trigger requires $E_T^{miss} > 60$ GeV, muons with a $p_{\mathrm{T}} > 10$ GeV, H_T greater than 350 GeV and two calorimeter jets with a $p_{\mathrm{T}} > 40$ GeV, a difference in pseudo$-$rapidity between these jets $\Delta\eta >$

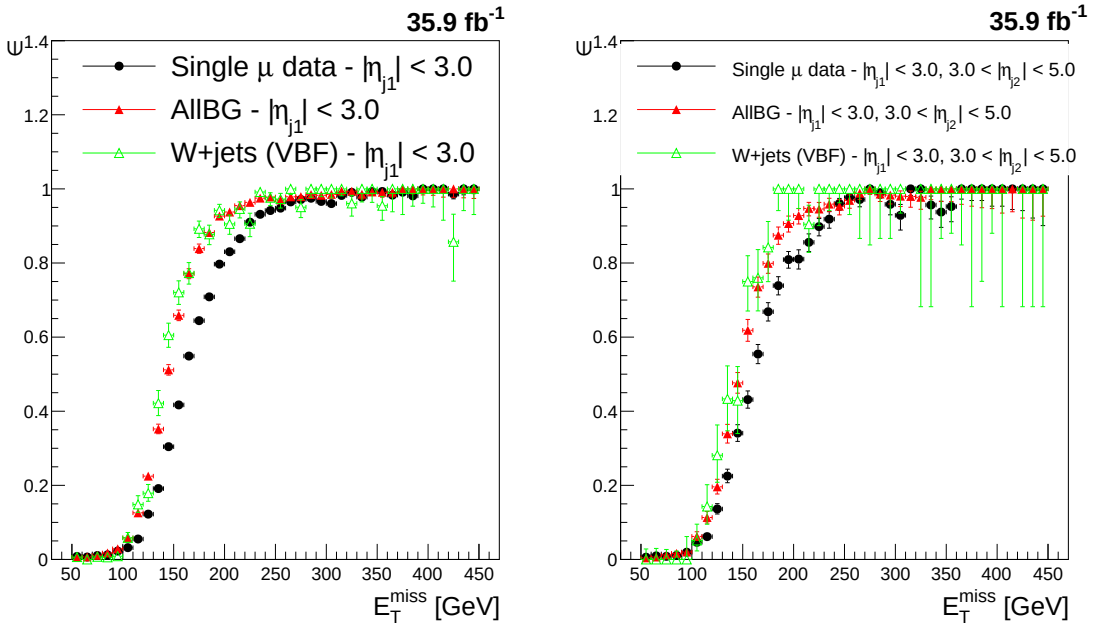

Figure 4.2: Left: trigger efficiency for monojet trigger as a function of E_T^{miss} in the case where both jets are central ($|\eta| < 3.0$). Right: shows trigger efficiency for monojet trigger as a function of E_T^{miss} in the case where one jet is central while the other one is forward ($3.0 < |\eta| < 5.0$)

3.5, and an invariant dijet mass of 750 GeV. In addition, the L1 seed used for this trigger is L1_Mu6_HTT100.

Since the trigger has multiple requirements, it is necessary to study the effect of each requirement independently. In order to study the trigger efficiency as a function of a specific variable, the requirement for that variable is loosened while assuring that events pass the rest of the requirements.

To study the trigger efficiency as a function of dijet mass, events satisfying the following requirements are analysed:

- $E_T^{miss} > 120$ GeV
- $H_T > 600$ GeV
- Muon $p_{\mathrm{T}} > 12$ GeV

The trigger efficiency as a function of m_{jj} is shown in Figure 4.3 (left).

To study the trigger efficiency as a function of E_T^{miss}, events satisfying the following requirements are analysed:

- $H_T > 600$ GeV
- $m_{jj} > 1200$ GeV
- Muon $p_{\mathrm{T}} > 12$ GeV

The trigger efficiency as a function of E_T^{miss} is shown in Figure 4.3 (right). We see the E_T^{miss} turns on around 150 GeV, which is better when compared to E_T^{miss} + VBF with a plateau around 300 GeV.

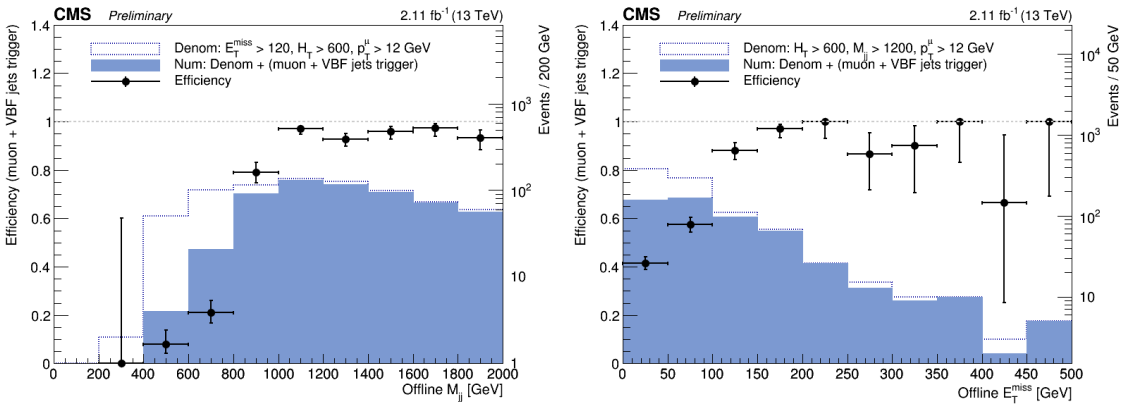

Figure 4.3: Left: mu+VBF trigger efficiency as a function of m_{jj}. Right: mu+VBF trigger efficiency as a function of missing transverse energy.

5. PHYSICS OBJECTS

After a proton-proton collision, outgoing particles leave hits in the various subsystems of the CMS detector. All of these hits are nothing but binary signals and need to be reconstructed for further data analysis. In Figure 5.1 we see the path of the particles as they travel through the magnetic field, away from the collision point. The radius of curvature of the charged particles will change depending upon their momentum and the sign of their charge. Neutral particles, however, are not affected by the magnetic field and do not leave any hits in the tracker.

Physics objects are reconstructed by using different algorithms relying on information from the sub-detectors. The reconstruction process for each of the physics objects is explained briefly in the following sections.

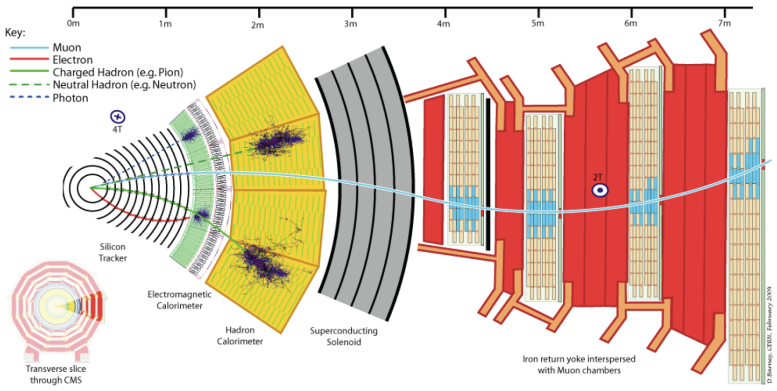

Figure 5.1: Transverse slice of the CMS detector and paths for several species of particles traveling in the magnetic field. Reprinted from [9]

5.1 The Particle Flow Algorithm

The particle flow algorithms [41] is used in order to reconstruct and identify particles such as muons, electrons, hadrons, and photons using information from all of the sub-detectors. For instance, this is done for muons by matching hits in the muon detectors to track in the tracker. As each particle is identified, the energy deposits and hits used to reconstruct this particle are removed from consideration for future particles. This avoids using the same hit or energy deposit for multiple particles. If energy deposits in HCAL and ECAL have no corresponding track pointing to those energy deposits, then remaining ECAL and HCAL deposits are a sign for neutral particles such as photon/ pion etc., which do not interact with tracker.

5.2 Jets

Due to quantum chromodynamics (QCD) confinement, colored particles (i.e. quarks, antiquarks, and gluons) cannot be bare, meaning they must be bound to other particles to form a colorless state. This process is known as hadronization. A collimated spray of these colorless objects is called a “jet." Over the years, many algorithms have been developed in order to reconstruct jets [42]. In this analysis we make use of the anti-k_T jet clustering algorithm [43] with a reconstruction cone R=0.4 ($R = \sqrt{\Delta\eta^2 + \Delta\phi^2}$). The anti-k_T jet clustering algorithm uses information from subdetectors as input. Jet quality criteria are also imposed to eliminate jets forming purely from noise. Jet energy corrections are applied in order to make sure that the energy used for analysis is that of the initiating parton, without being effected by detector inefficiencies or pileup. The L1Fastjet corrections seek to remove extra energy coming from pileup (PU) and the underlying event (UE), while the L2 Relative and L3 Absolute corrections seek to remove any detector

biases due to the p_T or η of the jet. Additional requirements, called PF jet ID, are placed on the jets used in this analysis. Only jets with $p_T^{Jet} > 30$ GeV and $|\eta|$ <2.4 are used. Table 5.1 shows additional selection criteria used for the recommended loose PF jet ID. The jet reconstruction and ID efficiency in simulation is $> 98\%$ for η. Figure 5.2 shows good agreement between data and MC after applying the ID requirements.

Table 5.1: Loose Jet-ID selections.

Selection	Cut
Neutral Hadron Fraction	< 0.99
Neutral EM Fraction	< 0.99
Number of Constituents	> 1
And for $\eta < 2.4$, $\eta > -2.4$ in addition apply	
Charged Hadron Fraction	> 0
Charged Multiplicity	> 0
Charged EM Fraction	< 0.99

5.3 Missing Transverse Energy

The total momentum of the scattering partons from the beam is unknown. However, because the protons do not travel perpendicular to the beam axis, the initial momentum of the partons in the transverse plane ($\vec{p}_T$) is equal to zero. Missing transverse momentum, $\vec{p}_{\mathrm{T}}^{miss}$ is defined as the negative vector sum of the ($\vec{p}_{\mathrm{T}}$) of all of the PF objects [44]. If the momentum of every PF particle was measured precisely, then $\vec{p}_{\mathrm{T}}^{miss}$ will be equal to the transverse momentum of only the neutrinos of BSM particles i.e. invisible particles which do not leave any hit

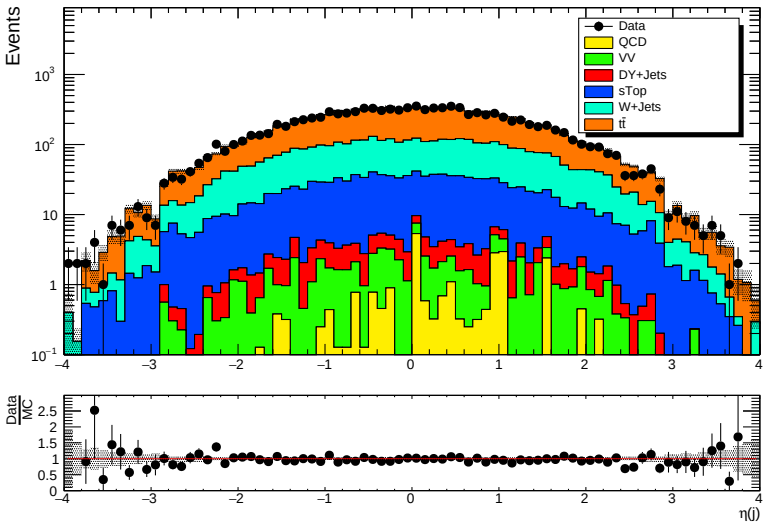

Figure 5.2: η distribution for jets in a $t\bar{t}$ control sample with one soft electron, 1 b-tagged jet, $E_T^{miss} > 250$ GeV, and $m_T(e, E_T^{miss}) < 110$ GeV.

in detector.

$$\vec{p}_{\mathrm{T}}^{\,miss} = -\sum_{Objects} \vec{p}_{\mathrm{T}}^{\,i} \tag{5.1}$$

E_T^{miss}, the magnitude of $\vec{p}_{\mathrm{T}}^{\,miss}$, is a commonly used variable..

5.4 Electron

Electrons are reconstructed using information from tracker and energy clusters in the ECAL. Electron tracks are reconstructed by matching trajectories in the silicon strip tracker to seed hits in the pixel detector by making use of Gaussian Sum Filter algorithm (GSF) [45]. The track that best matches an energy supercluster is chosen to be the reconstructed track.

While electrons are traveling through the silicon tracker material they lose energy due to Bremsstrahlung radiation. In order to estimate initial energy of the electrons, it is essential to calculate the photons' energy, which spread in ϕ over several ECAL crystals. Two algorithms, based on the clustering in the ECAL, are

used to estimate the energy of the electrons and photons. The "hybrid" algorithm is used in the barrel while the "multi-5x5" or "Island" algorithm is used in the endcap [46].

The electron energy is measured based on the information from both the ECAL and the tracker, since the two measurements complement each other. If the energy measurement from the ECAL matches the momentum measurement from the tracker, then the final energy is taken as average of the two. If the ECAL energy is greater than the tracker energy, then the ECAL measurement is used. However, if the tracker measurement is much greater than the ECAL measured value, then a decision is made based on the magnitude of the ECAL energy; less than 15 GeV and the tracker measurement is used, other wise the ECAL measurement is used.

Electron selections have two main components that are electron identification (eID) (see Table 5.2) and electron isolation. The "medium" identification working point of the cut based ID is used in this analysis.

Table 5.2: Electron ID selections.

Cut	Barrel	EndCap
H/E	< 0.253	< 0.0878
$\sigma_{i\eta i\eta}$	< 0.00998	< 0.0298
$\lvert\Delta\eta_{in}\rvert$	< 0.00311	< 0.00609
$\lvert\Delta\phi_{in}\rvert$	< 0.103	< 0.045
$1/E - 1/p$	< 0.134	< 0.13
Missing inner hits	< 2	< 2
Pass conversion veto	yes	yes
Rel Combined PF Iso (EA corr)	< 0.0695	< 0.0821

5.5 Muons

In this analysis we are using particle flow muons. Standalone muon reconstruction starts with the information gathered from all of the muon detectors. As a first step, the inner tracker produces a list of "tracker tracks" and the muon system generates a list of standalone muon tracks. In order to reconstruct the standalone muon, hits from innermost muon detectors are combined with the hits in outer muon detectors by using a Kalman fitting technique. Then, by extrapolating from the innermost muon station to the outer tracker surface, a standalone muon trajectory is reconstructed. This trajectory is then used to find a matching tracker track. After applying a global fit to matching tracker tracks and standalone muons, "global" muons are reconstructed. Table 5.3 shows complete list of a muon identification criteria, which are based on POG recommendations.

Table 5.3: μ Identification

Cut
recoMu.isGlobalMuon()
muon::isPFMuon()
recoMu.globalTrack()-> normalizedChi2()< 10
recoMu.globalTrack()-> hitPattern().numberOfValidMuonHits()> 0
recoMu.numberOfMatchedStations()> 1
fabs(recoMu.muonBestTrack()-> dxy(vertex-> position()))< 0.2
fabs(recoMu.muonBestTrack()-> dz(vertex-> position()))< 0.5
recoMu.innerTrack()-> hitPattern().numberOfValidPixelHits()> 0
recoMu.innerTrack()-> hitPattern().trackerLayersWithMeasurement()> 5

5.6 Hadronically Decaying Tau Lepton

The tau lepton is the heaviest lepton in the standard model. It has a mass of 1.777 GeV/c^2 and a lifetime of 0.29 picosecond. Taus are also the only leptons which decay hadronicaly $\approx$ 65% of the time and leptonically $\approx$ 35% of the time to the final products $e + \nu_e$ or $\mu + \nu_\mu$. These decays occur through the weak interaction.

It is challenging to reconstruct hadronically decaying taus because they are similar to QCD jets. The object is reconstructed using hadronic plus strip (HPS) [47] algorithm, which makes use of PFJets as input and is designed to optimize the performance of τ_h reconstruction by considering specific τ_h decay modes. Since hadronically decaying taus decay to charged pions and neutral pions, these neutral pions decay to well separated photon pair, resulting in two electromagnetic strips. Thus, "Single hadron" plus "two strips" refers to the reconstruction of the decay $\tau \rightarrow \nu_\tau \pi^\pm \pi^0$, while single hadron plus zero strips can refer to $\tau \rightarrow \nu_\tau \pi^\pm$. Tau decay modes are outlined in Table 5.4.

In order to reduce the fake rate from quark/gluons that can mimic hadronic taus, taus are required to be spatially isolated from other energy in the event. This is done by forming an isolation ring of radius ΔR. This isolation variable is calculated using a multivariate boosted decision tree (BDT) technique.

5.7 B-Tagged Jets

B quark jets (b-jets) arise from the hadronization of bottom quarks. B tagging algorithms make use of the long life time of bottom quarks, which leads to the production and identification or a secondary vertex. For a given jet, the impact parameter of the matched vertex is used to discriminate between b-jets and jets from light quarks or gluons. Some of the algorithms for identifying b-jets within

Table 5.4: Reconstructed tau decay modes

HPS Tau Decay Modes
Single Charged Hadron + Zero Strip
Single Charged Hadron + One Strip
Single Charged Hadron + Two Strips
Two Charged Hadrons
Three Hadrons

CMS are track counting algorithm, jet probability algorithm, simple secondary vertex and combined secondary vertex (CSV) etc [48]. The CSV algorithm has three benchmark points named loose, medium, and tight. The mistag probability for each working point is 10%, 1%, and 0.1% respectively. The corresponding b-tagging efficiencies are 80%, 65%, and 50%, respectively. B-tagging is very important in many physics analyses in order to obtain a clean signal region by removing the background processes with b-jets or obtain a background enriched control regions.

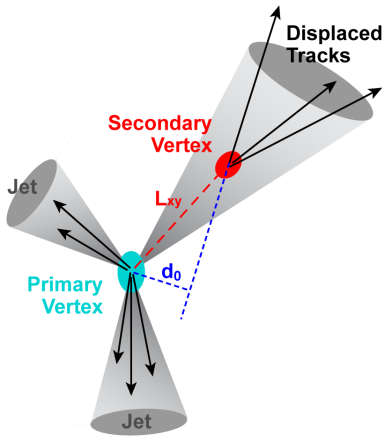

Figure 5.3: Illustration of a displaced secondary vertex with respect to a primary vertex in an event containing a bottom quark. Reprinted from [14]

5.8 Event Generation and Simulation

In high energy physics, physics processes are generated based on models such as SM, BSM theory in order to compare with the collision data. After generating the processes, the second step is simulating the way particles interact with the detector.

To generate events using event generators, parton distribution functions (PDF) are made use of in order to get the relevant information about the particles created from the incoming parton. This information will be used as input for the generator. PDF's are determined based on measurements of many different experiments such as CDF, ZEUS, D0, etc. LHC data are also used to reduce the uncertainty on the PDF's. The second step in generating the physics processes is calculating the matrix elements or probability of how often a process is happening. Many event generators, which will be detailed below are available for this purpose.

5.8.1 MadGraph 5

A matrix element generator MadGraph [49] is used for pp, $p\bar{p}$ collisions and contains next to leading order (NLO) perturbative calculations. It can be run with PYTHIA since it does not perform parton showering and hadronization process. Samples generated with MadGraph contains "madgraph" in their names.

5.8.2 Pythia

The Pyhtia is a leading order (LO) matrix element generator which also performs hadronization and fragmentation [50]. Pythia includes different tunes for underlying events (UE), PS and the hadronization. Samples labeled with "pythia"in their name are produced with the PYTHIA such as DY+Jets (see Ta-

ble 6.2 for list of samples generated with Pythia).

5.8.3 POWHEG

POWHEG is another matrix element generator that includes NLO perturbative calculations [51]. Samples produced with POWHEG include key "powheg" in their name.

5.8.4 Geant4

Geant4 (GEometry ANd Tracking) is a platform for detector simulation [52]. Interaction of the produced particles with material of all sub-detectors is simulated with Geant4 which includes detectors' geometry and their components. It is used by many different experiment such as ATLAS, CMS, MINOS and DUNE etc.

6. DATA AND MONTE CARLO SAMPLES

6.1 Data Samples

The 13 TeV data collected by the CMS detector during 2016 is used in this analysis. The primary data set (PD) used is the MET PD for the main search region although the Single Muon PD is used for trigger efficiency study in order to utilize clean muon control regions. Table 6.1 shows the collision datasets used. The official JSON file is used to select "good" run ranges and lumi sections (Cert_271036-284044_13TeV_03Feb2017ReReco_Collisions16_JSON.txt). The total integrated luminosity of the collision data samples is 35.87 fb^{-1} (see Figure 6.1)

Table 6.1: Collision data samples correspond to an integrated luminosity of 35.86 fb^{-1}

.

Physics Sample	Official CMS Datasets
Run 2016B SingleMu Run2016B-03Feb2017	*/SingleMuon/Run2016B-03Feb2017_ver2-v2/MINIAOD*
Run 2016C SingleMu Run2016C-03Feb2017	*/SingleMuon/Run2016C-03Feb2017-v1/MINIAOD*
Run 2016D SingleMu Run2016D-03Feb2017	*/SingleMuon/Run2016D-03Feb2017-v1/MINIAOD*
Run 2016E SingleMu Run2016E-03Feb2017	*/SingleMuon/Run2016E-03Feb2017-v1/MINIAOD*
Run 2016F SingleMu Run2016F-03Feb2017	*/SingleMuon/Run2016F-03Feb2017-v1/MINIAOD*
Run 2016G SingleMu Run2016G-03Feb2017	*/SingleMuon/Run2016G-03Feb2017-v1/MINIAOD*
Run 2016Hv2 SingleMu Run2016H-03Feb2017	*/SingleMuon/Run2016H-03Feb2017_ver2-v1/MINIAOD*
Run 2016Hv3 SingleMu Run2016H-03Feb2017	*/SingleMuon/Run2016H-03Feb2017_ver3-v1/MINIAOD*
Run 2016B Met Run2016B-03Feb2017	*/Met/Run2016B-03Feb2017-v3/MINIAOD*
Run 2016C Met Run2016C-03Feb2017	*/Met/Run2016C-03Feb2017-v1/MINIAOD*
Run 2016D Met Run2016D-03Feb2017	*/Met/Run2016D-03Feb2017-v1/MINIAOD*
Run 2016E Met Run2016E-03Feb2017	*/Met/Run2016E-03Feb2017-v1/MINIAOD*
Run 2016F Met Run2016F-03Feb2017	*/Met/Run2016F-03Feb2017-v1/MINIAOD*
Run 2016G Met Run2016G-03Feb2017	*/Met/Run2016G-03Feb2017-v1/MINIAOD*
Run 2016Hv2 Met Run2016H-03Feb2017	*/Met/Run2016H-03Feb2017_ver2-v1/MINIAOD*
Run 2016Hv3 Met Run2016H-03Feb2017	*/Met/Run2016H-03Feb2017_ver3-v1/MINIAOD*

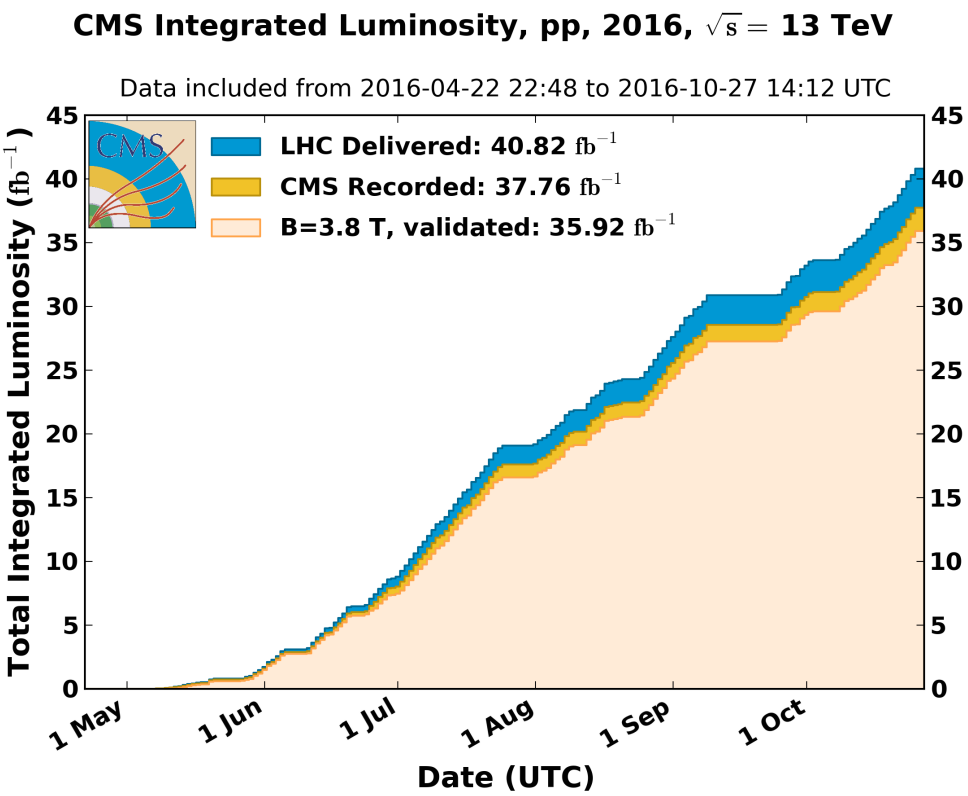

Figure 6.1: Integrated luminosity delivered by LHC and recorded by CMS. Reprinted from [15]

6.2 MC Samples

Official MC samples are used for all SM processes in this analysis and were generated using the LO generator PYTHIA8 and NLO generator POWHEG, MADGRAPH. Table 6.2 shows the entire list of MC samples. Since pile-up (PU) distributions in the MC samples differ from the ones in the data, we need to weight those in order to fit the PU distribution in the data by using event weight (See Eq 6.1) where $P_{data}(n)$ is the probability of getting n interaction in data while $P_{MC}(n)$ is the probablity of getting n interaction in MC.

$$w_{PU}(n) = \frac{P_{data}(n)}{P_{MC}(n)} \tag{6.1}$$

Table 6.2: MC samples

Process	cross-section (pb)	Official CMS Datasets (MINIAODSIM)
$Z \to ll$	5765.4	/DYJetsToLL_M-50_TuneCUETP8M1_13TeV-madgraphMLM-pythia8/RunIISummer16MiniAODv2-PUMoriond17_80X_mcRun2_asymptotic_2016_TrancheIV_v6_ext1-v2
mass binned	7.67*1.031	/DYJetsToLL_M-200to400_TuneCUETP8M1_13TeV-amcatnloFXFX-pythia8/RunIISummer16MiniAODv2-PUMoriond17_80X_mcRun2_asymptotic_2016_TrancheIV_v6_ext2-v2
LO samples	0.423*1.008	/DYJetsToLL_M-400to500_TuneCUETP8M1_13TeV-amcatnloFXFX-pythia8/RunIISummer16MiniAODv2-PUMoriond17_80X_mcRun2_asymptotic_2016_TrancheIV_v6_ext1-v1
	0.24*0.996	/DYJetsToLL_M-500to700_TuneCUETP8M1_13TeV-amcatnloFXFX-pythia8/RunIISummer16MiniAODv2-PUMoriond17_80X_mcRun2_asymptotic_2016_TrancheIV_v6_ext1-v1
	0.035*0.973	/DYJetsToLL_M-700to800_TuneCUETP8M1_13TeV-amcatnloFXFX-pythia8/RunIISummer16MiniAODv2-PUMoriond17_80X_mcRun2_asymptotic_2016_TrancheIV_v6_ext1-v1
	0.03*0.961	/DYJetsToLL_M-800to1000_TuneCUETP8M1_13TeV-amcatnloFXFX-pythia8/RunIISummer16MiniAODv2-PUMoriond17_80X_mcRun2_asymptotic_2016_TrancheIV_v6_ext1-v1
	0.016*0.938	/DYJetsToLL_M-1000to1500_TuneCUETP8M1_13TeV-amcatnloFXFX-pythia8/RunIISummer16MiniAODv2-PUMoriond17_80X_mcRun2_asymptotic_2016_TrancheIV_v6_ext1-v1
	0.002*0.882	/DYJetsToLL_M-1500to2000_TuneCUETP8M1_13TeV-amcatnloFXFX-pythia8/RunIISummer16MiniAODv2-PUMoriond17_80X_mcRun2_asymptotic_2016_TrancheIV_v6_ext1-v1
	0.00054*0.825	/DYJetsToLL_M-2000to3000_TuneCUETP8M1_13TeV-amcatnloFXFX-pythia8/RunIISummer16MiniAODv2-PUMoriond17_80X_mcRun2_asymptotic_2016_TrancheIV_v6_ext1-v1
$W + jets$	61526.7	/WJetsToLNu_TuneCUETP8M1_13TeV-madgraphMLM-pythia8/RunIISummer16MiniAODv2-PUMoriond17_80X_mcRun2_asymptotic_2016_TrancheIV_v6_ext2-v1
HT binned	1345*1.21	/WJetsToLNu_HT-100To200_TuneCUETP8M1_13TeV-madgraphMLM-pythia8/RunIISummer16MiniAODv2-PUMoriond17_80X_mcRun2_asymptotic_2016_TrancheIV_v6_ext2-v1
LO samples	359.7*1.21	/WJetsToLNu_HT-200To400_TuneCUETP8M1_13TeV-madgraphMLM-pythia8/RunIISummer16MiniAODv2-PUMoriond17_80X_mcRun2_asymptotic_2016_TrancheIV_v6_ext2-v1
	48.91*1.21	/WJetsToLNu_HT-400To600_TuneCUETP8M1_13TeV-madgraphMLM-pythia8/RunIISummer16MiniAODv2-PUMoriond17_80X_mcRun2_asymptotic_2016_TrancheIV_v6_ext1-v1
	12.05*1.21	/WJetsToLNu_HT-600To800_TuneCUETP8M1_13TeV-madgraphMLM-pythia8/RunIISummer16MiniAODv2-PUMoriond17_80X_mcRun2_asymptotic_2016_TrancheIV_v6_ext1-v1
	5.501*1.21	/WJetsToLNu_HT-800To1200_TuneCUETP8M1_13TeV-madgraphMLM-pythia8/RunIISummer16MiniAODv2-PUMoriond17_80X_mcRun2_asymptotic_2016_TrancheIV_v6_ext1-v1
	1.329*1.21	/WJetsToLNu_HT-1200To2500_TuneCUETP8M1_13TeV-madgraphMLM-pythia8/RunIISummer16MiniAODv2-PUMoriond17_80X_mcRun2_asymptotic_2016_TrancheIV_v6_ext1-v1
	0.03216*1.21	/WJetsToLNu_HT-2500ToInf_TuneCUETP8M1_13TeV-madgraphMLM-pythia8/RunIISummer16MiniAODv2-PUMoriond17_80X_mcRun2_asymptotic_2016_TrancheIV_v6_ext1-v1
$t\bar{t}$	831.76	/TT_TuneCUETP8M2T4_13TeV-powheg-pythia8/RunIISummer16MiniAODv2-PUMoriond17_80X_mcRun2_asymptotic_2016_TrancheIV_v6-v1
single Top samples	35.6	/ST_tW_antitop_5f_inclusiveDecays_13TeV-powheg-pythia8_TuneCUETP8M1/RunIISummer16MiniAODv2-PUMoriond17_80X_mcRun2_asymptotic_2016_TrancheIV_v6_ext1-v1
	35.6	/ST_tW_top_5f_inclusiveDecays_13TeV-powheg-pythia8_TuneCUETP8M1/RunIISummer16MiniAODv2-PUMoriond17_80X_mcRun2_asymptotic_2016_TrancheIV_v6_ext1-v1
	136.02	/ST_t-channel_top_4f_inclusiveDecays_13TeV-powhegV2-madspin-pythia8_TuneCUETP8M1/RunIISummer16MiniAODv2-PUMoriond17_80X_mcRun2_asymptotic_2016_TrancheIV_v6-v1
	26.23	/ST_t-channel_antitop_4f_inclusiveDecays_13TeV-powhegV2-madspin-pythia8_TuneCUETP8M1/RunIISummer16MiniAODv2-PUMoriond17_80X_mcRun2_asymptotic_2016_TrancheIV_v6-v1
	3.344	/ST_s-channel_4f_leptonDecays_13TeV-amcatnlo-pythia8_TuneCUETP8M1/RunIISummer16MiniAODv2-PUMoriond17_80X_mcRun2_asymptotic_2016_TrancheIV_v6-v1
$VV \to 2l2\nu$	11.95	/VVTo2L2Nu_13TeV_amcatnloFXFX_madspin_pythia8/RunIISummer16MiniAODv2-PUMoriond17_80X_mcRun2_asymptotic_2016_TrancheIV_v6_ext1-v1
$ZZ \to 2l2q$	3.22	/ZZTo2L2Q_13TeV_amcatnloFXFX_madspin_pythia8/RunIISummer16MiniAODv2-PUMoriond17_80X_mcRun2_asymptotic_2016_TrancheIV_v6-v1
$ZZ \to 4l$	1.256	/ZZTo4L_13TeV_powheg_pythia8/RunIISummer16MiniAODv2-PUMoriond17_80X_mcRun2_asymptotic_2016_TrancheIV_v6-v1
$WW \to lv2q$	1.212	/WWToLNuQQ_13TeV-powheg/RunIISummer16MiniAODv2-PUMoriond17_80X_mcRun2_asymptotic_2016_TrancheIV_v6_ext1-v1
$WZ \to 2l2q$	5.595	/WZTo2L2Q_13TeV_amcatnloFXFX_madspin_pythia8/RunIISummer16MiniAODv2-PUMoriond17_80X_mcRun2_asymptotic_2016_TrancheIV_v6-v1
$WZto3lv$	4.708	/WZJToLLLNu_TuneCUETP8M1_13TeV-amcnlo-pythia8/RunIISummer16MiniAODv2-PUMoriond17_80X_mcRun2_asymptotic_2016_TrancheIV_v6-v1
$WZ \to l3v$	3.05	/WZTo1L3Nu_13TeV_amcatnloFXFX_madspin_pythia8/RunIISummer16MiniAODv2-PUMoriond17_80X_mcRun2_asymptotic_2016_TrancheIV_v6-v1
$WZ \to lv2q$	10.71	/WZTo1L1Nu2Q_13TeV_amcatnloFXFX_madspin_pythia8/RunIISummer16MiniAODv2-PUMoriond17_80X_mcRun2_asymptotic_2016_TrancheIV_v6-v3

We also use officially produced signal samples in this study corresponding to different benchmark points. We assumed that $\tilde{\chi}_1^{\pm}$ and $\tilde{\chi}_2^0$ have the same mass

as both belong to the same gauge multiplet. Signal samples are listed in Table 6.3. For each of the corresponding $\tilde{\chi}_1^{\pm}$ - $\tilde{\chi}_2^0$ mass combinations, we have different mass splitting setting the $\tilde{\chi}_1^0$ mass. For example, $m_{\tilde{\chi}_1^{\pm}} = m_{\tilde{\chi}_2^0} - m_{\tilde{\chi}_1^0} =$ $1, 2, 5, 10, 15, 20, 25, 30, 35, 40, 45, 50$ GeV. Namely, ΔM is a mass difference between $\tilde{\chi}_1^{\pm}$ and LSP or mass difference between $\tilde{\chi}_2^0$ and LSP.

Table 6.3: List of officially produced signal samples. Mass of chargino-neutralino is given in the sample name's description. The "leptonic" in the naming means branching ratio to selectron or smuon is 50 %.

Sample Name	Located (LPC)
VBF-C1N2_leptonic_100_	*/eos/uscms/store/user/ra2tau/jan2017tuple/VBF-C1N2_leptonicDecays_TuneCUETP8M1_13TeV-madgraphMLM-pythia8/*
VBF-C1N2_leptonic_150_	*/eos/uscms/store/user/ra2tau/jan2017tuple/VBF-C1N2_leptonicDecays_TuneCUETP8M1_13TeV-madgraphMLM-pythia8/*
VBF-C1N2_leptonic_200_	*/eos/uscms/store/user/ra2tau/jan2017tuple/VBF-C1N2_leptonicDecays_TuneCUETP8M1_13TeV-madgraphMLM-pythia8/*
VBF-C1N2_leptonic_250_	*/eos/uscms/store/user/ra2tau/jan2017tuple/VBF-C1N2_leptonicDecays_TuneCUETP8M1_13TeV-madgraphMLM-pythia8/*
VBF-C1N2_leptonic_300_	*/eos/uscms/store/user/ra2tau/jan2017tuple/VBF-C1N2_leptonicDecays_TuneCUETP8M1_13TeV-madgraphMLM-pythia8/*
VBF-C1N2_leptonic_350_	*/eos/uscms/store/user/ra2tau/jan2017tuple/VBF-C1N2_leptonicDecays_TuneCUETP8M1_13TeV-madgraphMLM-pythia8/*
VBF-C1N2_leptonic_400_	*/eos/uscms/store/user/ra2tau/jan2017tuple/VBF-C1N2_leptonicDecays_TuneCUETP8M1_13TeV-madgraphMLM-pythia8/*
VBF-C1N2_leptonic_450_	*/eos/uscms/store/user/ra2tau/jan2017tuple/VBF-C1N2_leptonicDecays_TuneCUETP8M1_13TeV-madgraphMLM-pythia8/*
VBF-C1N2_leptonic_500_	*/eos/uscms/store/user/ra2tau/jan2017tuple/VBF-C1N2_leptonicDecays_TuneCUETP8M1_13TeV-madgraphMLM-pythia8/*

7. ANALYSIS

With 13 TeV data, we search for a SUSY signature in final states with a soft lepton plus two VBF jets and E_T^{miss} from the LSP. Our signals are chargino-neutralino, chargino-chargino production via VBF. In order to increase the sensitivity, our search will be based on three different channels: $e^{\pm}$, $\tau^{\pm}$ and $\mu^{\pm}$. Compared to the dilepton search at 8 TeV, the single lepton channel gives better efficiency to reconstruct one of the well identified leptons instead of both of them in the scenario where leptons are very soft.

7.1 Signal Region and Control Regions

As mentioned in the previous sections, VBF topology is characterized by the presence of two energetic jets in the forward direction, in opposite hemispheres, and with large dijet invariant mass. Events firing MET trigger **HLT_PFMETNoMu120_PFMHTNoMu120_IDTight** are selected for the final single electron + VBF analysis. These events need to satisfy offline selection criteria, such as a soft electron with $10 < p_{\mathrm{T}} < 40$ GeV in the central region of the detector having $|\eta| < 2.1$, in order to ensure that both tracks are reconstructed within the tracking system's acceptance, along with a large missing transverse energy E_T^{miss} > 250 GeV (dramatically reduces the $DY(\rightarrow ll)$+jets) from lightest supersymmetric particle (LSP). In this analysis well identified muons and hadronic taus are vetoed. We also require "0" b-jets identified by using the CSV medium working point in order to surpress top pair contamination. Only jets with $p_{\mathrm{T}} > 30$ GeV and seperated from leptons by $\Delta R > 0.3$ are searched for b-tagging. All those cuts above will be called central cuts.

Finally, we implement VBF cuts which require two jets that have $p_{\mathrm{T}} > 60$ GeV,

with a large pseudorapidity gap, $\eta_{j1} \times \eta_{j2} < 0$, and $m_{jj} > 1000$ GeV.

Figure 7.1 and 7.2 show VBF related distributions such as: m_{jj}, η^{Jet}, leading jet p_{T} and E_T^{miss}. Distribution in red corresponds to SM backgrounds while black lines represent a signal sample (VBF production of $\tilde{\chi}_1^{\pm}$-$\tilde{\chi}_2^0$ where $m_{\tilde{\chi}_1^{\pm}} = 300$ GeV and $m_{\tilde{\chi}_2^0} = 299$ GeV). As seen from the distributions, jets from SM production are more central with a small invariant mass while jets from VBF production are more forward like with a large dijet invariant mass.

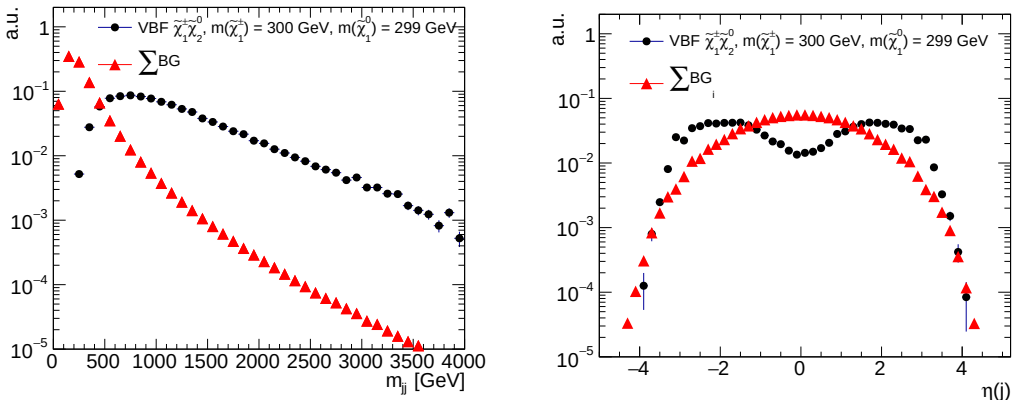

Figure 7.1: (a) m_{jj}, and (b) η^{jets}.

7.2 Optimization

Since the outgoing partons must carry large transverse momentum in order to produce both a SM vector boson and a pair of SUSY particles, we require high $p_{\mathrm{T}}^{Jets} > 60$ GeV with $|\eta| < 5.0$. All jets passing those requirements and having $\eta_{j1} \times \eta_{j2} < 0$, $|\Delta\eta| > 3.8$ and $m_{jj} > 1$ TeV form dijet candidates. All of those cuts above are called "VBF selections". In order to optimize the central selection cuts, we checked the significance by scanning for an upper threshold and lower

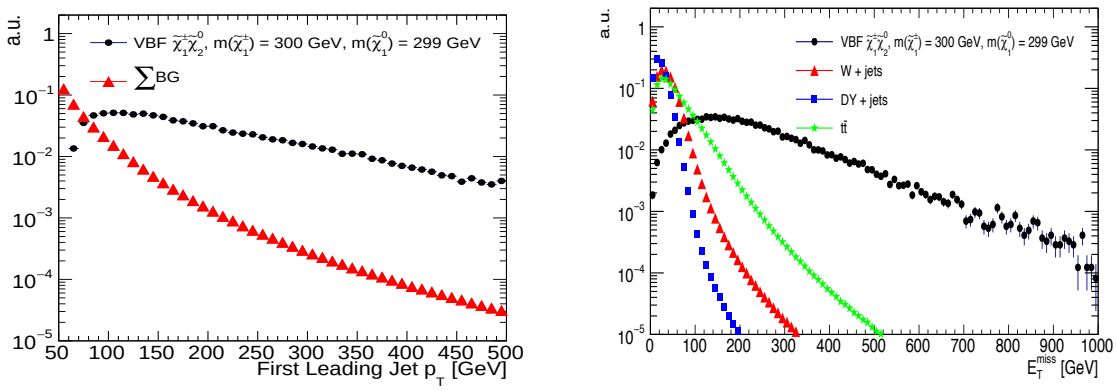

Figure 7.2: (a) leading jet p_{T}, and (b) E_T^{miss}.

threshold on variables one by one. Significance is given by Eq. 7.1 where S is Signal events while B corresponds to the background rate for the given variable that will be optimized. For electron p_{T}, we want to go as low as possible since soft leptons are crucial in compress mass spectra scenarios. Thus, electron p_{T} is set to be between 10 GeV and 40 GeV in order to reject SM background contribution in the signal region. The other variable we optimized is transverse mass (m_T). As seen in Figure 7.3 top plot, background MC events are mostly in the region where $m_T < 110$ and the significance plot at the bottom shows significance is highest around 110 GeV. Thus, we reject the events with a $m_T < 110$ GeV cut in order to reduce the background contribution in the signal region especially from W($\rightarrow e\nu$) + jets. Based on the trigger efficiency study (see Figure 4.2), we select $E_T^{miss} > 250$ GeV cut where the trigger turn-on curve reaches 100% efficiency. This cut is also the optimum one based on signal significance seen in Figure 7.4. Table 7.1 shows briefly the optimized cuts we are using for the analysis.

$$Sig = \frac{S}{\sqrt{S+B}} \tag{7.1}$$

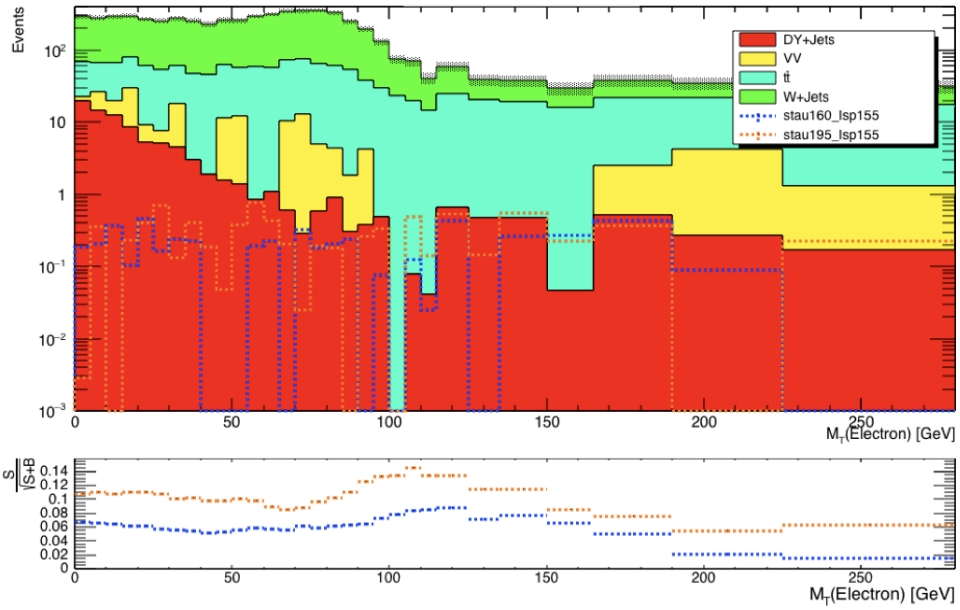

Figure 7.3: Transverse mass distribution

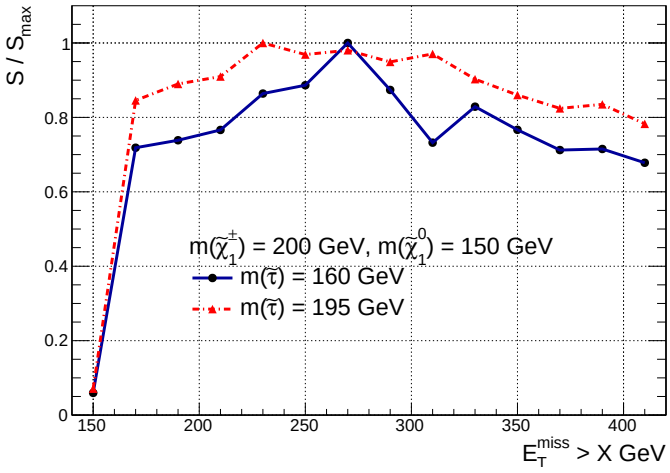

Figure 7.4: Signal significance S divided by the max significance S_{max}, as a function of E_T^{miss}.

Table 7.1: Event selection cuts after optimization

Event Selection	**Electron exclusive channel (Exactly one)**		
Dataset	Full 2016 data with 35.86 fb^{-1} (MET PD)		
Lepton flavour	Electron	Muon	Tau
Lepton Identification	Medium ID	Tight ID	Discrimination prong type 1 hps
Lepton Isolation	0.25	0.25	Tight Combined Isolation Delta Beta Corr 3 Hits
P_{T}^{lepton}	10.0 - 40.0	>8.0	>20.0
η^{lepton}	<2.1		
Specifics	Selected	Vetoed	Vetoed
Number of Jets	N(Jets)≥2		
VBF p_{T}^{Jet}	p_{T} >60 GeV, $\lvert\eta\rvert < 5.0$		
b-jet	$N(b-jets)$ =0, 1 or 2 with Medium W.P., p_{T}>30 GeV, $\lvert\eta\rvert < 2.4$ and No b-jet SF applied		
Overlap Removal	Yes		
E_T^{miss}	250 GeV		
VBF Cuts	At least one set of jets (j1,j2) with $\eta_{j1} \times \eta_{j2} < 0$, $\Delta\eta_{j1,j2} > 3.8$, $m_{jj} > 1$ TeV		

7.3 Background Estimation Using ABCD Method

7.3.1 ABCD Method

In order to estimate background rate in the signal region we use a data-driven background estimation using the ABCD method. In this method, we select four regions, one of which is the signal region (SR) while the others are background enriched regions called control region (CR), in a two dimensional plane where each of the axes is represented with a variable. In the case where the two variables are not correlated with each other, the relation $SR = \frac{CR(A) \times CR(C)}{CR(B)}$ holds.

7.3.2 $t\bar{t}$ Estimation

In this analysis, we have standard model backgrounds that mimic our signal. QCD production of $t\bar{t}$ is the dominant background and the predicted $t\bar{t}$ rate is

10.9 ± 4.1. The estimation of this background is carried out in a semi-data-driven method by selecting background enriched control regions. The first control region is selected such a way in order to extract Data to MC correction factor for the centrals selections, as defined in the beginning of this section. The other one is used to extract the Data to MC correction factor for the VBF selections. Figure 7.5 is an illustration to show how the control regions are defined for $t\bar{t}$ estimation.

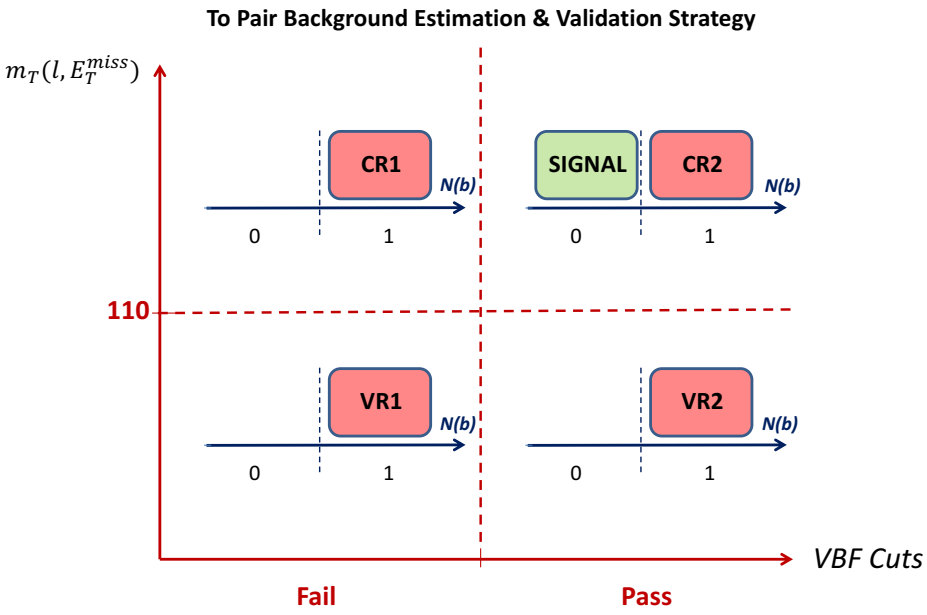

Figure 7.5: $t\bar{t}$ background estimation and validation strategy.

The first control region, called CR1, has a similar selection as the signal re-

gion, except with an inverted VBF requirement and a b-jet requirement. Inverted VBF means no dijet candidate satisfies all VBF selections. Also requiring 1 jet tagged as a b-jet increases the $t\bar{t}$ purity dramatically in this region. This control region has the same kinematics as the signal region (will be shown in section 7.4) thus correction factor obtained in here is not biased and can be used to correct the predicted $t\bar{t}$ from MC in the signal region. Table 7.2 shows observed and predicted event yields in CR1 along with the scale factor (SF^{CR1}) which is calculated as $(N^{\text{CR1}}(\text{Data}) - N^{\text{CR1}}(\text{other BGs}))/N^{\text{CR1}}(t\bar{t})$.

Table 7.2: Predicted and observed rates for the $t\bar{t}$ control regions with inverted VBF selections, CR1.

Sample	$t\bar{t}$ CR1
Diboson	2.2 ± 0.7
QCD	0.9 ± 0.5
Single Top	27.9 ± 2.0
W + jets	19.5 ± 1.9
DY + jets	1.0 ± 0.2
$t\bar{t}$	254.2 ± 8.7
Total MC	305.7 ± 9.2
Purity	83.2%
Data	349
Scale Factor	1.17 ± 0.09

The second control region (CR2) is also selected with a similar selection as the signal region except for requiring 1 jet identified as a b-jet. VBF efficiencies for both MC and data are calculated in this region. Table 7.3 shows event yields from MC and Data in CR2 along with the purity and Data to MC SF calculated as $(N^{\text{CR2}}(\text{Data}) - N^{\text{CR2}}(\text{other BGs}))/N^{\text{CR2}}(t\bar{t})$.

The scale factor for the VBF efficiencies (SF_{VBF}^{CR2}) is used to estimate $t\bar{t}$ con-

tribution in the signal region (See equation 7.2). VBF efficiency from data $\epsilon^{\text{Data}}_{t\bar{t},e}(\text{VBF cuts}) = 5.41e\text{-}2 \pm 1.24e\text{-}2$ and the VBF efficiency in $t\bar{t}$ MC is measured as $\epsilon^{\text{MC}}_{t\bar{t},e}(\text{VBF cuts}) = 6.61e\text{-}2 \pm 0.87e\text{-}2$. Thus, Data to MC scale factor for VBF efficiencies from CR2 is $SF^{\text{CR2}}_{VBF} = 0.82 \pm 0.26$. By using Equation 7.2, where $N^{t\bar{t}}_{SR}(\text{VBF cuts})$ is the number of $t\bar{t}$ events from MC in the signal region, the number of $t\bar{t}$ events in the signal region from data is estimated as 10.9 ± 4.1. Some of the kinematic distributions from CR1 and CR2 are seen in Figure 7.6 and Figure 7.7. Plots are produced after applying the data to MC scale factors in each CR. As seen, there is a perfect agreement between data and MC within the statistical uncertainty.

Table 7.3: Predicted and observed rates in CR2 after requiring 1 b-jet in addition to central and VBF selections.

Sample	$t\bar{t}$ CR2
Diboson	—
QCD	0.5 ± 0.4
Single Top	1.9 ± 0.5
W + jets	0.5 ± 0.1
DY + jets	—
$t\bar{t}$	19.7 ± 2.6
Total MC	22.6 ± 2.7
Purity	87.2%
Data	19
Scale Factor	0.82 ± 0.26

$$N^{\text{Data}}_{t\bar{t}} = N^{t\bar{t}}_{SR}(\text{VBF cuts}) \cdot SF^{\text{CR1}} \cdot SF^{\text{CR2}}_{VBF}, \tag{7.2}$$

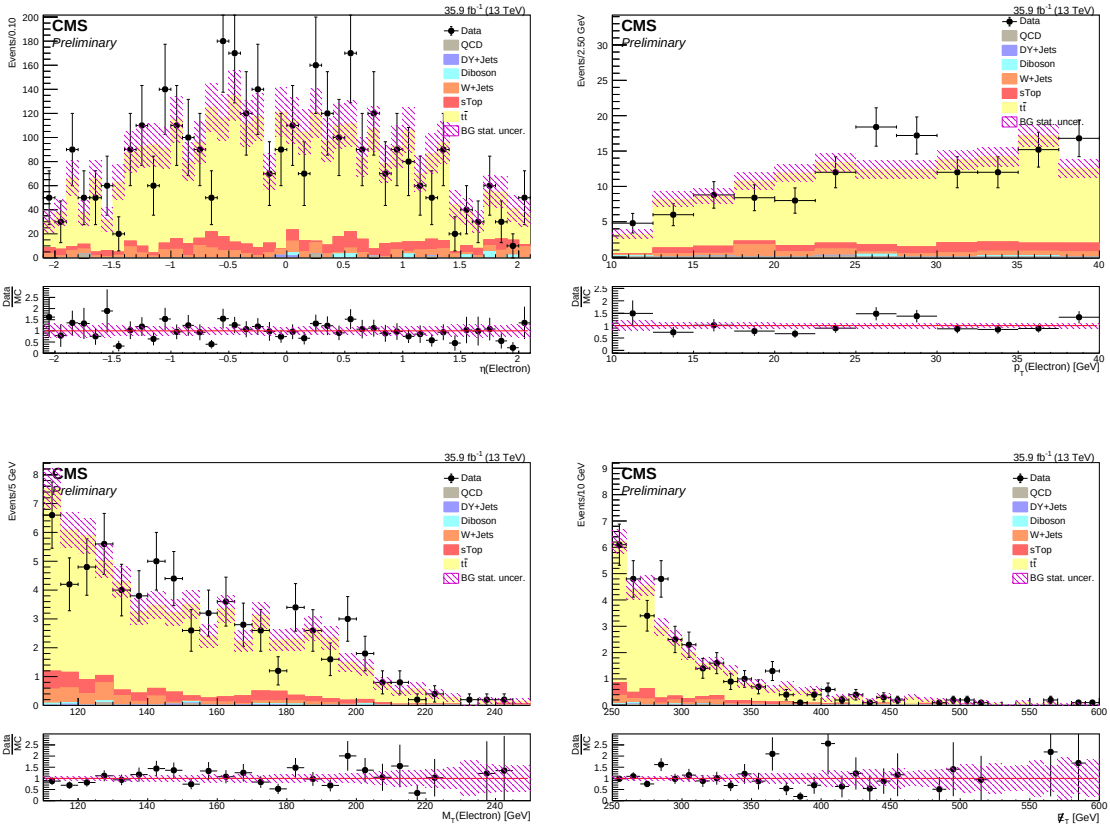

Figure 7.6: (Top from left to right) electron η and p_{T} distributions. Electron m_T and MET distributions (bottom left and right respectively) in $t\bar{t}$ enriched control region (CR1) after applying SF.

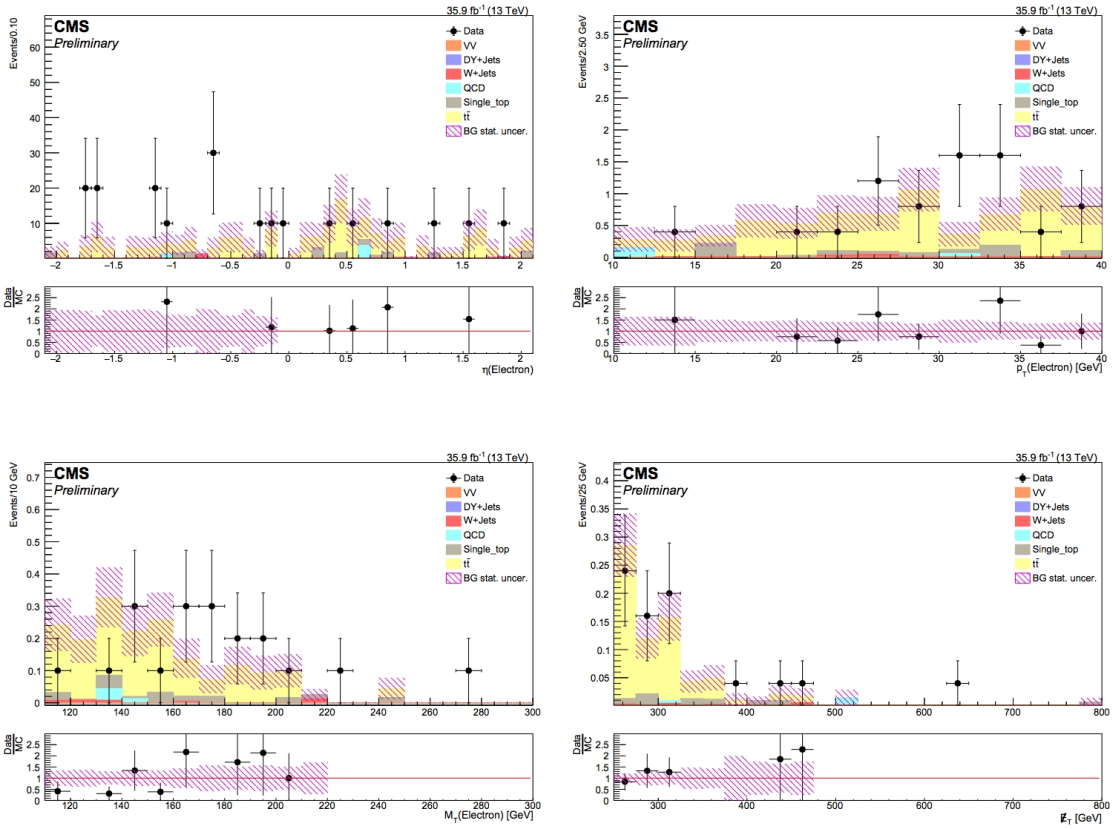

Figure 7.7: (Top from left to right) electron η and p_{T} distributions. Electron m_T and MET distributions (bottom left and right respectively) in $t\bar{t}$ enriched control region (CR2) after applying SF.

7.3.3 $W(\rightarrow e\nu)+$ jets Estimation

The second biggest contribution in the signal region is coming from the $W(\rightarrow e\nu)+$ jets process whose predicted rate (N^{Data}_{W+jets}) is 6.05 ± 1.38. $W(\rightarrow e\nu)+$ jets becomes a background when the W decays leptonically. The general methodology used in order to estimate the $W(\rightarrow e\nu)+$ jets background in the signal region is similar for all final states and is based on both simulation and data. As in $t\bar{t}$ estimation, we define control regions enriched with $W(\rightarrow e\nu)+$ jets sample. As side bands, we have chosen transverse mass (m_T) and dijet mass (m_{jj}) since these two variables are verified to be weakly correlated. Two control regions are obtained in order to estimate overall contribution of $W(\rightarrow e\nu)+$jets in the signal region. The first region, called CR1, is used to extract the Data to MC SF to correct for the mis-modeling of the central selections while CR2 is used to measure VBF efficiency. Figure 7.8 shows the CR selection criteria for $W(\rightarrow e\nu)+$ jets estimation.

The first control region is selected with the same selections as the signal region but requiring inverted VBF cuts. Inverting VBF cuts reduces the signal contamination to manageable level while increase the event yield from $W+$ jets significantly in this control region (CR1). With these selections, $\approx$ 65% purity of $W+$jets is obtained. Figures 7.9 and 7.10 show η^e, p^e_T, $m_T(e, E^{\text{miss}}_T)$ and E^{miss}_T distributions after the Data to MC SF is applied. As can be seen from the distributions, the shapes are consistent between data and MC within the uncertainty.

Table 7.4 shows event yields from CR1 for both data and MC as well as the scale factor calculated as $(N^{\text{CR1}}(\text{Data}) - N^{\text{CR1}}(\text{other BGs}))/N^{\text{CR1}}(\text{W + jets})$.
$\text{SF}^{CR1} = 0.97 \pm 0.10$. The uncertainty on the scale factor is statistical.

In order to calculate VBF efficiency, we obtained a DY+jets enriched control

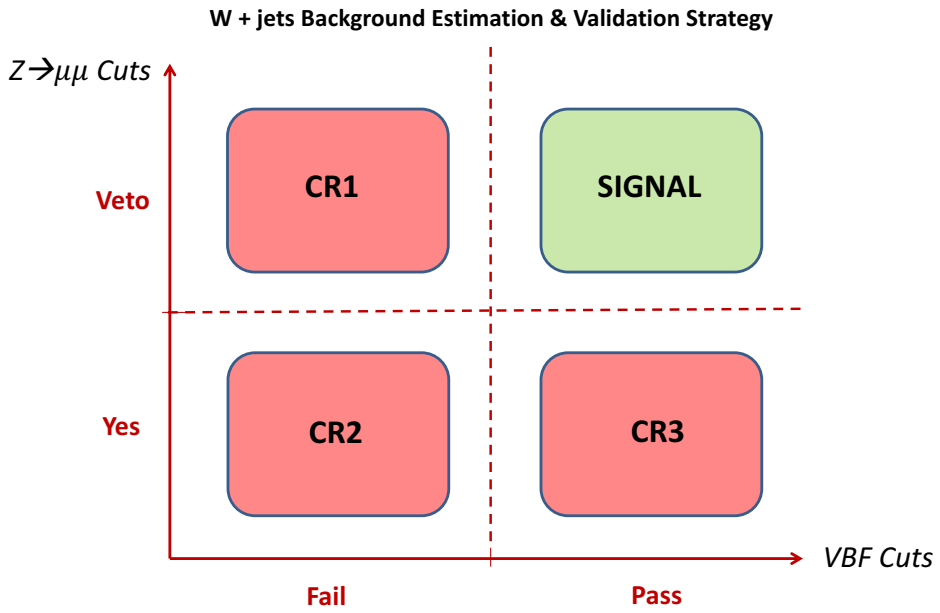

Figure 7.8: W + jets estimation strategy.

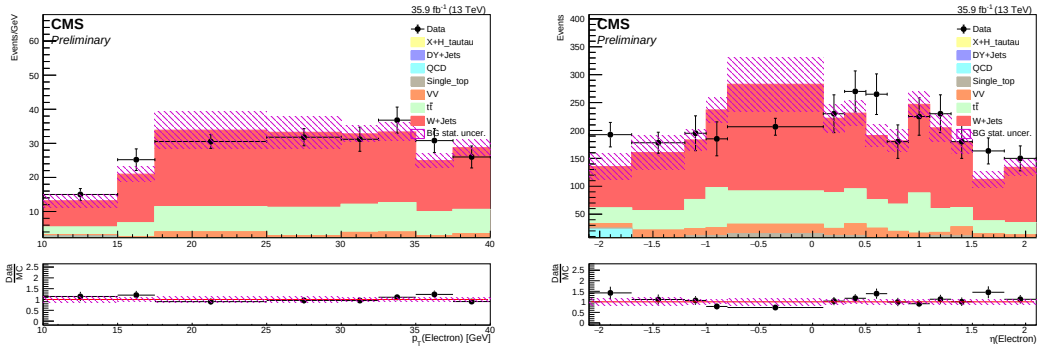

Figure 7.9: (a) p_T^e and (b) η^e distributions for W + jets CR1.

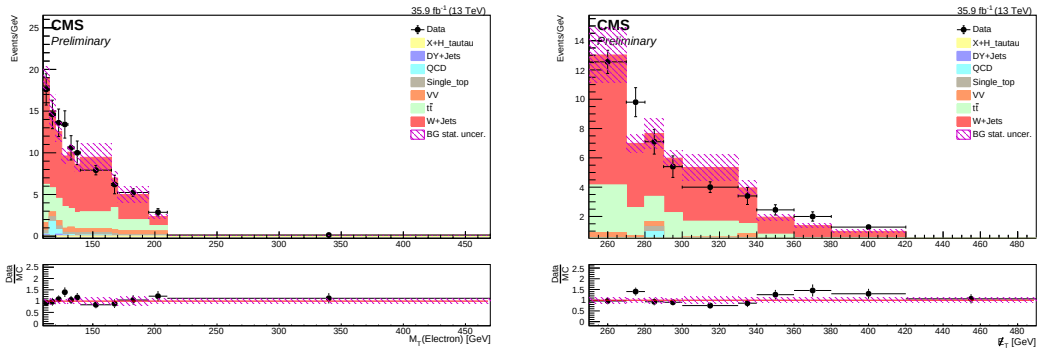

Figure 7.10: (a) $m_T(e, E_T^{miss})$ and (b) $E_{\mathrm{T}}^{\mathrm{miss}}$ distributions for W + jets CR1.

region which requires two isolated opposite charged muons with $p_T > 30$ GeV along with a dimuon invariant mass window of $60 < m(\mu, \mu) < 120$ GeV. Since muon channels are the cleanest one and muons are well understood, VBF efficiency from the $Z(\rightarrow \mu\mu)$+ jets are used in order to study the VBF efficiency in $W(\rightarrow e\nu)+$ jets. On top of passing the selections above, events firing the high level single muon trigger "*HLT_Iso_Mu*_24" comprises CR3 (see Diagram $Z(\rightarrow \mu\mu)$. With these selections (detailed event selection criteria for $Z(\rightarrow \mu\mu)$ are shown in Table 7.6), greater than 99% purity is obtained and perfect agreement between data and MC proves $\epsilon(\mu\mu)$ is well modeled. Having proved good modeling for $\epsilon(\mu\mu)$, VBF cut efficiency can be studied in the CR2. Some distributions from CR3 showing perfect agreement between data and MC can be seen in Figure 7.11. Event yields from CR3 are listed in Table 7.5.

Table 7.4: Predicted and observed rates along with data to MC scale factor for the W + jets control regions with inverted VBF selections. SF^{CR1} is calculated as $(N^{\text{CR1}}(\text{Data}) - N^{\text{CR1}}(\text{other BGs}))/N^{\text{CR1}}(\text{W + jets})$.

Sample	W + jets CR1
Diboson	56.0 ± 4.3
QCD	13.8 ± 7.3
Single Top	26.3 ± 2.2
W + jets	554.4 ± 46.6
DY + jets	6.6 ± 1.1
$t\bar{t}$	195.9 ± 8.7
Total MC	853.0 ± 48.2
Purity	65%
Data	838
Scale Factor	0.97 ± 0.10

Table 7.5: Event yields in $Z \to \mu\mu$ enriched region and VBF region called CR2 and CR3 respectively.

Process	CR2	CR3
Data	15080657	4174
$DY + Jets$	15795222.6 ± 7659.0	3100.7 ± 42.6
QCD	62412.8 ± 23860.0	373.3 ± 250.5
VV	18533.7 ± 78.1	25.0 ± 2.8
$W + Jets$	1372.1 ± 100.9	3.0 ± 0.9
sTop	5625.1 ± 32.9	20.3 ± 1.9
$t\bar{t}$	34336.6 ± 115.6	252.5 ± 9.9
Scale Factor	0.947 ± 0.001	1.128 ± 0.084

CR3 is selected with the VBF cuts in addition to CR2 cuts. The data driven

VBF efficiency is $Eff_{VBF}^{Data} = 2.33e\text{-}4 \pm 0.17e\text{-}4$ whereas the VBF efficiency from MC is $Eff_{VBF}^{MC} = 1.96e\text{-}4 \pm 0.03e\text{-}4$. Thus, scale factor for the VBF efficiency is $\text{SF}_{VBF} = \frac{Eff_{VBF}^{Data}}{Eff_{VBF}^{MC}} = 1.19 \pm 0.03e\text{-}4$. The number of W + jets events in the signal region is calculated by using the equation 7.3, where $\sigma_{\text{W + jets}}$ is the cross section of the W + jets process, L_{int} is the total integrated luminosity, $\epsilon_{\text{W + jets}}^{\text{MC}}(\text{central cuts})$ is the central selection efficiency for MC W + jets events, SF^{CR1} is the correction factor for the central selections obtained from the inverted VBF control samples (with other similar SR cuts), $\epsilon_{\text{W + jets}}^{\text{MC}}(\text{VBF cuts})$ is the efficiency for the VBF selections in MC W + jets events, and SF^{CR2} is the correction factor for the VBF efficiency obtained from CR3 ($Z(\rightarrow \mu\mu)$ + jets control sample). This procedure yields an estimate of $N_{\text{W + jets},e}^{\text{Data}} = 6.05 \pm 1.38$. Some kinematic distributions from "CR3" are shown in Figure 7.12.

$$N_{\text{W + jets}}^{\text{Data}} = \sigma_{\text{W + jets}} \cdot L_{int} \cdot \epsilon_{\text{W + jets}}^{\text{MC}}(\text{central cuts}) \cdot \epsilon_{\text{W + jets}}^{\text{MC}}(\text{VBF cuts}) \cdot SF^{\text{CR1}} \cdot SF^{\text{CR2}}, \tag{7.3}$$

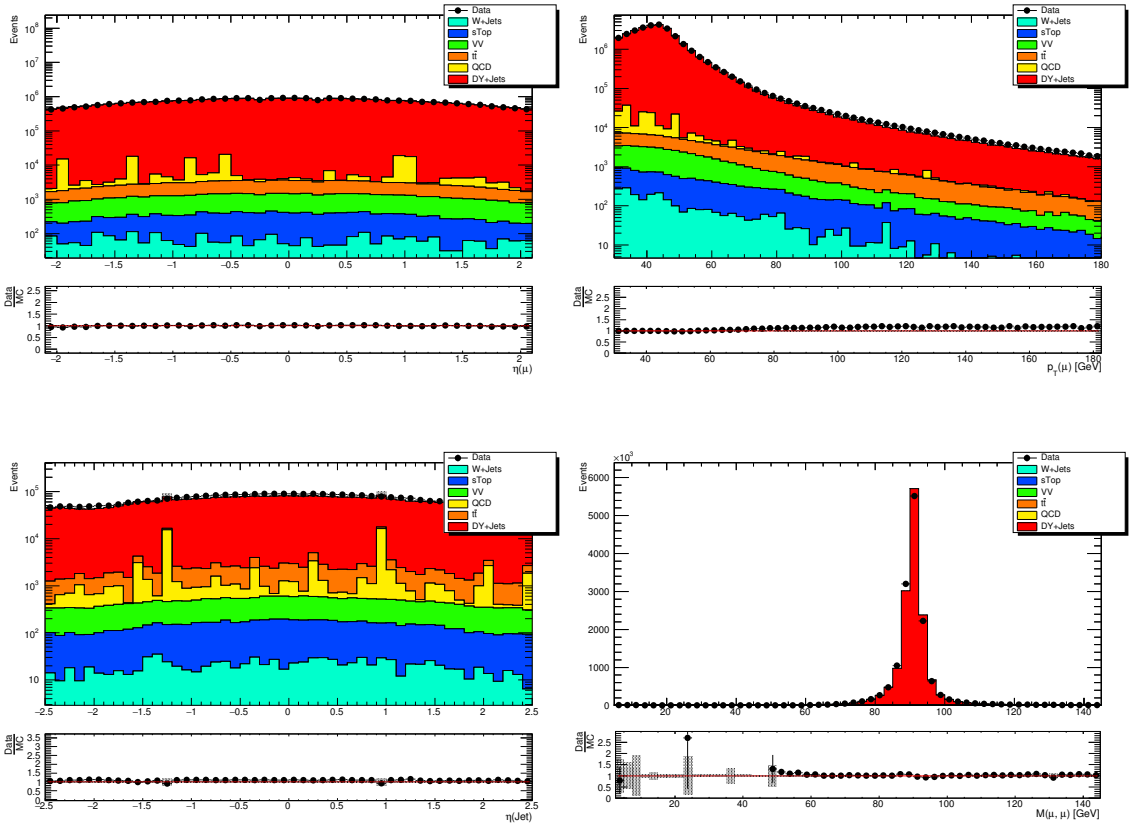

Figure 7.11: (Top from left to right) muon η and p_{T} distributions. Central jet η with di-muon invariant mass distributions (bottom left and right respectively) in DY+jets dominated CR (CR2) after applying SF.

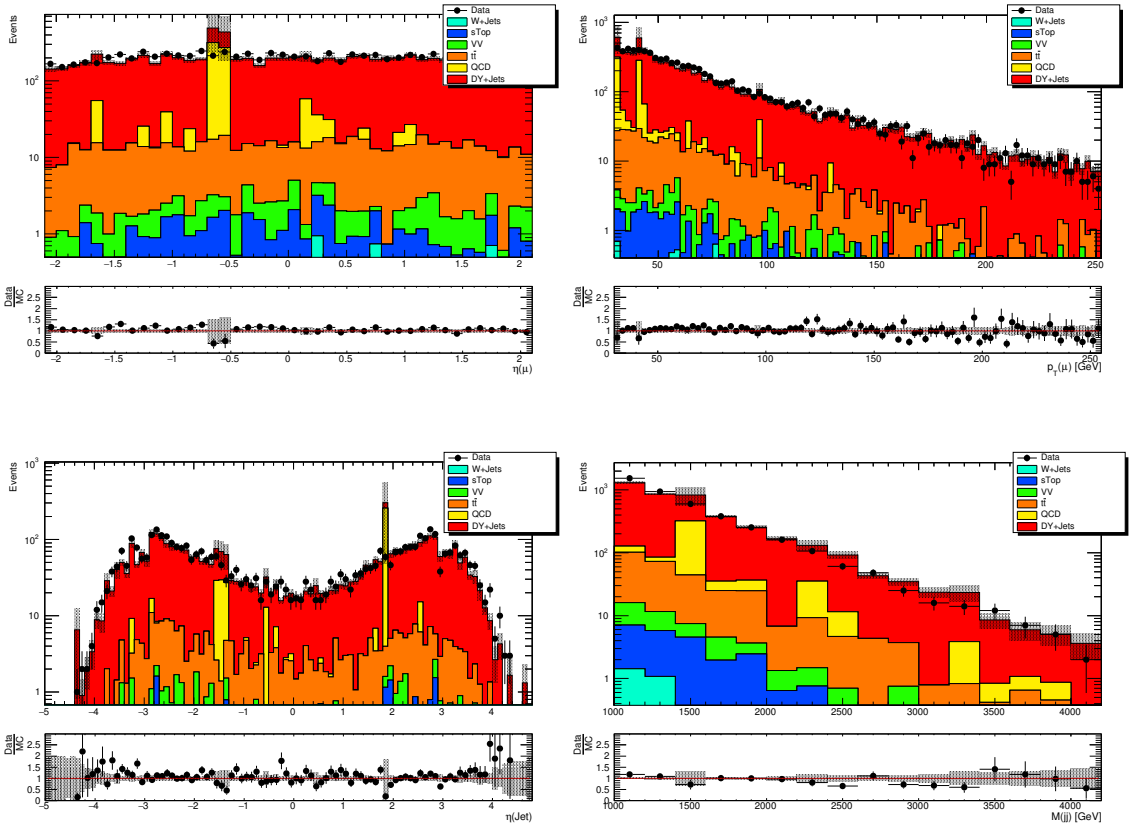

Figure 7.12: (Top from left to right) muon η and p_{T} distributions. Central jet η with di-muon invariant mass distributions (bottom left and right respectively) in CR3 after applying SF.

Table 7.6: Event selections criteria for DY+jets CR2. On top of those following cuts, VBF cuts are also applied for another region called "CR3" in order to measure VBF efficiency as a ratio of two regions.

Event Selection	**$Z \to \mu\mu$ CR**		
Dataset	Full 2016 data with 35.86 fb^{-1} (Single Muon PD)		
Lepton flavour	Electron	Muon	Tau
Lepton Identification	Medium ID	Tight ID	Discrimination prong type 1 hps
Lepton Isolation	0.25	0.25	Tight Combined Isolation Delta Beta Corr 3 Hits
P_{T}^{lepton}	10.0 - 40.0	>30.0	>20.0
η^{lepton}	<2.1		
Specifics	Vetoed	2 μ Selected	Vetoed
Number of Jets	N(Jets)≥2		
VBF p_{T}^{Jet}	p_{T} >60 GeV, $\lvert\eta\rvert < 5.0$		
b-jet	$N(b-jets)$ =0 with Medium W.P., p_{T}>30 GeV, $\lvert\eta\rvert < 2.4$ and No b-jet SF applied		
Overlap Removal	Yes		
E_T^{miss}	No Cuts		
VBF Cuts	At least one set of jets (j1,j2) with $\eta_{j1} \times \eta_{j2} < 0$, $\Delta\eta_{j1,j2} > 3.8$, $m_{jj} > 1$ TeV		

7.3.4 Other Backgrounds

Contribution from the other SM backgrounds in the signal region is negligible compared to $t\bar{t}$ and W($\to e\nu$) + jets due to the $E_T^{miss} > 250$ GeV, $p_{\mathrm{T}}^{jet} > 60$ GeV and other VBF cut requirements. Thus, background estimations will be taken directly from MC simulation.

7.4 $t\bar{t}$ Closure Test

In order to show our ttbar one b-jet selection (instead of b-jet veto) does not bias the composition of events, we carried out some closure test by requiring 1-b jet and 0-b jet separately on top of the signal region selections and proved our selections does not bias the lepton kinematics. Figure 7.13 through Fig-

ure 7.14 shows electron η and p_{T}, m_T and m_{jj} distributions after requiring both with matching and without matching to generated particles. Distributions are normalized to unity, and as seen from the ratio plots, agreement is within the statistical uncertainty thus it can be concluded that VBF selection efficiency is not biased by the requirement of 1 b-jet. Table 7.7 lists the composition of events in $t\bar{t}$ MC events for the signal region (0 b-tagged jets) and control region (1 b-tagged jet). The composition of events is in agreement in both region within the statistical uncertainty.

Table 7.7: Composition of $t\bar{t}$ events in both signal and control regions.

Composition	0 b-jets (signal region)	1 b-jets (control region)
1 e + 0 "fakes"	0.72 ± 0.14	0.83 ± 0.12

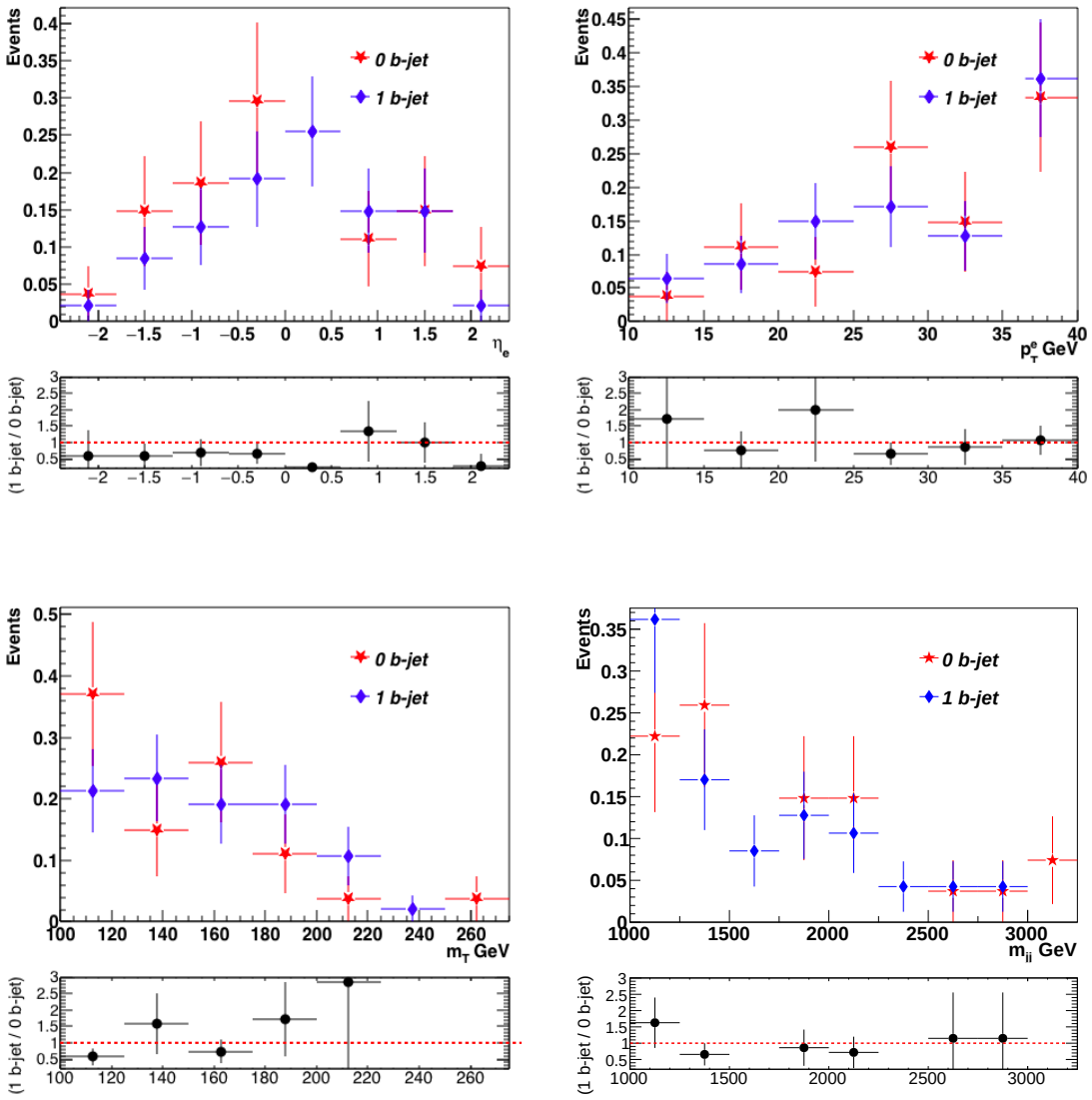

Figure 7.13: Comparision of events with 1 b-jet and 0-b jet after lepton matching and normalized to unity. Top from left to right, electron η and p_{T} distributions. Bottom left to right, m_T and m_{jj} distributions.

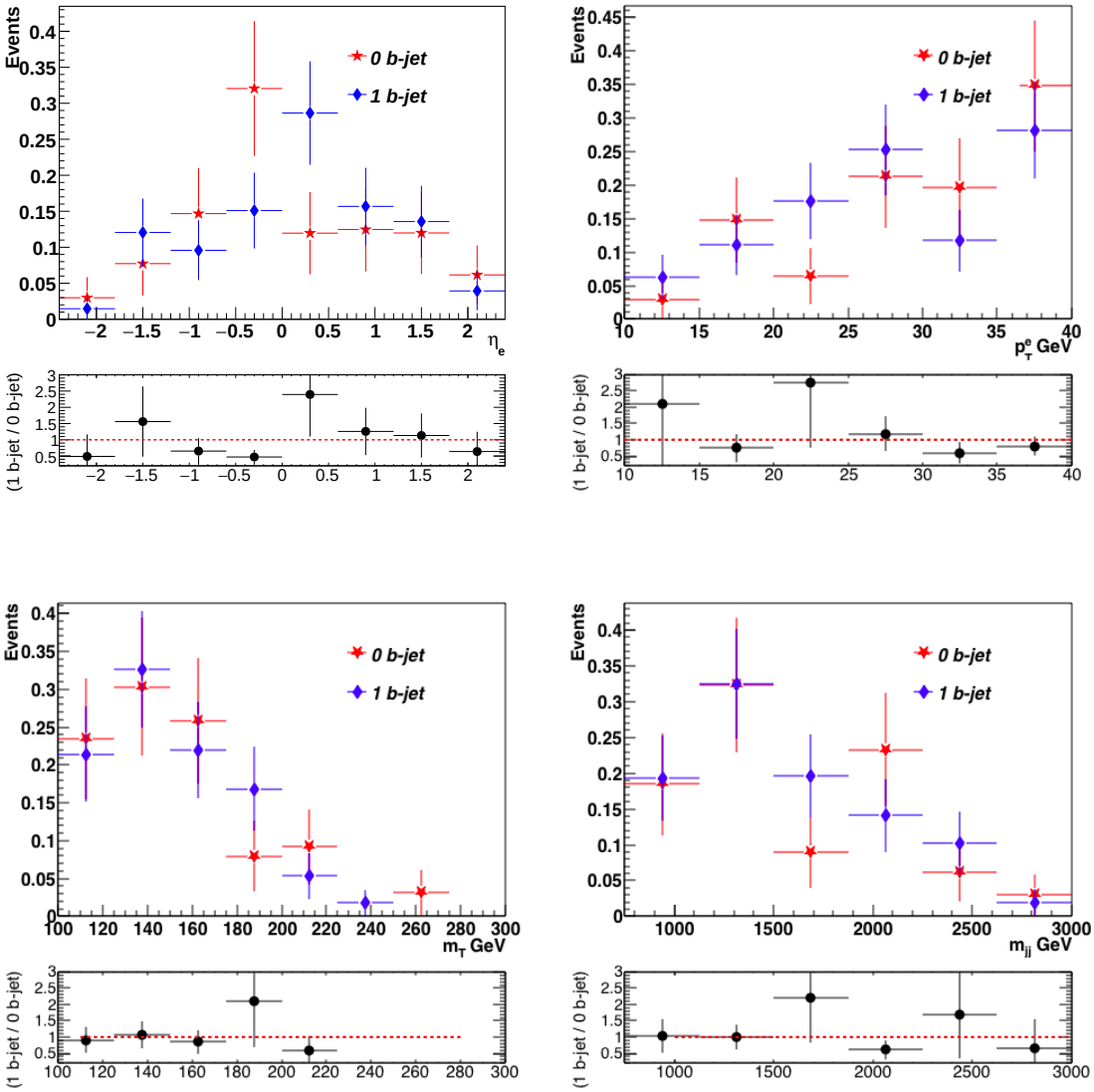

Figure 7.14: Comparision of events with 1 b-jet and 0-b jet after no lepton matching. Distributions are normalized to unity. Top from left to right, electron η and p_{T} distributions. Bottom left and right, m_T and m_jj distributions respectively.

7.5 Validation of the $t\bar{t}$ Scale Factors and VBF Shapes with Low-m_T Region

Since data to MC scale factors are calculated from a control region with low statistics by requiring 1-b jet + VBF cuts selections, it is worthwhile to validate the

results by choosing validation regions (VR) that are completely orthogonal and have higher statistics with highly $t\bar{t}$ purity. The first one of the two validation regions, referred as VR1, is formed with the same selection as $t\bar{t}$ CR1 but requires $m_T(e, E_T^{miss}) < 110$ GeV and is used to validate measured SF for centrals selections. Similarly, in order to validate the scale factor for VBF efficiency, the second validation control region (VR2) is comprised of events with $m_T(e, E_T^{miss}) < 110$ and VBF selections. Validation regions are depicted in Figure 7.5.

Figures 7.15 show the η and p_{T} distributions from VR1 after applying SF^{CR1}. As seen from the distributions, both shape and event rate are consistent for MC and data. Thus, SF^{CR1} can be used to correct the $t\bar{t}$ event yield in the signal region. In a similar way, VR2 can be used to validate the VBF efficiency scale factors, as agreement between the data and MC is seen from the Figures 7.16. Table 7.8 and Table 7.9 shows event yields for both MC and data from VR1 and VR2 respectively.

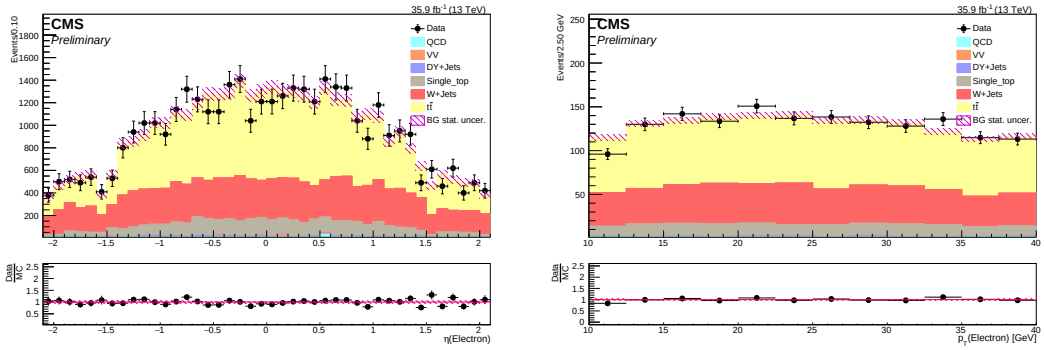

Figure 7.15: (a) $\eta(e)$ and (b) $p_{\mathrm{T}}(e)$ distributions in VR1.

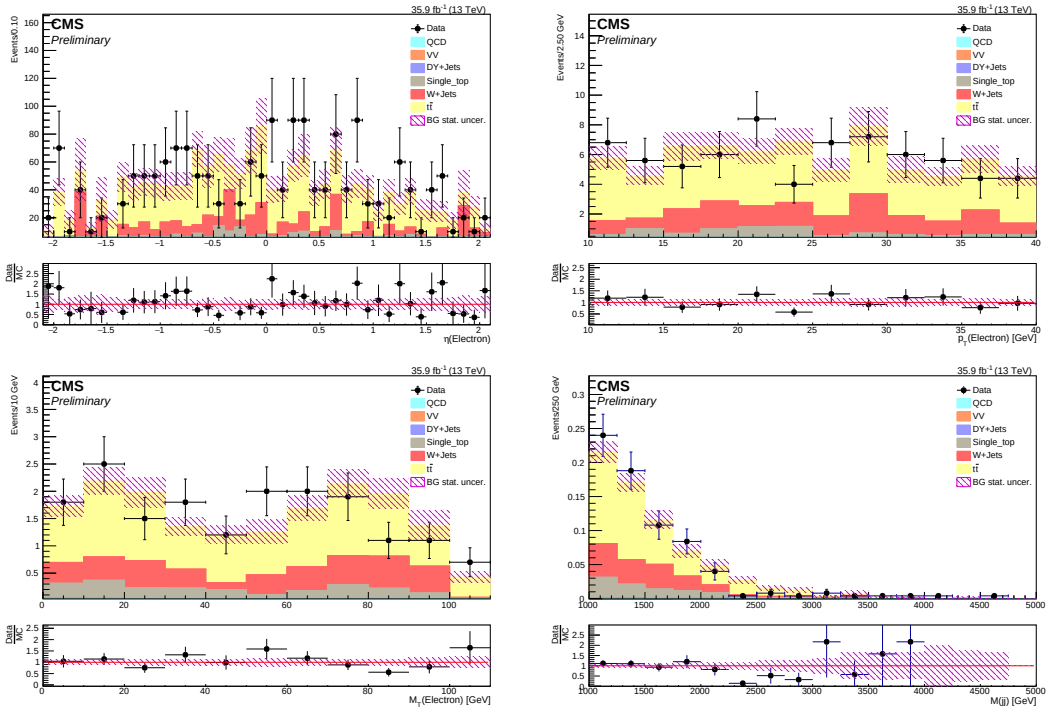

Figure 7.16: (a) $\eta(e)$, (b) $p_{\mathrm{T}}(e)$, (c) E_T^{miss}, and (d) m_{jj} distributions for the $t\bar{t}$ in VR2.

7.6 Validation of the $t\bar{t}$ VBF Shapes with Dilepton Samples

The level of agreement between data and MC has been studied in $t\bar{t}$ enriched $\mu\mu$ and $e\mu$ samples in order to have more confidence for $t\bar{t}$ shape in the signal region. This can be taken from the MC directly. The purity of $t\bar{t}$ is very high in those control regions since control regions are generated by requiring one b-tagged jet and $p_{\mathrm{T}}^{\mu} > 30$ GeV, which surpress signal contamination dramatically in the compress mass spectra scenario where lepton(s) is/are soft. Figures 7.17(a)-(b) show the m_{jj} distributions for the $t\bar{t}$ $\mu\mu$ and $e\mu$ samples respectively. As seen, m_{jj} distribution in data and MC is in perfect agreement. Thus, shapes for $t\bar{t}$ in signal region can be taken directly from MC.

Table 7.8: Predicted and observed rates for validation region VR1, used to validate the scale factor measured from $t\bar{t}$ control sample CR1.

Sample	$t\bar{t}$ VR1
Diboson	27.3 ± 2.7
QCD	5.5 ± 2.5
Single Top	401.8 ± 6.9
W + jets	1255.5 ± 18
DY + jets	28.5 ± 1.3
$t\bar{t}$	2669.0 ± 28.2
Total MC	4387.6 ± 29.03
Purity	60.8%
Data	3880.0

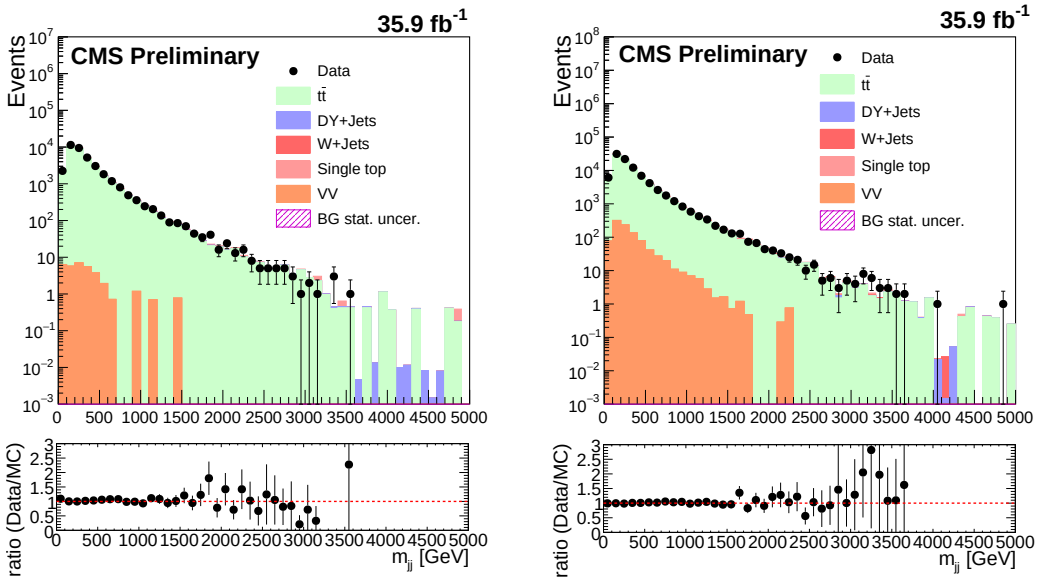

Figure 7.17: m_{jj} distributions for the $t\bar{t}$ $\mu\mu$ and $e\mu$ shape validation regions.

Table 7.9: Predicted and observed rates for validation region VR2 which are used to validate the VBF efficiency scale factors measured from $t\bar{t}$ control sample CR2.

Sample	$t\bar{t}$ VR2
Diboson	0.2 ± 0.2
QCD	1.3 ± 1.3
Single Top	22.3 ± 1.5
W + jets	42.3 ± 4.8
DY + jets	0.8 ± 0.1
$t\bar{t}$	115.4 ± 5.7
Total MC	$182.3 \pm 6.1_{\text{MC } stat} \pm 13.5_{poisson}$
Purity	63.3%
Data	176

7.7 Validation of the W + jets Scale Factors and VBF Shapes with Low-m_T Region

Although the efficiency for the central selection is well modeled by MC, it is worthwhile to validate this scale factor and VBF efficiency (measured from $Z(\rightarrow \mu\mu)$ + jets control region) by selecting validation regions (VR), orthogonal to signal region. Events passing central selections with $m_T(e, E_T^{miss}) < 110$ GeV and inverted VBF requirements comprises VR1, which has higher statistics and pure W + jets events (greater than 85% according to MC). In order to validate the scale factor measured from CR1, distributions in the VR1 are scaled with the SF^{CR1}. It is demonstrated that there is a good agreement between data and MC after applying SF^{CR1} as seen in Figure 7.18. As a result of this consistency between data and MC after applying the SF^{CR1}, SF^{CR1} can be used to correct W +jets events in the signal region. Event yields in the VR1 is shown in Table 7.10.

The second validation region (VR2) is filled with events satisfying the central selection and VBF cuts in low mT region (<110 GeV). The validation strategy for

central selection SF and VBF efficiency is depicted in Figure 7.19. As seen from the distributions in Figure 7.20, corrected with SF^{CR3}, there is a good agreement between the data and MC shapes as well as event rates within the statistical uncertainty, which validates the VBF efficiency measured from the $Z(\rightarrow \mu\mu)$ + jets control sample. Event yield for VR2 is listed in Table 7.11.

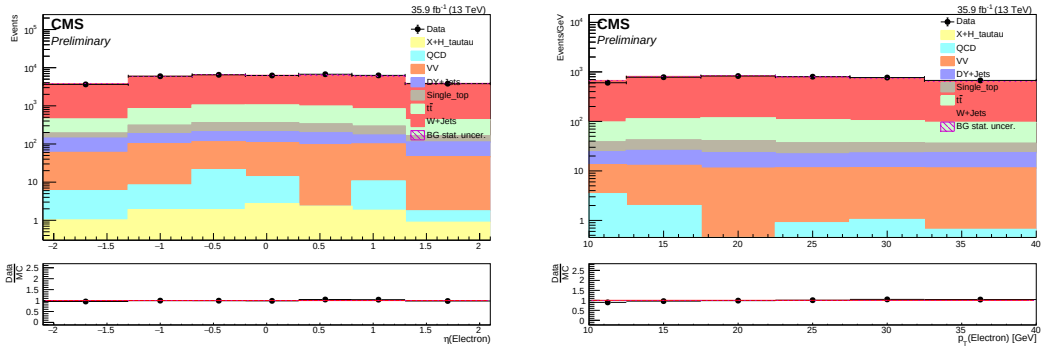

Figure 7.18: (a) η^e and (b) p_{T}^e distributions for the W + jets validation region VR1.

7.8 Expected Limits

After optimizing the cuts for the signal region, expected event yields from MC samples in the signal region after the VBF cuts are seen in Table 7.12. Based on these expected event yields in the signal region, limits are set on chargino-neutralino.

The expected limit on the chargino-neutralino in a democratic scenario, where slepton mass is defined as a half of the chargino mass and half of the neutralino mass ($\tilde{l} = 0.5\tilde{\chi}_1^{\pm}+0.5\tilde{\chi}_1^0$), after combining all channels is shown in Figure 7.21. The upper limit on the signal is obtained at 95% confidence level by using the CL_s method [53] which makes use of the m_{jj} distribution per channel to construct

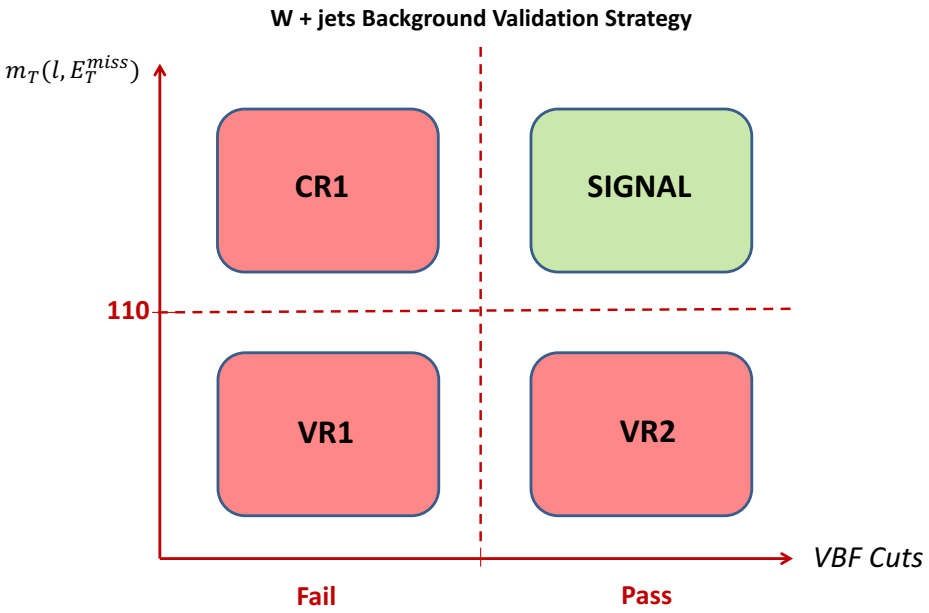

Figure 7.19: W + jets validation strategy.

a combined likelihood in bins of m_{jj}. As seen in the Figure 7.21, for different ΔM mass points (defined as the mass difference between chargino/neutralino and LSP), we exclude the chargino/neutralino mass below the value where theoretical cross section crosses the expected limit for the given mass difference points. We set the expected upper limit ~200 GeV on the chargino/neutralino where the theoretical cross section line crosses the expected limit in the case where $\Delta M = 1$ GeV. However, for the case of $\Delta M = 50$ GeV it is ~320 GeV after combining all channels.

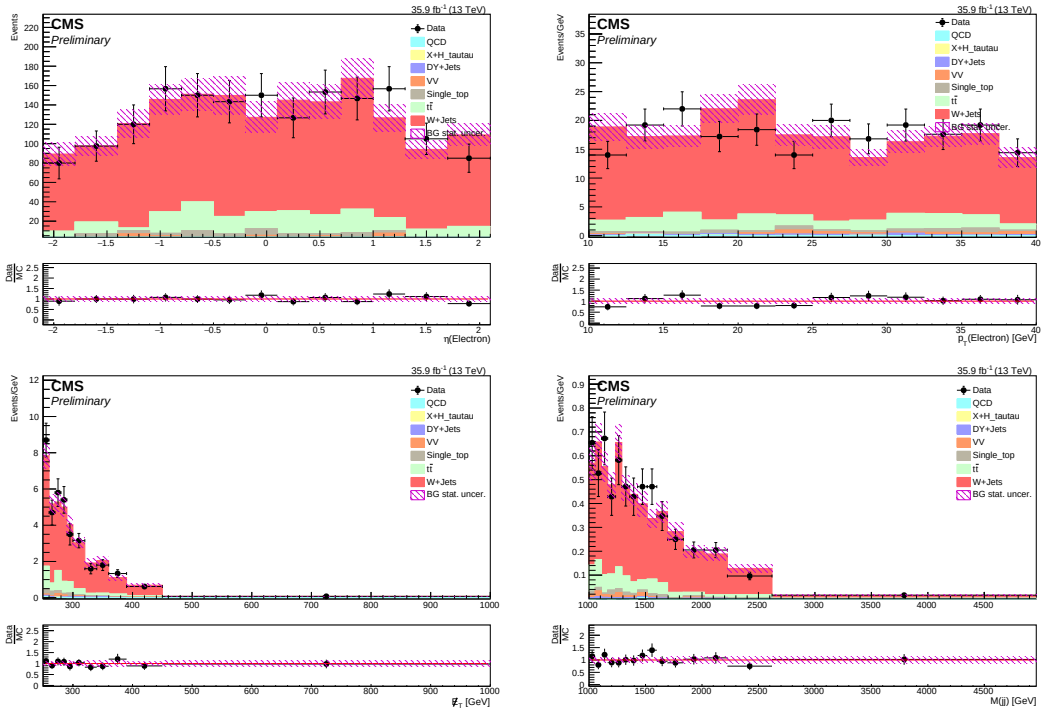

Figure 7.20: (a) η^{e}, (b) p_{T}^{e}, (c) E_{T}^{miss}, and (d) m_{jj} distributions for the W + jets validation region VR2.

Table 7.12: Expected event yield in the signal region after combining all leptonic channels.

	$DY + jets$	QCD	VV	$W + Jets$	sTop	$t\bar{t}$
$e^{\pm} + jj$	0.1 ± 0.0	6.4±5.9	1.0 ± 0.6	5.3 ± 1.0	0.1 ± 0.1	11.4 ± 2.1
$\mu^{\pm} + jj$	0.2 ± 0.1	0.0±0.0	1.3 ± 0.6	10.2 ± 2.1	2.3 ± 0.7	16.9 ± 2.6
$\tau^{\pm} + jj$	0.1 ± 0.1	1.1 ± 0.6	0.5±0.4	5.7 ± 1.1	0.5 ± 0.2	3.7 ± 1.2

7.9 Data in the Signal Region

As this dissertation research covers SM background estimation methodology for SUSY searches with events in final states with a single electron and E_{T}^{miss}

Table 7.10: Predicted and observed rates for the W + jets validation region VR1, which obtained with inverted m_T and VBF selections.

Sample	W + jets VR1
Diboson	319.6 ± 10.5
QCD	28.2 ± 8.9
Single Top	443.9 ± 8.0
W + jets	18986.9 ± 1452.8
DY + jets	351.8 ± 19.5
$t\bar{t}$	2008.6 ± 28.0
Total MC	22139.0 ± 1453.3
Purity	85.7%
Data	22433.0

along with two VBF jets, this section is blinded in this dissertation.

Table 7.11: Predicted and observed rates for the W + jets validation region VR2, which is used to validate the VBF efficiency measured from $Z(\rightarrow \mu\mu)$ + jets control sample CR3.

Sample	W + jets VR2
Diboson	8.3 ± 1.7
QCD	0.6 ± 0.4
Single Top	14.2 ± 1.4
W + jets	456.6 ± 48.8
DY + jets	5.5 ± 0.6
$t\bar{t}$	66.4 ± 5.1
Total MC	551.6 ± 49.1
Purity	82.7%
Data	530

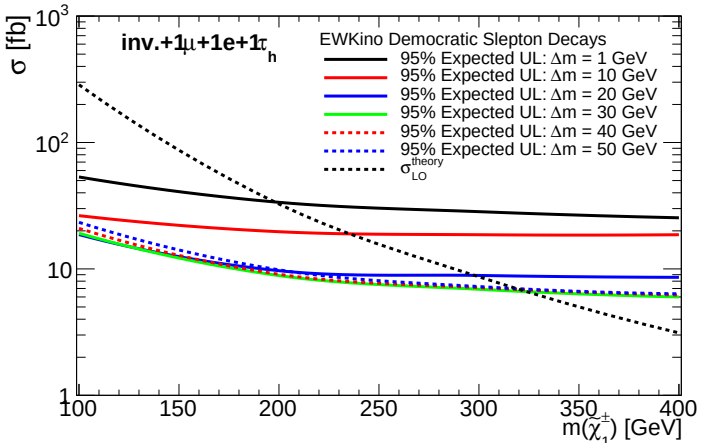

Figure 7.21: Expected upper limit on chargino/neutralino after combining all channels in a democratic scenario for different ΔM benchmarks.

8. CONCLUSIONS

The search for compressed mass spectra SUSY is challenging at the LHC. A new search is carried out using low energy single lepton events in a VBF topology in proton-proton collisions at a center-of-mass energy of 13 TeV at the LHC. We proposed to search for SUSY signal in the single soft lepton (e) channel with the requirement of $p_{\mathrm{T}} > 10$ GeV in order to explore the parameter space where other analysis have limited sensitivity. Full measurements of the SM event yields are crucial and I have carried out these measurement for single electon channel.

As described in Section 2, SUSY searches in final states with di-lepton + two VBF jets and MET were carried out at 8 TeV. Due to trigger constraint, the lepton p_{T} requirement was > 30 GeV which was not low enough ideally to look for SUSY signal in the case of a compressed mass spectra scenario. The second constraint was the efficiency of the reconstruction of two lepton at the same time which degrades the sensitivity of the analysis. Our proposed analysis should provide an improved sensitivity.

A methodology to determine MC-to-data scale factors (SFs) for two primary selection requirements ("central" and "VBF") is developed using both simulation and data. By creating $t\bar{t}$ and $W(\rightarrow e\nu)$ + jets enriched control regions, SFs for the central selections are calculated. In a similar way, the SF for VBF efficiency is extracted from a control region where events satisfy central selections in addition to the VBF selections. Due to low statistics in the control samples, VBF efficiencies and SFs for the central selections are validated in the high statistics and highly pure control samples. By using those two SFs, extrapolation from the control region, which has events similar as the signal region topology, to signal region

is carried out in order to estimate $t\bar{t}$ / $W(\rightarrow e\nu)$ + jets event contributions in the signal region. The expected event yield in the signal region is shown in Table 7.12.

Since this is a blind analysis of three single lepton channels (e, μ, τ), we will not look at the data in the signal region until all background estimates are completed. With an estimate of all other background contribution in the signal region in single μ and single τ channels, the analysis will be concluded either with a hint of new physics or setting limits on its masses using the m_{jj} / m_{T} distributions. (see Figure 7.21)

REFERENCES

[1] "MissMJ, "Standard model of elementary particles—wikipedia, the free encyclopedia,"." http://commons.wikimedia.org/wiki/File:Standard_Model_of_Elementary_Particles.svg. Accessed: Sep 2017.

[2] "CMS Collaboration, "Summaries of CMS cross section measurements"." https://twiki.cern.ch/twiki/bin/view/CMSPublic/PhysicsResultsCombined. Accessed: Oct 2017.

[3] S. P. Martin, "A supersymmetry primer (2011)," *arXiv preprint hep-ph/9709356*, vol. 161, p. 162.

[4] V. Khachatryan, A. Sirunyan, A. Tumasyan, W. Adam, E. Asilar, J. Erö, *et al.*, "Search for supersymmetry in the vector-boson fusion topology in proton-proton collisions at $\sqrt{s} = 8$ TeV," *JHEP*, vol. 11, p. 189, 2015.

[5] "CMS Collaboration, "Summary of observed limits for ewkino models"." https://twiki.cern.ch/twiki/pub/CMSPublic/OldPhysicsResultsSUS/EWKino_ICHEP2014_2.pdf. Accessed: Jun 2017.

[6] C. Lefèvre, "The CERN accelerator complex. Complexe des accélérateurs du CERN." Dec 2008.

[7] CMS Collaboration, "The CMS Experiment at the CERN LHC," *JINST*, vol. 3, p. S08004, 2008.

[8] V. Halyo, P. LeGresley, and P. Lujan, "Massively parallel computing and the search for jets and black holes at the LHC," *Nucl. Instrum. Meth.*, vol. A744,

pp. 54–60, 2014.

[9] G. Bayatian, A. Korablev, A. Soha, O. Sharif, M. Chertok, *et al.*, "CMS physics: Technical design report volume 1: detector performance and software," tech. rep., CMS-TDR-008-1, 2006.

[10] "CMS Collaboration, "CMS silicon pixels detector"." https://http://cms.web.cern.ch/news/silicon-pixels. Accessed: Sep 2017.

[11] CMS Collaboration, "Performance of the CMS hadron calorimeter with cosmic ray muons and LHC beam data," *JINST*, vol. 5, p. T03012, 2010.

[12] A. Colaleo, A. Safonov, A. Sharma, and M. Tytgat, "CMS technical design report for the muon endcap GEM upgrade," Tech. Rep. CERN-LHCC-2015-012. CMS-TDR-013, Jun 2015.

[13] V. Khachatryan, D. Anderson, A. Apresyan, A. Bornheim, J. Bunn, *et al.*, "The CMS trigger system," *JINST*, vol. 12, no. 1, p. P01020, 2017.

[14] "T. D. Collaboration, "b-tagging graphic"." http://www-d0.fnal.gov/Run2Physics/top/singletop_observation/b_tagging_graphic.png. Accessed: Jun 2017.

[15] "CMS Collaboration, "Public CMS data quality information"." https://twiki.cern.ch/twiki/pub/CMSPublic/DataQuality/int_lumi_per_day_cumulative_pp_2016_Golden_23Sep-PromEraH_Morion.png. Accessed: Jun 2017.

[16] Z. Wan, "Search for high-mass tau pairs in 1.96-TeV $p\bar{p}$ collisions," *Rutgers University*, 2005.

[17] R. Voss and A. Breskin, eds., *The CERN Large Hadron Collider, accelerator and experiments*. Cern Geneva, 2009.

[18] A. G. Delannoy, B. Dutta, A. Gurrola, W. Johns, T. Kamon, *et al.*, "Probing dark matter at the LHC using vector boson fusion processes," *Phys. Rev. Lett.*, vol. 111, no. 6, p. 061801, 2013.

[19] G. Aad, T. Abajyan, B. Abbott, J. Abdallah, S. A. Khalek, A. Abdelalim, *et al.*, "Observation of a new particle in the search for the standard model higgs boson with the ATLAS detector at the LHC," *Phys. Lett. B*, vol. 716, no. 1, pp. 1–29, 2012.

[20] S. Chatrchyan, V. Khachatryan, A. M. Sirunyan, A. Tumasyan, W. Adam, E. Aguilo, *et al.*, "Observation of a new boson at a mass of 125 GeV with the CMS experiment at the LHC," *Phys. Lett. B*, vol. 716, no. 1, pp. 30–61, 2012.

[21] S. L. Glashow, "Partial symmetries of weak interactions," *Nucl. Phys.*, vol. 22, p. 579, 1961.

[22] A. Salam and J. C. Ward, "On a gauge theory of elementary of interactions," *Nuovo Cim.*, vol. 19, p. 165, 1961.

[23] S. Weinberg, "A model of leptons," *Phys. Rev. Lett.*, vol. 19, no. 21, p. 1264, 1967.

[24] M. A. Halzen, F., *Quarks and leptons : an introductory course in modern particle physics.* 1984.

[25] J. W. Valle, "Status and implications of neutrino masses: a brief panorama," in *Massive Neutrinos: Flavor mixing of leptons and neutrino oscillations*, pp. 25–37, World Scientific, 2016.

[26] S. Dimopoulos, S. Raby, and F. Wilczek, "Supersymmetry and the scale of unification," *Phys. Rev.*, vol. D24, pp. 1681–1683, 1981.

[27] R. Allahverdi, B. Dutta, and K. Sinha, "Non-thermal higgsino dark matter: cosmological motivations and implications for a 125 GeV higgs," *Phys. Rev.*, vol. D86, p. 095016, 2012.

[28] G. Jungman, M. Kamionkowski, and K. Griest, "Supersymmetric dark matter," *Phys. Rept.*, vol. 267, p. 195, 1996.

[29] C. Boehm, A. Djouadi, and M. Drees, "Light scalar top quarks and supersymmetric dark matter," *Phys. Rev. D*, vol. 62, p. 035012, 2000.

[30] C. Balázs, M. Carena, and C. E. M. Wagner, "Dark matter, light top squarks, and electroweak baryogenesis," *Phys. Rev. D*, vol. 70, p. 015007, 2004.

[31] S. Chatrchyan, V. Khachatryan, A. Sirunyan, A. Tumasyan, W. Adam, *et al.*, "Search for supersymmetry in pp collisions at $\sqrt{s}$=8 TeV in events with a single lepton, large jet multiplicity, and multiple b jets," *Phys. Lett. B*, vol. 733, pp. 328–353, 2014.

[32] S. Belforte, V. Candelise, M. Casarsa, G. DELLA RICCA, A. Zanetti, *et al.*, "Search for new phenomena with the MT2 variable in the all-hadronic final state produced in proton-proton collisions at $\sqrt{s}$=13 TeV," *The Eur. Phys. J. C, Particles and Fields*, vol. 77, no. 10, pp. 1–34, 2017.

[33] B. Dutta, A. Gurrola, W. Johns, T. Kamon, P. Sheldon, and K. Sinha, "Vector boson fusion processes as a probe of supersymmetric electroweak sectors at the LHC," *Phys. Rev. D*, vol. 87, no. 3, p. 035029, 2013.

[34] A. G. Delannoy, B. Dutta, A. Gurrola, W. Johns, T. Kamon, *et al.*, "Probing dark matter at the LHC using vector boson fusion processes," *Phys. Rev. Lett.*, vol. 111, no. 6, p. 061801, 2013.

[35] B. Dutta, A. Gurrola, K. Hatakeyama, W. Johns, T. Kamon, *et al.*, "Probing compressed bottom squarks with boosted jets and shape analysis," *Phys. Rev. D*, vol. 92, no. 9, p. 095009, 2015.

[36] C. Balazs, M. Carena, and C. E. M. Wagner, "Dark matter, light stops and electroweak baryogenesis," *Phys. Rev.*, vol. D70, p. 015007, 2004.

[37] T. S. Pettersson and P. Lefèvre, "The Large Hadron Collider: conceptual design," Tech. Rep. CERN-AC-95-05-LHC, Oct 1995.

[38] G. Aad, J. Butterworth, J. Thion, U. Bratzler, P. Ratoff, *et al.*, "The ATLAS experiment at the CERN large hadron collider," *JINST*, vol. 3, p. S08003, 2008.

[39] A. A. Alves Jr, L. Andrade Filho, A. Barbosa, I. Bediaga, G. Cernicchiaro, G. Guerrer, *et al.*, "The LHCb detector at the LHC," *JINST*, vol. 3, no. 08, p. S08005, 2008.

[40] K. Aamodt, A. A. Quintana, R. Achenbach, S. Acounis, D. Adamová, C. Adler, *et al.*, "The ALICE experiment at the CERN LHC," *JINST*, vol. 3, no. 08, p. S08002, 2008.

[41] A. M. Sirunyan, A. Tumasyan, W. Adam, E. Asilar, T. Bergauer, *et al.*, "Particle-flow reconstruction and global event description with the CMS detector." Submitted to *JINST*, 2017.

[42] G. P. Salam, "Towards jetography," *Eur. Phys. J.*, vol. C67, p. 637, 2010.

[43] M. Cacciari, G. P. Salam, and G. Soyez, "The Anti-k(t) jet clustering algorithm," *JHEP*, vol. 04, p. 063, 2008.

[44] CMS Collaboration, "MET performance in 8 TeV data," Tech. Rep. CMS-PAS-JME-12-002, CERN, Geneva, 2013.

[45] W. Adam, R. Frühwirth, A. Strandlie, and T. Todorov, "Reconstruction of electrons with the gaussian-sum filter in the CMS tracker at the LHC," *Journal of Physics G: Nuclear and Particle Physics*, vol. 31, no. 9, p. N9, 2005.

[46] S. Baffioni, C. Charlot, F. Ferri, D. Futyan, P. Meridiani, *et al.*, "Electron reconstruction in CMS," *The Eur. Phys. J. C*, vol. 49, no. 4, pp. 1099–1116, 2007.

[47] CMS Collaboration, "Reconstruction and identification of τ lepton decays to hadrons and ν_τ at CMS," *JINST*, vol. 11, no. 01, p. P01019, 2016.

[48] CMS Collaboration, "Identification of b-quark jets with the CMS experiment," *JINST*, vol. 8, p. P04013, 2013.

[49] J. Alwall, M. Herquet, F. Maltoni, O. Mattelaer, and T. Stelzer, "MadGraph 5 : Going Beyond," *JHEP*, vol. 06, p. 128, 2011.

[50] T. Sjostrand, S. Mrenna, and P. Z. Skands, "PYTHIA 6.4 Physics and Manual," *JHEP*, vol. 05, p. 026, 2006.

[51] S. Alioli, P. Nason, C. Oleari, and E. Re, "A general framework for implementing NLO calculations in shower Monte Carlo programs: the POWHEG BOX," *JHEP*, vol. 06, p. 043, 2010.

[52] S. Agostinelli, J. Allison, K. a. Amako, J. Apostolakis, H. Araujo, *et al.*, "GEANT4: A simulation toolkit," *Nucl. Instrum. Meth.*, vol. 506, no. 3, pp. 250–303, 2003.

[53] A. L. Read, "Presentation of search results: the CL s technique," *Journal of Physics G: Nuclear and Particle Physics*, vol. 28, no. 10, p. 2693, 2002.